CARBON NANOTUBE NANOELECTROMECHANICAL SYSTEMS

PHD THESIS BY MARIANNA SLEDZINSKA

Director: Prof. Adrian Bachtold
Tutor de la UAB: Prof. Javier Rodriguez

Dr. Adrian Bachtold, profesor del CSIC en el CIN2, certifica que la presente memoria ha sido realizada bajo su dirección por Marianna Sledzinska.

Acknowledgments

First of all I would like to thank my thesis advisor prof. Adrian Bachtold. Secondly, the whole group of Quantum Nanoelectronics: MariaJose Esplandiu, Joel Moser, Alexander Eichler and ex-members: Amelia Barreiro, Daniel Garcia, Julien Chaste and Mariusz Zdrojek.

I would also like to thank CNM personnel: Neus Sabate and Marc Salleras for help with micro-scale heaters; Clean room staff: Jordi Llobet, Xevi Borrise and Libertad Sole for help with SEM and FIB, Marta Duch and Marta Gerboles for help with the micro-fabrication.

I would like to thank the tribunal: Neus Sabaté, Gabriel Abadal, Ricardo Rurali, Sergio Valenzuela and Maria Jose de Montserrat Esplandiu Egido.

Last but not least I thank my family and friends for help and support.

Contents

Contents 5
1. Introduction: carbon-based electronics 9
1.2 Carbon nanotube transistors and integrated circuits 10
1.3 Carbon nanotube optoelectronic devices 14
1.4 Outlook to carbon-based electronics 15
1.5 Aim of this work 16
2. Introduction to carbon nanotubes and graphene 19
2.1 Structural properties of carbon nanotubes 19
2.2 Electronic structure of CNTs 21
2.3 Phonons in CNTs 23
2.4 Mechanical properties 24
2.5 Synthesis of Carbon Nanotubes 25
2.5.1 Laser-ablation fabrication of MWNTs 26
2.5.2 CVD growth 26
2.6 Graphene 28
3. Nanoelectromechanical systems (NEMS) 31
3.1 Introduction 31
3.2 Carbon nanotube resonators 32
3.3 Carbon nanotube motors 39
4. High-frequency nanotube mechanical resonators 43
4.1 Introduction 43
4.2 Fabrication and measurements 44
4.3 Discussion 44
4.4 Conclusions 49
5. Multi-walled Carbon Nanotube Resonators 51
5.1 Introduction 51
5.3 Discussion 52
5.4 Conclusions 56
6. Micro-fabricated heaters for controlled thermal gradient CNT motor 57
6.1 Introduction 57
6.2 Platinum and gold based micro-heaters 59
6.2.1 Design, simulations and optimum geometry 59
6.2.2. Fabrication 62

6.2.3 Etching optimization 62
6.2.4 Adhesion layer thickness optimization 65
6.2.5 Heating layer optimization: gold heaters 66
6.2.6 Temperature characterization 66
6.2.7 Integration with CNT motor 67
6.3 Silicon Heaters 69
6.3.1 Design and simulations 69
6.3.2 Fabrication 72
6.3.4 Si heater temperature characterization 74
6.3.4 Integration with nanotube motor and etching problems 75
6.3.5 Bi-metallic layer for silicon heaters 77
6.4 Conclusions 78
7. Graphene heaters: a way to all-carbon electronics 79
7.1 Introduction 79
7.2 Fabrication 81
7.3 Graphene mechanical cleaning 83
7.4 Graphene heating properties 83
7.5 Conclusions 85
8. Carbon Nanotube Electron Windmill 87
8.1 Introduction: Chiral currents in CNTs 87
8.2 Sample preparation and measurements 90
8.3 Discussion 91
8.3.1 Rotating the plate with electric field 92
8.3.2 Influence of CNT edges 92
8.3.3 Friction force estimation with AFM 94
8.4 Conclusions 95
Annex A: Nanofabrication 97
A.1 Substrate preparation 97
A.2 Nanotube growth/deposition 97
A.3 Electron Beam Lithography (EBL) 99
A.4 Metal evaporation and lift-off 100
A.5 Atomic Force Microscopy (AFM) and device design 101
A.6 Electrical measurements and etching 103
A.7 Annealing 104

A.8 Electrical breakdown technique 104
Annex B: Mixing technique 107
B.1 Actuation and detection 107
B.2 Resonance width and quality factor with the FM technique 110
Annex C: Dynamics of a system with one degree of freedom 111
C.1 Dynamics of a system with infinite degrees of freedom 111
C.2 Flexural vibrations of a beam 111
Publications 115
Conferences 115
Bibliography 121

1. Introduction: carbon-based electronics

1.1 Motivation

The semiconductor industry has been able to improve the performance of electronic systems for more than four decades by making ever-smaller devices. However, this approach will soon encounter both scientific and technical limits, which is why a number of alternative device technologies are being explored. Here we review the progress that has been made with carbon nanotubes (CNTs). Field-effect transistors based on semiconductor nanotubes (CNTFET) and graphene nanoribbons have already been demonstrated, and metallic nanotubes could be used as high-performance interconnects. Moreover, owing to the excellent optical properties of nanotubes it could be possible to make both electronic and optoelectronic devices from the same material (2).

Microelectronics based on silicon is probably the technology, with most development in the past century. The dramatic advances in electronics have found uses in computing, communications, automation and other applications that affect just about every aspect of our lives. To a large extent these advances have been the result of the continuous miniaturization or 'scaling' of electronic

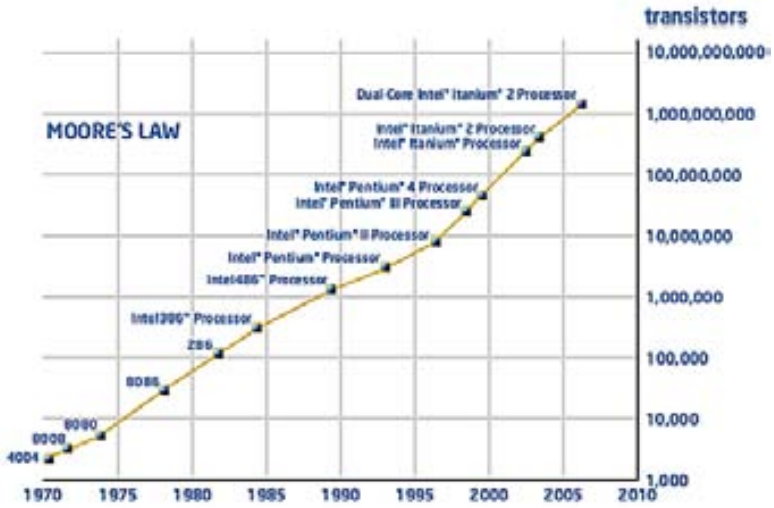

Fig. 1.1. Illustration of Moore's law, adapted from (1)

devices, particularly transistors, that has led to denser, faster and more power-efficient circuitry. Obviously, this device scaling and performance enhancement cannot continue forever, as a number of limitations of fundamental scientific as well as technological nature place limits on the ultimate size and performance of silicon devices. For over 50 years the progress of the semiconducting industry was following the prophetic statement of Gordon Moore, the co-founder of Intel, that the number of transistors on a silicon chip would grow exponentially, doubling every two years (Fig. 1.1).

The so-called Moore's law cannot be maintained forever and so the challenge is to find new materials which can be able to produce higher performance and better functionality.

CNTs are currently considered promising as building blocks for future electronics. This is not only due to their small size, but rather the overall properties. First of all, carrier transport is one-dimensional, which implies a reduced space for scattering and opens up the possibility of ballistic transport. Secondly, all the chemical bonds of carbon atoms are satisfied, so there is no need for chemical passivation of dangling bonds as in silicon. This implies that carbon electronics should not be bound to use SiO_2 as an insulator and instead high dielectric constant and crystalline insulators can be used. The strong covalent bonding gives CNTs high mechanical and thermal stability. Furthermore, both active devices (i.e. transistors) and interconnects can be made out of CNTs or graphene, leading to all-carbon electronics (3).

1.2 Carbon nanotube transistors and integrated circuits

First reports of carbon nanotube field-effect transistors based on semiconducting single-walled carbon nanotubes (SWNTs) date back to 1998 (4-5). A CNTFET consists of semiconducting single-walled carbon nanotube or a network of semiconducting SWNTs which are contacted by source and drain electrodes. Gate electrode is typically separated from the CNT by an insulator film. As in typical, semiconducting field effect transistor (FET) voltage applied on the gate can modulate source-drain current. The gate voltage induces accumulation of electron/holes, which make the valence and conduction bands move downwards/upwards with respect to the Fermi level.

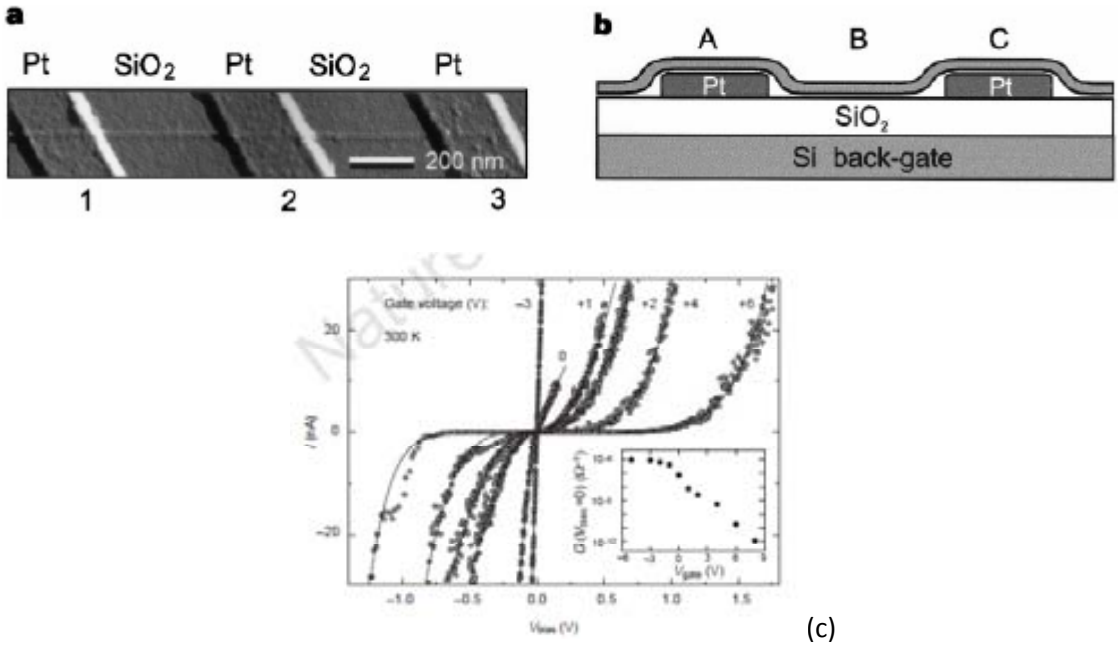

Fig. 1.2. (a) AFM image and (b) Schematic of the first CNTFETs with a semiconducting SWNT lying over two gold electrodes. (c) I–V_{bias} curves for various values of the gate voltage (V_{gate}). Data were taken at room temperature and in vacuum (10^{-4} mbar), with the voltage applied to contacts 1 (drain) and 2 (source). Inset, conductance at V_{bias} = 0 as a function of V_{gate}. Adapted from (4).

However, the electric field generated by the gate voltage is dependent not only on the electronic characteristics of the nanotube itself (that is on their band-gap characteristics) but also on the interface between the SWNTs and the metal electrodes where Schottky barriers can be formed. Schottky barriers in general can be formed when a semiconductor is brought into direct contact with a metal, due to the mismatch of the work functions of the metal and the CNT. A charge transfer occurs until the Fermi levels of the metal and the semiconductor are aligned. The charge transfer creates a depletion zone in the semiconductor near the junction (electrical dipole). Such depletion causes a rectifying behavior, meaning that carrier transport is hindered in one of the two possible current directions. Not all metal–semiconductor junctions form Schottky barriers. A metal–semiconductor junction that does not rectify current is called an ohmic contact. Rectifying properties depend on the metal's work function, the band gap of the intrinsic semiconductor, the type and concentration of dopants in the semiconductor, among other factors (2).The thickness and height of Shottky barrier can be increased or decreased with the electric field provided by the gate electrode. In general mechanisms based on tunneling processes and hence on the thickness of the barrier are more important at the contact/CNT interface than the ones depending on temperature which are more dependent on the height of the barrier (6). Therefore, when the Schottky barrier becomes thinner, tunneling of the charge carriers can be produced favoring the current flow in the CNTFET.

In the first generation of CNTFETs a nanotube was placed across two metallic contacts fabricated on top of a SiO_2-layer, and a voltage was applied to the conducting substrate to move carriers onto the tube (4). The tube could be 'turned on' by applying a negative bias to the substrate, thereby inducing holes on the initially non-conducting tube. Thus, this device is analogous to a p-type MOSFET (metal-oxide-semiconductor field effect transistor), with the nanotube replacing silicon as the channel. These devices work at room temperature. In figure 1.2 these early back-gated CNTFETs are shown in (a) an AFM image and in (b) a schematic illustration. The main disadvantage of these devices is that the variations in the output voltage are far too small to control the input of a second transistor, thus preventing these CNTFETs from being integrated into circuits (Fig. 12c). In addition, use of the substrate as a gate implies that all devices are turned on simultaneously.

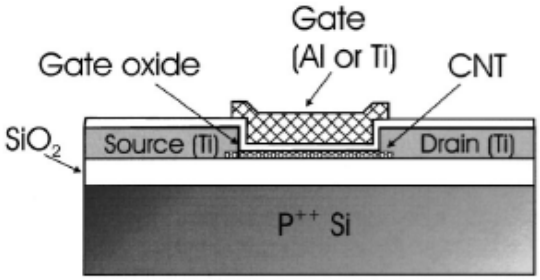

Figure 1.3. Schematic illustrations of a top-gated CNTFET resembling the conventional MOSFET structure. Adapted from (7)**.**

Up to now, a lot of effort has been put to improve the operation characteristics of CNTFETs. For instance, a reduction of the contact resistance of the tubes by a few orders of magnitude can be obtained by patterning source and drain on top of the tubes (8). Also a big improvement is obtained by reducing the insulator thickness. The bottom gate structure usually has an open geometry, in which the CNT is exposed to air. This presents an electrostatic disadvantage, because the gate insulator capacitance is diluted by the lower dielectric constant of the air surrounding the CNT. In

contrast, for top-gate geometry, the CNT is completely embedded within the gate insulator, offering the full advantage of the gate dielectric. Top-gated CNTFETs with a 15 nm gate oxide fabricated by Wind *et al*. (Fig. 1.3) resemble the conventional MOSFET (metal-oxide-semiconductor FET) structure and showed dramatic improvements that can compete with the leading prototype silicon transistors (7).

The fabrication and evaluation of CNT-based devices has advanced beyond single devices to include logic gates (9-12) and more complex structures such as ring oscillators (13).

A way of integration of multiple CNTFETs was proposed by Bachtold *et al*. in 2001. Different micro-fabricated Al wires were used as separate local gates with a native Al_2O_3 insulating layer and single semiconducting SWNTs contacted by gold electrodes were used as channels (Fig. 1.4a, b) (11).

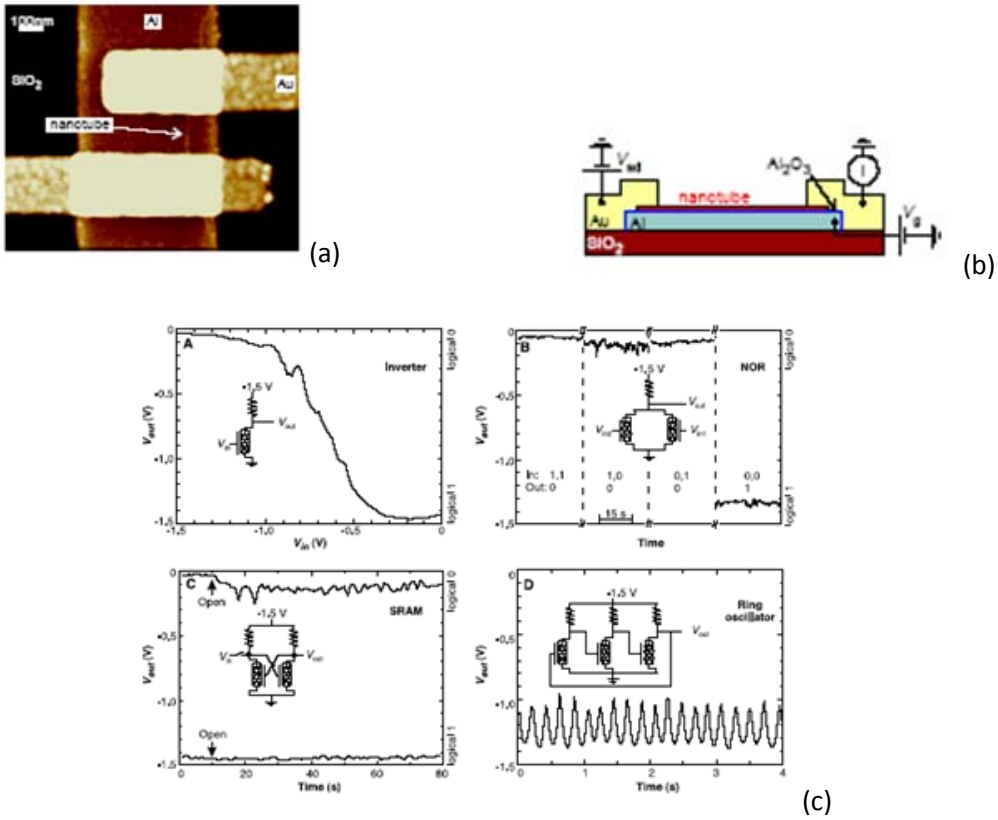

Figure 1.4. (a) AFM image of a single-nanotube transistor where a semiconducting nanotube is contacted by two Au electrodes and an Al wire, covered by a few-nanometers-thick oxide layer, is used as a gate. (b) Schematic side view of the device. (c)Demonstration and schematics of the electronic circuits of one-, two-, and three-transistor logic circuits with CNTFETs such as (A) an Inverter, (B) a NOR gate for the four possible input states (1,1), (1,0), (0,1) and (0,0), (C) a SRAM cell composed of two nanotube FETs and (D) a ring oscillator (11).

The proximity of the gate led to high gain (>10) and large output swing. For any further development of operational logic circuits, a gain at large bias voltage is a crucial requirement, because the output of one logic structure must be able to drive the input of the next logic structure. The output typically has to provide a voltage swing of about 1 V.

The high gain of the first transistor made possible control of the input of a second transistor and therefore was unambiguously suited for further applications in microelectronics. Several digital logic operations such as an inverter, a logic NOR, a SRAM cell and an ac ring oscillator were reported. The schematics of the logic circuits and their characteristic output curves are shown in Fig. 1.4c.

All the CNTFETs used to build the latter devices were p-type. This is a consequence of the fact that semiconducting nanotubes which were exposed to ambient conditions are typically operating like p-type semiconductors, mainly due to molecules from the atmosphere being adsorbed onto the nanotube and charge-transfer from the electrodes. The adsorption of molecules could be a problem because they affect the reproducibility of the device characteristics. On the other hand this special sensitivity to adsorbates makes CNTFETs to exceptional sensors for the detection of different gases (14). Nevertheless, the problem of adsorption and desorption of molecules on the CNT can be controlled by either covering the nanotubes by a thin film or by applying thermal-annealing treatments in a vacuum (15). This allows to get n- and p-type CNT transistors in a controlled manner and to realize the last step towards CMOS technology. Such n-type and even ambipolar transistors have been realized by doping nanotubes with metals (15-17) as well as by embedding the SWNTs in a PMMA thin film and applying thermal treatments in vacuum (12, 15). Up to now inverters (9, 15) and intra-molecular inverters (12) based on CNTs have been realized. To build the intra-molecular CNTFET inverter, first, a SWNT bundle was deposited on top of three gold electrodes, resulting in two p-type CNTFETs in series. Then, the entire device was covered by PMMA, opening a window afterwards by means of e-beam lithography, as is shown in the AFM image in Fig. 1.5a. Potassium was used to dope half of the nanotube through this window to produce n-CNTFET, while the half protected by the PMMA film remained p-type. In this case, a common back gate was used.

Additional improvements in performance for CNTFET devices can be obtained by further improving the gate–channel capacitance by reducing the gate dielectric thickness and/or using higher dielectric constant materials, along with reductions in gate length. Indeed, CNTFETs with high-*k* materials have already been built by Javey *et al*. demonstrating a high voltage gain up to 60 (9).

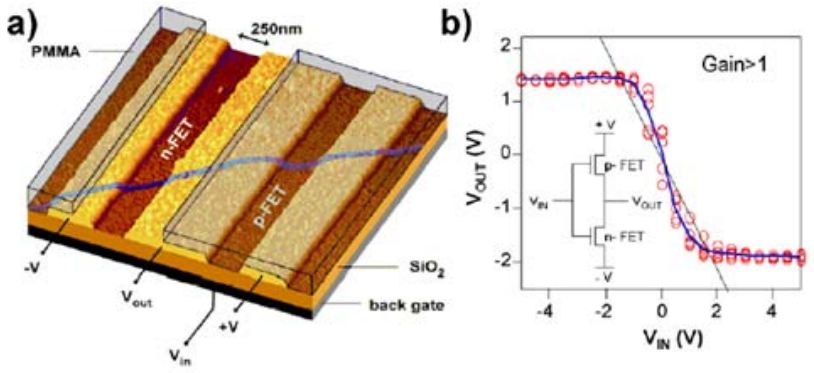

Fig. 1.5. (a) AFM image showing the design of an intramolecular logic gate. (b) Electrical characteristics of the intramolecular voltage inverter (12)**.**

A number of p-type CNTFET devices with different geometries have been reported in the literature. A selection of some of these CNTFETs was compared with their silicon based counterparts in Table 1.1 (18). It can be seen that the drive current (on current) of the p-CNTFETs is between 3 and 20 times larger than for state-of-the-art Si transistors with approximately two to 18 times higher transconductance. The sub-threshold slopes of the CNTFETs are somewhat worse than for the Si transistors, but this is related to the thicker gate oxides (except for the first one). Thus, it seems that CNTFETs have superior properties to current Si transistors and the experimental results advocate strongly for CNTs as candidates for future nanoelectronic technologies.

In general, the key advantage of CNTFETs over Si MOSFETs in logic applications is their much lower capacitance of ~10 aF (for d_{CNT} = 1 nm, L = 10 nm, t_{ox} = 5 nm) and their somewhat lower operating voltage. An area of clear advantage of CNTFETs is their lower switching energy per logic transition.

	CNT FET McEuen (2002)	CNT FET Seidel (2003)	CNT FET Javey (2003)	CNT FET Javey (2004)	CNT FET Seidel (2004)	TriGate Doyle (2003)	FinFET Yu (2002)	SON Harrison (2003)
Channel Material	CNT	CNT	CNT	CNT	CNT	Si	Si	Si
Drive Voltage [V]	1.0	1.0	0.6	0.4	1.0	1.3	1.2	0.9
Drive Current [mA/μm]	2.96	4–20	14	11.6	2.4–6.4	0.88	0.72	0.914
Transconductance [μS/μm]	6666	260	3070	17650	2640–6430	920	900	1170
Subthreshold Slope [mV/dec]	80	700–1100	150–170	110	105	69.5	101	70
On Resistance [Ω/μm]	473	50–250	43	22	155–425	1480	1667	985
Gate Length [nm]	1400	150–2000	300	50	600	60	10	70
Gate Oxide Thickness [nm]	1	200	67	8	8*	1.5	1.7	2
Off Current [nA/μm]	N/A	1.0	1.0	600	22**	120	20	1

Table 1.1: Comparison of key device characteristics of state-of-the-art p-type carbon nanotube and silicon transistors (18).

1.3 Carbon nanotube optoelectronic devices

Electrically or optically generated electron and hole carriers in semiconductors can recombine by a variety of different mechanisms (for instance by radiative or Auger recombination). If the recombination involves emission of a photon it is called electroluminescence and is to great means used for production of light sources, such as light emitting diodes (LEDs). In order to fabricate LEDs, or other electroluminescent devices, one must generate and bring together significant populations of electrons and holes. Conventionally, this is achieved at the interface between a hole-doped and an electron-doped semiconductor (a *p–n junction*).

In case of ambipolar CNTFETs, both electrons and holes can be simultaneously injected from the source and drain of the CNTFET. The quasi-1D character of the CNT confines the two types of carriers, which are driven towards each other. Indeed, radiative recombination in an ambipolar CNTFET was reported in ref. 19. The main difference between a semiconducting LED and a CNT is that the CNT is not doped so there is no clear p–n junction. As a result, the light does not originate from a fixed point along the CNT, but its origin can be translated by simply changing V_g, which determines the local potential in a long CNT device and the overall emission intensity is maximized when the hole and electron currents become equal (19, 20).

For some devices, localized electroluminescence is also observed from particular spots on a SWNT even under unipolar transport conditions. This happens at the spots with some inhomogeneities such as trapped charges in the gate insulator of the FET and interfaces between materials with different dielectric constants. In general these inhomogeneities produce voltage along the CNT and generate large, local electric fields (21). These fields can accelerate the carriers to an energy that allows them to generate electron–hole pairs through an intra-nanotube impact-excitation process. This excitation mechanism offers a number of possibilities for new applications. For example, more intense and brighter light sources can be produced because unipolar currents in CNTs can be higher than ambipolar currents, carrier multiplication can take place in the high fields and the emission is more localized.

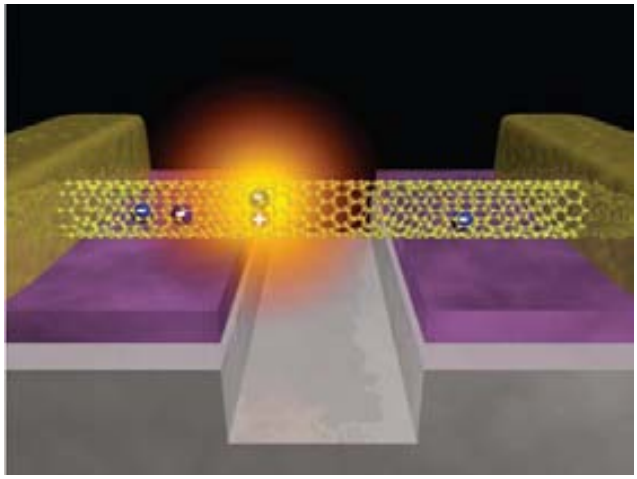

Fig. 1.6. Light emission from a nanotube. Schematic of a back-gated nanotube transistor suspended over a trench used to produce a sudden change in the potential along the nanotube (2)**.**

Photoconductivity is the reverse process of electroluminescence, with optical radiation producing electron–hole pairs that are separated by the applied field. Single CNT photoconductivity was reported for the first time in 2003 (22). The resonant excitation of a CNT generates an electric current and can be used as a nanosized photodetector, a photo switch, or as a spectroscopic tool. Alternatively, in the opencircuit configuration the device generates a photovoltage. Internal fields such as those formed at Schottky contacts, or defect sites can also separate photogenerated electron–hole pairs and can be used to image such sites and determine the band bending in an open-circuit configuration (23-25). Thus, a CNTFET device can be used as a transistor, a light emitter or a light detector.

1.4 Outlook to carbon-based electronics

To conclude, carbon nanotubes offer a model system to study electrical and optical phenomena on the nanometre scale. Those 1-D materials with exotic properties, long the realm of theoretical studies, are now open to experimentation. There is no doubt that in the future new information on the nano-scale physics will be obtained through the experimental studies on nanotubes.

In terms of direct technological applications, we focused here only on electronic switching and light emission and detection. Apart from that, nanotubes offer the potential of very fast (THz) transistors, logic devices, and simpler and cheaper self-assembly based fabrication. In addition, transistors with properly functionalized CNTs can be used as sensitive and selective chemical and biological sensors. Further integration to include optics could lead to a unified electronic — optoelectronic technology. At the same time carbon-based research is developing in other directions: spintronics, material science and nanoelectromechanical systems, discussed in more detail in following chapters.

How soon do we expect to see developments in nanotechnology? Even though the CNTs are one of the most promising materials for molecular electronics, many challenges remain before they can become a successful technology. The main hurdle is our current inability to produce large amounts of identical nanostructures. Nanotubes come in many sizes and structures and the same is true of many other nanostructures. For example, there is no reliable way to directly produce a single CNT type such as will be needed in a large integrated system, and patterning graphene is limited by the resolution of current lithographic techniques. However, promising signs that these problems will be circumvented soon are appearing. The success of carbon-based electronics will depend on how rapidly these techniques develop.

1.5 Aim of this work

In order to realize future nanotube electronic and electro-mechanical systems, it is not only necessary to thoroughly understand the underlying physical phenomena of both single as multi-walled carbon nanotubes (MWNTs), but also to be able to fabricate devices possessing the desirable qualities. Many efforts of this work were dedicated to nanotube manipulation and nanofabrication in order to integrate carbon nanotubes in current fabrication processes and achieve novel type of devices. The device fabrication is described in the *Annex A*.

In the thesis various attempts to experimental realization of CNT-based nano-electromechanical systems are shown.

Typically, the CNT devices presented later in this thesis operate in so-called transistor geometry, which is why it is important to understand principles of operations of CNTFETs, explained above in *Chapter 1*. Then, *Chapter 2* brings a short introduction to structural and electronic properties of CNTs and graphene, ways of synthesis and methods used for characterization. The *Chapter 3* is an introduction to micro and nanoelectromechanical systems, focusing carbon nanotube resonators and motors.

In the second part of the thesis carbon nanotube resonators are studied. To perform the measurements the so-called mixing technique was used, explained in Annex *B*. In *Chapter 4* a giga-hertz operation frequency resonator based on ultra-short SWNT is presented. Also influence of nanotube length and temperature on the resonator frequency and principles of mass sensing are discussed.

In *Chapter 5* MWNT resonators of different diameters are measured with emphasis of frequency as a function of a number of shells. The number of shells can be reduced using the electrical breakdown

technique and the MWNT resonator eigenmodes can be approximated using the elastic beam theory, which is in details explained in the *Annex C*.

The third part of the thesis is dedicated to carbon nanotube motors. First of all, in *Chapter 6* different approaches to fabricating micro-scale heaters are presented in order to realize controlled thermal gradient motor. Suspended micro-heaters based on platinum and gold are presented, as well as non-suspended heaters based on highly-doped silicon. In *Chapter 7*, a novel type of graphene-based heating is shown. For all types of heaters fabrication, characterization and integration with CNT motor is discussed. Finally, in *Chapter 8* an intention of realization of CNT electron windmill is presented.

2. Introduction to carbon nanotubes and graphene

2.1 Structural properties of carbon nanotubes

Since their discovery in 1991, carbon nanotubes have been a subject of intense study due to their exceptional electrical and mechanical properties (26). In the simplest view, CNTs are cylinders made of rolled graphite sheets. If a tube is made of one cylinder it is called single-walled carbon nanotube (SWNT) and a tube made of several concentrically arranged cylinders with the same axis is called multi-walled carbon nanotube (MWNT). They are usually ~nm in diameter and ~µm in length, however multiwall nanotubes can have much larger diameters. For MWNTs the interlayer spacing between the different carbon shells amounts about 3.4 Å, the interlayer spacing of graphene, and the length of MWNTs can extend up to hundreds of microns or even centimeters (27).

(a) (b)

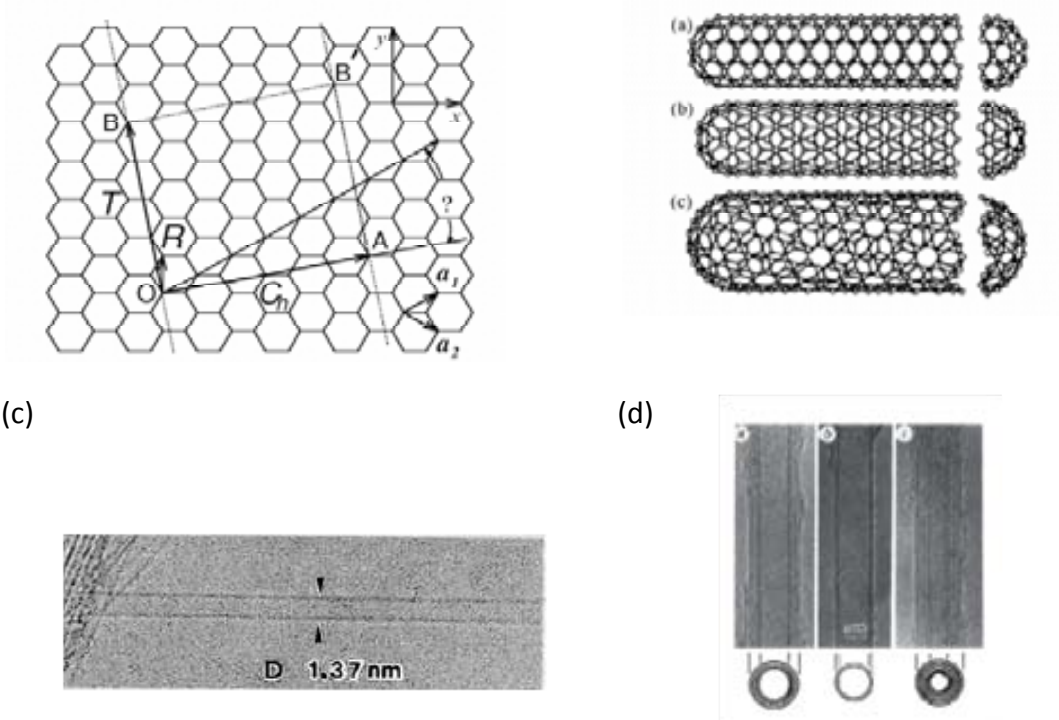

(c) (d)

Fig. 2.1 (a) Graphene honeycomb lattice. If lattice sites O, A, B and B' are connected, a nanotube is constructed. The rectangle OABB' defines a unit cell for the nanotube. OA and OB define the chiral vector C_h and translational vector *a*, respectively. The figure is constructed for (*n*,*m*) = (4,2) nanotube (28)**. (b) From top, structures of: armchair (*n*,*n*), zig-zag (*n*,0) and chiral (arbitrary) nanotubes** (29) **(c) and (d) some of the first TEM images from Iijima *et al.* of a single SWNT, and of MWNT, respectively** (30)**.**

Every graphene sheet, has a honeycomb lattice, in which we can distinguish two basis vectors $\overrightarrow{a_1}$ and $\overrightarrow{a_2}$, where a_1= (√3/2, 1/2)a and a_2= (√3/2 ,−1/2)a; a = √3a_{c-c} and a_{c-c}= 1.44Å is the carbon-carbon bond length (Fig. 2.1a). In a nanotube graphene lattice vector $\vec{c} = n\overrightarrow{a_1} + m\overrightarrow{a_2}$; *n* ,*m* ≥0, define circumference of the tube. The circumference vector, also called the chiral vector ($\vec{C}_h$) is denoted by the pair (*n*, *m*). Many properties of CNTs, like electronic band structure, vary with the chiral vector; therefore it uniquely defines a particular tube. Corresponding reciprocal lattice vectors are given by: $\overrightarrow{b_1} = (\frac{2\pi}{a\sqrt{3}}, \frac{2\pi}{a})$ and $\overrightarrow{b_2} = (\frac{2\pi}{a\sqrt{3}}, \frac{2\pi}{a})$.

The direction of the chiral vector is described by the chiral angle θ, defined as the angle between $\overrightarrow{a_1}$ and $\vec{c}$. It is calculated from (31):

$$\cos\theta = \frac{a_1 \cdot c}{|a_1| \cdot |c|} = \frac{n + m/2}{\sqrt{n^2 + nm + m^2}} \qquad (2.1)$$

We distinguish three types of CNTs. Tubes with chiral vector (*n,*0), which indicates chiral angle θ = 0°, are called zig-zag tubes; (*n,n*) tubes, with chiral angle θ= 30°, are called armchair tubes and the rest is generally called chiral tubes, as shown in Fig. 2.1b.

The smallest graphene lattice vector $\vec{T}$ perpendicular to $\vec{C}_h$ defines the translational period *t* along the tube axis.The lattice vector $\vec{T}$ can also be expressed in terms ofthe basis vectors $\overrightarrow{a_1}$ and $\overrightarrow{a_2}$ as $\vec{T} = t_1\vec{a}_1 + t_2\vec{a}_2$. Using $\overrightarrow{C_h} \cdot \vec{T} = 0$, the expressions for t_1 and t_2 are given by:

$$t_1 = \frac{2n + m}{N_R},\ t_2 = -\frac{2n + m}{N_R} \qquad (2.2)$$

where N_R is the greatest common divisor of (2*n*+*m)* and (2*m*+*n*). The length of the translational vector *t* is given by

$$t = \left|\vec{T}\right| = \frac{a\sqrt{3 \cdot (n_1^2 + n_2^2 + n_1 n_2)}}{N_R} \qquad (2.3)$$

Depending on (*n,m*) values the tube can be either metallic or semiconducting. If (*n*-*m*) = 3*l*, where *l* is an integer, the nanotube is metallic and if (*n*-*m*) = 3*l*±1 nanotube is semiconducting. Therefore, all armchair nanotubes are always metallic. Zig-zag nanotubes are quasi-metallic when *n* is multiple of 3, otherwise they are semiconducting.

The chiral vector determines structural parameters, such as diameter or number of carbon atoms in unit cell. The diameter of the tube is related to the length of chiral vector:

$$d = \frac{|c|}{\pi} = \frac{a_0}{\pi}\sqrt{n_1^2 + n_1 n_2 + n_2^2} = \frac{a_0}{\pi}\sqrt{N} \qquad (2.4)$$

where *N* is the number of hexagons contained within the 1D unit cell of the nanotube and is defined by:

$$N = 2(m^2 + n^2 + nm)/d \qquad (2.5).$$

Expressions for the reciprocal lattice vectors $\overrightarrow{K_2}$ along the nanotube axis and $\overrightarrow{K_1}$ in the circumferential direction are obtained from the relation $\overrightarrow{R_i} \cdot \overrightarrow{K_j} = 2\pi\delta_{ij}$, where $\overrightarrow{R_i}$ and $\overrightarrow{K_j}$ are, respectively, the lattice vectors in real and reciprocal space. Using the relations $\overrightarrow{C_h} \cdot \overrightarrow{K_1} = 2\pi$ and $\overrightarrow{C_h} \cdot \overrightarrow{K_2} = 0$ on the one hand, and, on the other hand, $\overrightarrow{T} \cdot \overrightarrow{K_1} = 0$ and $\overrightarrow{T} \cdot \overrightarrow{K_2} = 2\pi$, we get the expressions for $\overrightarrow{K_1}$ and $\overrightarrow{K_2}$: $\overrightarrow{K_1} = (1/N_C) \cdot (-t_2\vec{b}_1 + t_1\vec{b}_2)$ and $\overrightarrow{K_2} = (1/N_C) \cdot (m\vec{b}_1 - n\vec{b}_2)$ where $\vec{b}_1$ and $\vec{b}_2$ are the reciprocal lattice vectors of graphene. Since nanotubes are one-dimensional materials, only $\overrightarrow{K_2}$ is a reciprocal lattice vector. Vector $\overrightarrow{K_1}$ gives discrete $\vec{k}$ values in the direction of $\overrightarrow{C_h}$.

In general, the atomic structure of CNTs can be investigated by direct imaging, such as transmission electron microscopy (Fig. 2.1c, d) or scanning probe microscopy. Other methods include electron diffraction and atomic or scanning force microscopy (AFM/SFM). Very often above-mentioned methods are combined for cross-checking (28).

2.2 Electronic structure of CNTs

The electronic structure of CNTs is usually discussed on the basis of the band structure of graphene (Fig. 2.1). We can obtain the band structure of nanotubes by imposing the periodic boundary condition along the circumferential direction. The values of the wave vector $\vec{k}$ are quantized in the circumferential direction due to the periodic boundary condition $\vec{k} \cdot \vec{C}_h = 2\pi j$ where *j* is an integer (32). The electrons are only free to move in an axial direction. This quantization along the circumferential direction gives rise to discrete numbers of parallel equidistant lines, representing the allowed $\vec{k}$ modes in the reciprocal space of the graphene. Each line corresponds to a 1D channel for conduction along the nanotube. The distance between adjacent lines, $2/d_t$, is inversely proportional to the nanotube diameter d_t, and the orientationof the lines are given by the chiral angle θ. These discrete lines that give the one-dimensional energy dispersion relation of SWNTs E_{SWNT} can be obtained by zone-folding of the energy dispersion of graphene $E_{graphene}$ according to ref. 32:

$$E_{SWNT}(k) = E_{graphene}\left(k\frac{\vec{K}_2}{\left|\vec{K}_2\right|} + j\vec{K}_1\right), \text{ for } j=0,\ldots, N_C\text{-}1, \text{ and } -\pi/t < k < \pi/t. \qquad (2.6)$$

Where:

$$E_{graphene}(k_x, k_y) = \pm[1 + 4\cos(\frac{k_x a\sqrt{3}}{2})\cos(\frac{k_y a}{2}) + 4\cos^2(\frac{k_y a}{2})]^{\frac{1}{2}} \qquad (2.7).$$

To obtain explicit expressions for the dispersion relations, the simplest cases to consider are the nanotubes having the highest symmetry (armchair and zigzag). The quantization condition for armchair nanotubes is $\sqrt{3}nak_x = 2\pi q$ (q = 1,..., 2n), whereas $nak_y = 2\pi q$ (q= 1,..., 2n) applies for zigzag nanotubes. For armchar nanotubes the Fermi energy at the vertices of the Brillouin zone is sitting exactly on the allowed *k* modes, giving the metallic nature for armchair nanotubes. The dispersion relations for armchair and zigzag nanotubes can be obtained by inserting these quantization conditions into the equation of the energy dispersion of graphene to yield (33):

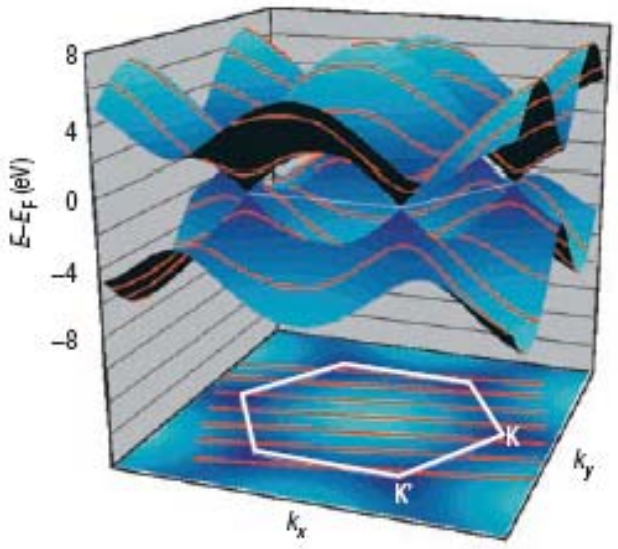

Fig. 2.2. (a) The band structure (top) and Brillouin zone (bottom) of graphene. The quantization of the circumferential momentum, leads to the formation of a set of discrete energy sub-bands for each nanotube (red parallel lines). The relation of these lines to the band structure of graphene determines the electronic structure of the nanotube. If the lines pass through the K or K' points, the nanotube is a metal; if they do not (such as in this figure), the nanotube is a semiconductor (34).

$$E_{armchair}(k) = \pm t[1 \pm 4\cos(\frac{\pi q}{n})\cos(\frac{ka}{2}) + 4\cos^2(\frac{ka}{2})]^{\frac{1}{2}} \quad \text{for } -\pi < ka < \pi \text{ and } q=1,\ldots,2n \qquad (2.8)$$

$$E_{zigzag}(k) = \pm t[1 \pm 4\cos(\frac{\pi q}{n})\cos(\frac{\sqrt{3}ka}{2}) + 4\cos^2(\frac{\pi q}{n})]^{\frac{1}{2}} \text{ for } -\frac{\pi}{\sqrt{3}} < ka < \frac{\pi}{\sqrt{3}} \text{ and } q=1,\ldots,2n. \qquad (2.9)$$

Next, we move on to analyze the density of states (DOS), *i.e.*, the number of states for a given energy interval. The DOS strongly depends on the dimensionality of the system. CNTs are one-dimensional systems; therefore 1/√E behavior for the DOS is expected (35, 36).

We express DOS of CNTs as:

$$D(E) = \frac{\sqrt{3}a^2}{2\pi R}\sum_i \int dk\,\delta(k - k_i)\left|\frac{\partial \varepsilon}{\partial k}\right|^{-1} \qquad (2.10)$$

Where $\varepsilon(k_i) = E$ and R is the tube radius. Energy dispersion relation and DOS for two different nanotubes: semiconducting and metallic are shown in Fig. 2.3. The unique feature is the presence of the so called van Hove singularities at the band edges, which is indicative of 1D system.

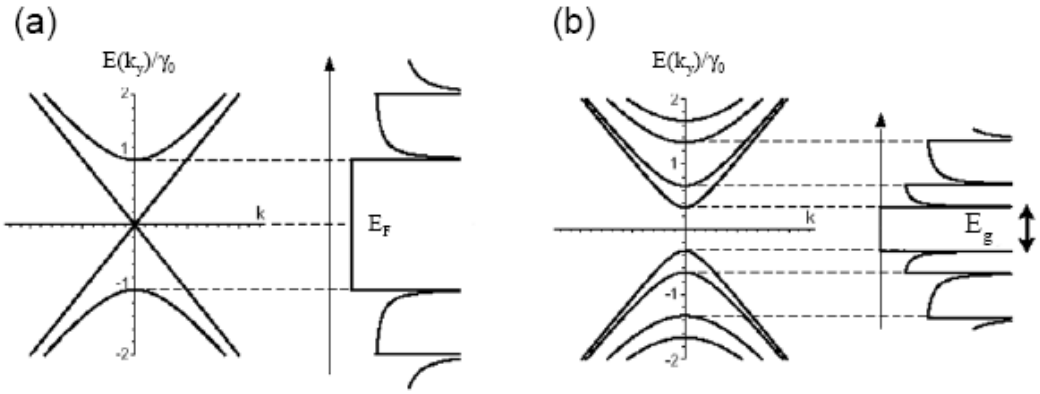

Fig. 2.3. Approximate one-dimensional energy dispersion relations and corresponding density of states for (a) metallic carbon nanotubes and (b) semiconducting carbon nanotubes, respectively. The number of subbands depends on the $\vec{C}_h$ vector. The energy at the Fermi level is zero (28).

Optical spectroscopy can yield some useful information about the physical properties of CNTs. It is because CNTs, due to their quasi one-dimensionality, exhibit strongly structured optical spectra. As discussed above, the singularities in the DOS should also cause strong absorption and luminescence peaks.

2.3 Phonons in CNTs

Phonons denote the quantized normal mode vibrations, which can strongly affect thermal, transport and mechanical properties in solids.

As a first approximation, the phonon dispersion relations for a SWNT ω_{SWNT} can be determined by zone-folding of the graphene phonon dispersion relation $\omega_{graphene}$, in the same was as it was done for the electronic structure of SWNTs. Since there are $2N_C$ carbon atoms in the unit cell of a CNT, $6N_C$ phonon dispersion branches for the three-dimensional vibrations of atoms are folded into the one-dimensional Brillouin zone of a SWNT along the $\overrightarrow{K_2}$ direction.

However, the zone-folding method does not always give the correct dispersion relation for a SWNT, especially in the low frequency region. In order to avoid these difficulties, the three-dimensional

dynamical matrix problem can be solved directly using ab-initio methods (31) . In Fig. 2.4 the phonon dispersion relations of graphene and armchair SWNT (10, 10) calculated by zone-folding methods are compared.

Investigation of the phonon structure is important, since they are mainly responsible for thermal conduction process and play an important part as carriers of thermal energy. The vibrational spectra also enable us to investigate elastic properties of the systems (31). Therefore, Raman spectroscopy, which allows investigation of phonon modes frequencies and intensities, is very useful for nanotube characterization. Raman spectroscopy is a commonly used method to determine the diameter distribution of SWNTs. The radial breathing mode (RBM) of SWNTs or the outer tube of DWNTs (double-walled carbon nanotube) appears from 140 to 280 cm^{-1} while the RBM of the inner tube of the DWNTs appears from 250 to 400 cm^{-1}. The diameter of the tubes can be calculated according to the formula $\upsilon_{RBM} = 233 / d + 14$, υ_{RBM} being the Raman shift of the observed peaks in cm^{-1} and d being the diameter of the SWNTs or the inner or outer tube of DWNTs in nm (37). Raman spectroscopy has also been shown to be a perfect tool to evaluate the defect concentration and crystalline lattice in different sp^2-hybridised carbon structures (38-41).

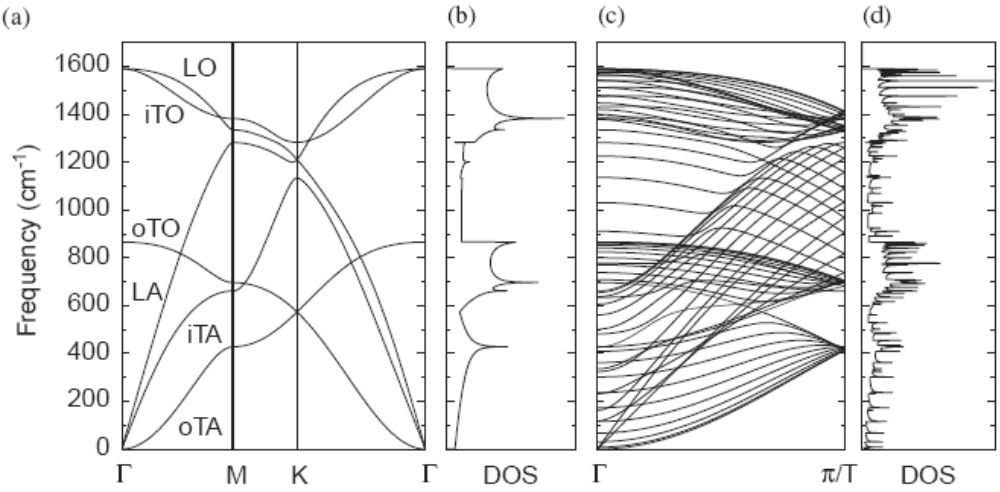

Fig. 2.4. (a) Phonon dispersion of 2D graphite. The phonon branches are labeled: out-of-plane transverse acoustic (oTA), in-plane transverse acoustic (iTA), longitudinal acoustic (LA), out-of-plane transverse optic (oTO), in-plane transverse optic (iTO), longitudinal optic (LO). (b) The phonon density of states for a 2D graphene sheet (c) The calculated phonon dispersion relation of a (10, 10) armchair nanotube, calculated from by using the zone folding procedure. (d) The corresponding phonon density of states for a (10, 10) nanotube (31)**.**

2.4 Mechanical properties

Carbon nanotubes have extraordinary mechanical properties. They are very light and stiff, with a Young's modulus of 1 TPa for the SWNT and 0.3 TPa for the MWNT. This makes them promising candidates for NEMS applications as well as for exploration of the quantum phenomena (42).

In the year 2000 Yu *et al.* demonstrated ultra-high tensile strength of CNTs (Fig. 2.5), ranging from 11 to 63 GPa for MWNTs, and from 13 to 52 GPa for SWNTs (43, 44). In the same year Cummings and Zettl observed the controlled and reversible telescopic extension of MWNTs within a TEM. They estimated shear strengths corresponding to static and dynamic friction to be 0.66 and 0.43 MPa, respectively (45).

Experimental observations of CNTs during compression and bending suggest that, at a global level, the CNTs may be treated as some form of "effective" beam. However, the experimental observations of internal structures during bending, buckling, and telescopic sliding indicate that specific structural features of CNTs make important contributions to CNT deformation response during mechanical loading, and such features should be accounted for in any "effective beam" model of a nanotube (46).

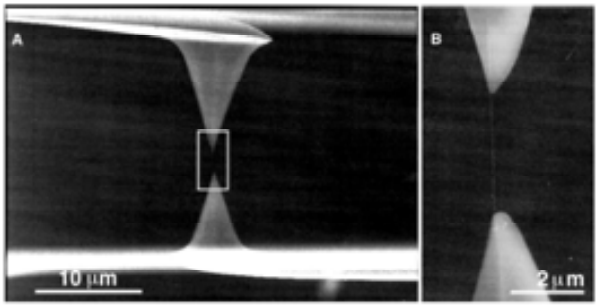

Fig. 2.5. Tensile-loading experiment with a MWNT which is mounted between two AFM tips. (a) SEM image of two AFM tips holding a MWCNT. The lower AFM tip in the image is on a soft cantilever. The deflection determines the force applied on the MWCNT. The top AFM tip is on a rigid cantilever that is driven upward to apply tensile load to the MWCNT. (b) High-magnification SEM image of the indicated region in a. Adapted from (43)**.**

2.5 Synthesis of Carbon Nanotubes

Carbon nanotubes are usually synthesized by arc discharge, laser ablation or chemical vapor deposition (CVD). Below the three methods are discussed.

Arc discharge – In this method an arc is generated between two electrodes by high current, so that in the presence of a catalyst graphitic material on one of them sublimates to the form of CNTs. In this way it is possible to obtain SWNT, MWNT, fullerenes, etc. (47).

Laser ablation – consists of vaporizing the graphitic material from the electrode by a laser pulse in an inert gas environment. Depending on the composition of the electrode this can result in synthesis of SWNT or MWNT. This is also the technique that produces the best quality CNTs. The nanotubes produced by laser ablation are purer (up to about 90% pure) than those produced in the arc process (48-50).

Chemical Vapor Deposition (CVD) – in this method a carbon containing gas is decomposed in high temperature and then reconstructed on the catalyst particle leading to CNT synthesis.

Laser-ablation for MWNT production and CVD for SWNT growth will be explained in more detail, since they are important for fabrication of the devices presented in this thesis.

2.5.1 Laser-ablation fabrication of MWNTs

In 1995, the Smalley group first reported the laser ablation technique as a way to synthesize SWNTs (51). Instead of an arc discharge, a laser was used to form a carbon vapor from a heated graphite rod. A carrier gas like helium, nitrogen or argon carries the carbon vapor from the 1200°C graphite rod to a water-cooled collector where the carbon vapor condenses to form SWNTs (Fig. 2.6). The graphite target can be mixed with catalyst particles like Co, Ni, Fe, Ti, Mn, and Cu in order to optimize the yield and the quality of the as-produced material. A variation of the SWNT diameter can be reached by changing the furnace temperature, the carrier gas, and the gas flow rate (52). In this technique, the diameter and diameter distribution of the produced SWNTs can be very accurately modified by changing the process parameters. Depending on the production conditions, SWNTs with a yield up to 80%, a mean diameter between 1 and 1.6 nm and a Gaussian diameter distribution with a variance better than 0.3 nm were obtained (52).

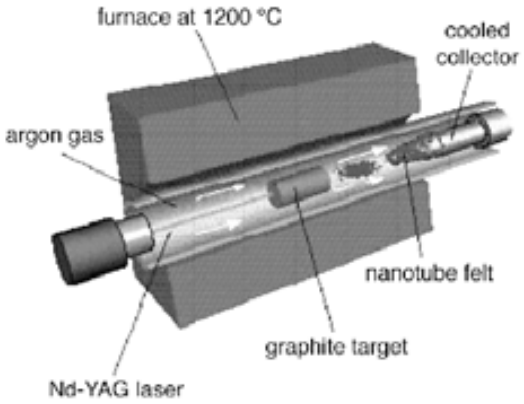

Fig. 2.6. Schematic representation of laser ablation process (51).

2.5.2 CVD growth

CVD (Fig. 2.7) is one of the most popular ways of synthesizing CNTs, mainly because its relatively low set-up cost and high production yield. The other advantage is that it allows the synthesis directly on the substrate, at the locations which can be predetermined by catalyst locations. It is also possible to control the diameter and the structure of CNTs by controlling the size and chemical composition of the catalyst particles (53).

However, the CNT synthesis by the means of CVD is still not perfectly understood. There are various hypothesis proposed by several groups, based on the reaction conditions and post-deposition product analyses. However those theories are often contradicting and therefore, no single CNT growth mechanism is well established till date.

The most general mechanism can be outlined as follows. Carbon-containing gases, when in contact with metal nanoparticles at high temperature, decompose into carbon and hydrogen species. Hydrogen flies away and carbon gets dissolved into the metal. After reaching the carbon-solubility

limit in the metal carbon precipitates out and crystallizes in the form of a CNT. The CNT has no dangling bonds and therefore is energetically stable.

Decomposition of carbon-containing gas is an exothermic process, so it releases heat to metal's exposed zone. On the other hand, carbon crystallization is an endothermic process, which absorbs heat from the catalyst nanoparticle. This precise thermal gradient inside the metal particle is supposed to keep the process on (53).

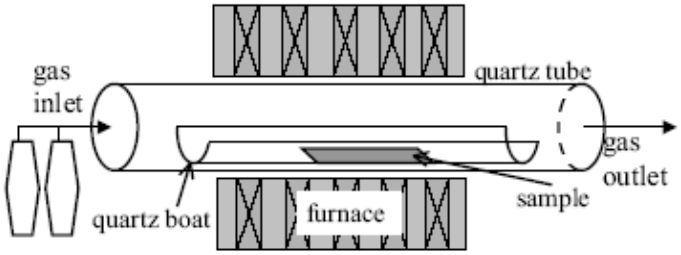

Fig. 2.7.Illustration of the CVD technique with a gaseous carbon source (54).

For synthesizing CNTs, typically, nanometer-size metal particles are required to enable hydrocarbon decomposition at a lower temperature than the spontaneous decomposition temperature of the hydrocarbon. Most commonly-used metals are Fe, Co, Ni, because of two main reasons: (i) high solubility of carbon in these metals at high temperatures; and (ii) high carbon diffusion rate in these metals. Besides, high melting point and low equilibrium-vapor pressure of these metals offer a wide temperature window of CVD for a wide range of carbon precursors.

Different carbon containing gases can be used for CNT synthesis, such as methane (CH_4) (55) (56), acetylene (C_2H_2) (57, 58), ethylene (C_2H_4) (59, 60), ethanol (C_2H_5OH) (61-64).

The gases influence CNT growth speed and structure, for instance the best structure is achieved using methane (55). Although the two main steps of the process are the catalyst activation and CNT growth, many of the recipes include also other steps, such as chamber conditioning and chamber cooling, as discussed below and shown in Fig. 2.8.

Chamber conditioning – in this step chamber is prepared for catalyst activation, as the temperature is increased in the inert gas ambient (Ar).

Catalyst activation – in this step the morphology of the catalyst is changed to form catalyst particles for the CNT growth. Also in the presence of H_2 the metal oxides formed on the catalyst particles are reduced. This step is performed in growth temperature, in the presence of inert gas and gases used to activate the catalyst particle, such as Ar and H_2, respectively.

CNT growth – in this step carbon-containing gas is introduced to the chamber, apart from the other gases, such as Ar and H_2. The optimum temperature and gas concentration allow CNTs to form.

Chamber cooling – in this step the carbon-containing gases are switched off and the temperature is reduced in the presence of an inert gas.

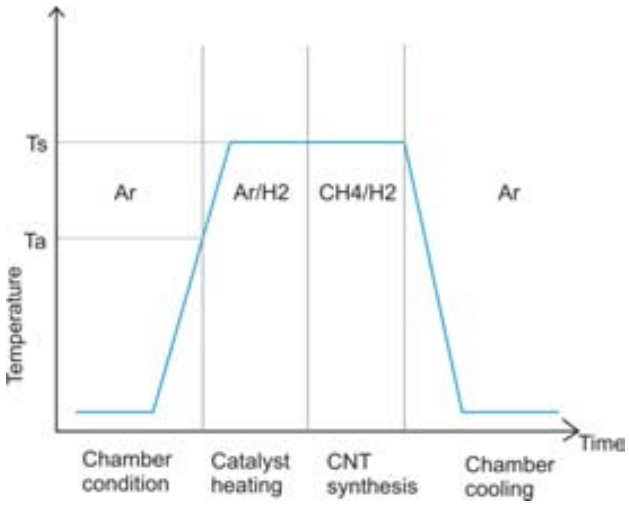

Fig. 2.8. Schematic of CNT synthesis. The process is composed of four steps. The schematic shows the gasses that are usually used in each step. Ta and Ts are the activation and synthesis temperature, respectively.

2.6 Graphene

For a long time it was believed that two dimensional crystals could not exist because they would be thermodynamically unstable (65). That is why since its discovery in 2004 by Novoselov *et al.* (66), rewarded with Nobel Prize in Physics in 2010, graphene has been the subject of intensive research. The graphene is a two-dimensional structure of carbon atoms which are arranged in a densely packed honeycomb crystal lattice. The connected carbon atoms share two electrons forming sp^2-bonds. The fourth valence electron of carbon occupies a p_z orbital. It can remain as a two-dimension structure, be wrapped up into fullerenes, rolled into nanotubes or stacked into graphite.

Graphene possesses unique electrical and mechanical characteristics. The energy bands ***E(k)*** of the graphene were calculated by P. R. Wallace in 1947 using tight-binding approach (67). As shown in Fig. 2.2. the Fermi surface is reduced to six points in which the conduction and valence bands meet., which are called *K-points*. Only two of the six points are not equivalent, these points are named *K* and *K'*. The dispersion relation near these points is conical, as shown in the Fig. 2.9. Because of this particular electronic structure the graphene is a semi-metal or zero-gap semiconductor. Thus, electrons and holes in graphene have zero effective mass and a velocity that is about 300 times slower than that of light. This linear dispersion relationship also means that quasi-particles in graphene display properties quite different to those observed in conventional three-dimensional materials, which have parabolic dispersion relationships.

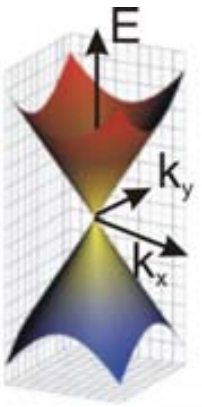

Fig. 2.9. Cone structure of the energy dispersion relation at low energies at the six Brillouin zone corners (54)**.**

Linear dispersion has lead to discovering some of the unusual properties of graphene, such as the anomalous quantum Hall effect and half-integer quantization of the Hall conductivity (68) (69). As far as spintronics is concerned, spin transport and spin precession over micrometre-scale distances have also been demonstrated in single graphene sheets at room temperature (70).

Graphene, as well as CNTs, is a material with unique mechanical proprieties, with the elastic stiffness of 340 N/m and breaking strength of 42 N/m (71). The value of Young's modulus is of 1 TPa and an intrinsic strength of 130 GPa, which places the graphene as the strongest known materials (72). Graphene is a promising choice for NEMS applications because it is very light and stiff. However, the main disadvantage is that, the fabrication process may introduce some residual in-plane stress, which results in unpredictable resonances and eigenmodes (73).

3. Nanoelectromechanical systems (NEMS)

3.1 Introduction

An electromechanical device is in principle a mechanical element (a cantilever, membrane, motor, etc.) that is controlled by an electronic circuit. Microelectromechanical systems (MEMS), typically made of silicon or its compounds, are currently used to make such diverse systems as electric current or light flow regulators (74), microscale mirrors arrays (75), accelerometers in crash airbags systems, RF electronic components, and sensors. The evolution from micro- to nano-electronics is paralleled by the more-recent miniaturization of mechanical devices, which are currently undergoing a transition from commercially-available MEMS to nanometre-scale electromechanical structures (NEMS). Miniaturization may have various advantages, such as increased speed and sensitivity, reduced power consumption, and improvements in the positional and spatial precision with which complex functions can be performed.

Micro- and nanoelectromechanical devices have been the subject of extensive research for a various years and generated much interest as their use in commercial applications has increased. NEMS also hold promise for a number of scientific and technological applications. In particular, they have been proposed for use in ultrasensitive mass detection (76), RF signal processing (77), and as a model system for exploring quantum phenomena in macroscopic systems (78). Among the various types of NEMS we will discuss motors and resonators, as they will be further explored in this thesis.

In fundamental science, mechanical resonators can be useful for studying quantum behaviour of macroscopic objects. To this end, a mechanical resonator has to be cooled to its ground state and its position has to be measured with great accuracy. Currently, various routes to reach these goals are being explored, with different techniques (optical or electrical) for sensitive position detection and cooling, such as sideband cooling and active feedback cooling.

In the last decade, many groups took the challenge to pursue the quantum limit of motion. The rapid progress in the development of sensitive optical techniques and mesoscopic electronics have led to detectors that have sensitivities that are approaching the quantum limit on position detection (79). Moreover, very recently the long-sought quantum mechanical behaviour of mechanical resonators was achieved in two different experiments. Science magazine research breakthrough of the year 2010 (80), the groups of Cleland and Martinis demonstrated quantum mechanical behavior of a 6 GHz mechanical resonator by coupling it to a superconducting flux qubit (81). At dilution refrigerator temperatures the first ten energy states of the harmonic mechanical oscillator (Fig.3.1a, b), including the ground state, could be probed. The measurement itself is performed on the superconducting qubit which acts as a two-level quantum system whose response changes when the occupation of the mechanical resonator state changes. A large coupling between the two quantum systems is achieved by using the piezoelectric properties of the mechanical resonator material.

In another approach Teufel *et al.* used a superconducting microwave cavity to actively cool a mechanical drum resonator (Fig. 3.2c) to such low temperatures that it is in the quantum mechanical ground state for most of the time (82). The drum resonator is integrated in the superconducting resonant circuit to provide strong phonon-photon coupling and the measurements use concepts developed for optical cavities to achieve efficient cooling.These two breakthrough experiments not only show that non-classical behaviour can be encoded in the motion of a mechanical resonator but also open a new exciting research field involving quantum states of motion.

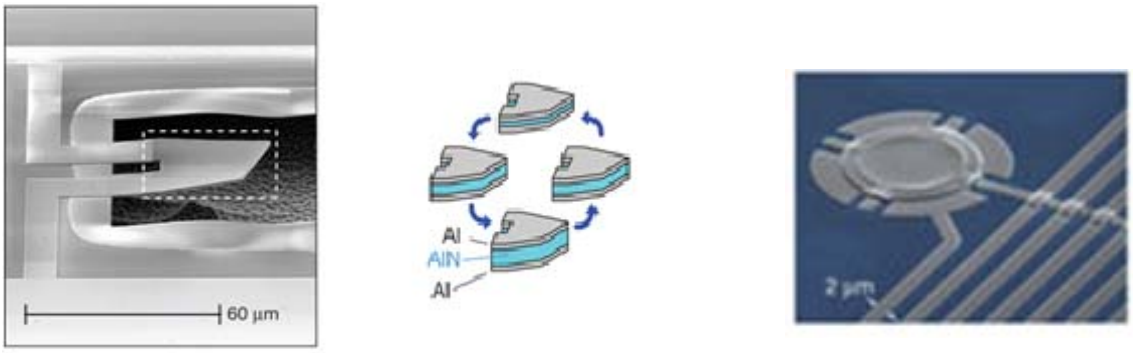

(a) (b) (c)

Fig. 3.1. (a) SEM image of a suspended resonator. The structure comprises, from bottom to top, 150 nm SiO_2, 130 nm Al, 330 nm AlN and 130 nm Al. The dashed box indicates the mechanically active part of structure. (b) Fundamental dilatational resonant mode for the mechanically active part of the resonator. The thickness of the structure changes through the oscillation cycle (81)**. (c) False-colour SEM image showing the aluminium (grey) electromechanical circuit fabricated on a sapphire (blue) substrate; a 15-µm-diameter membrane is suspended 50 nm above a lower electrode** (82)**.**

3.2 Carbon nanotube resonators

The top-down approach, typically used for MEMS fabrication, consists of etching parts of a larger structure, for example a thin film on a substrate, or by depositing material by means of evaporating or sputtering on a resist mask that is subsequently removed in a lift-off process. In both cases, patterning of resist is needed, which is done using optical or electron-beam lithography. Nowadays, state-of-the-art devices can reach down to 100 nm in thickness and width.

A major drawback of scaling down the Si resonators to increase their frequency is that the quality factor decreases, meaning a large dissipation of energy. This can be either due to increase in surface-to-volume ratio or due to micromachining process which can induce defects in resonators structure (74).

On the contrary, for bottom-up devices, based on inorganic nanowires, carbon nanotubes and graphene high quality factor Q is expected. This, combined with low mass, makes them ideal building blocks for nano-electromechanical systems

Electromechanical resonators are a key element in radio-frequency telecommunication devices and therefore CNT resonators can readily find some important industrial opportunities. Due to their nanometer-scale diameter, ultra-low mass and exceptional electrical and mechanical properties,

individual SWNTs are possible candidates as the central vibrating element for NEMS working in MHz and GHz range (83). However, direct measurements of intrinsic high-frequency electrical response of individual SWNT remains challenging due to parasitic capacitance and impedance mismatch. Recently, frequency mixing and digital demodulation was proposed to use for measuring vibrations of CNT resonator in transistor geometry. With that recent progress all-electronic actuation and readout can be achieved with transfer rate of 10 kbps, which is compatible with GSM requirement (84).

The break-through in CNT resonators came with the experiment of Sazonova *et al*. where the electrical actuation and detection of the guitar-string-like oscillation modes of doubly clamped nanotube oscillators were reported mixing technique became increasingly popular for motion detection of CNT resonator (85).

The motion of SWNT resonator was actuated and detected using the electrostatic interaction with the gate electrode underneath the tube (Fig.3.2c). The AC voltage component applied on the back-gate produced a periodic electric force, which set the nanotube into motion. To detect the vibrations of the nanotube, the transistor properties of semiconducting and small-bandgap semiconducting carbon nanotubes was employed, that is that the conductance change is proportional to the change in the induced charge on the tube. The nanotube was used as a mixer, which helped avoid unnecessary complications due to capacitive currents between the gate and the drain electrodes. The magnitude of the current is given by the product of the AC voltage on the source electrode and the modulated nanotube conductance (Fig.3.2a).

The DC voltage component on the back- gate can also be used to tune the tension in the nanotube and therefore the oscillation frequency, i.e., the resonant frequency shifts upward as the magnitude of the DC gate voltage is increased, as shown in Fig. 3.2b.

To understand this frequency dependence on DC gate voltage (V_{DC}) various simulations were performed. To summarize, for no static electric force on the nanotube the resonance frequency is determined by the bending rigidity of the nanotube and is approximately that of an equivalent doubly clamped beam with no tension. At small gate voltages there is a static electric force downward on the nanotube producing a tension $T \sim (V_{DC})^2$, which shifts the resonant frequency of the nanotube, $\Delta f \sim T \sim (V_{DC})^2$. At intermediate V_{DC} the electrostatic force overcomes the bending rigidity and the nanotube behaves as a hanging chain; the profile of the tube forms a catenary. In this regime, the resonance frequency is given by $\Delta f \sim \sqrt{T} \sim V_{DC}$. In the large electrostatic force regime, the nanotube behaves as an elastic string - the extensional rigidity becomes dominant. In this regime, the resonance frequency is given by $\Delta f \sim \sqrt{T} \sim (V_{DC})^{2/3}$. The transition point from the bending-dominated regime to the catenary, and from the catenary to the stretching-dominated regime, depends on the amount of slack in the nanotube. One, two or all three described regimes may be relevant for a particular device.

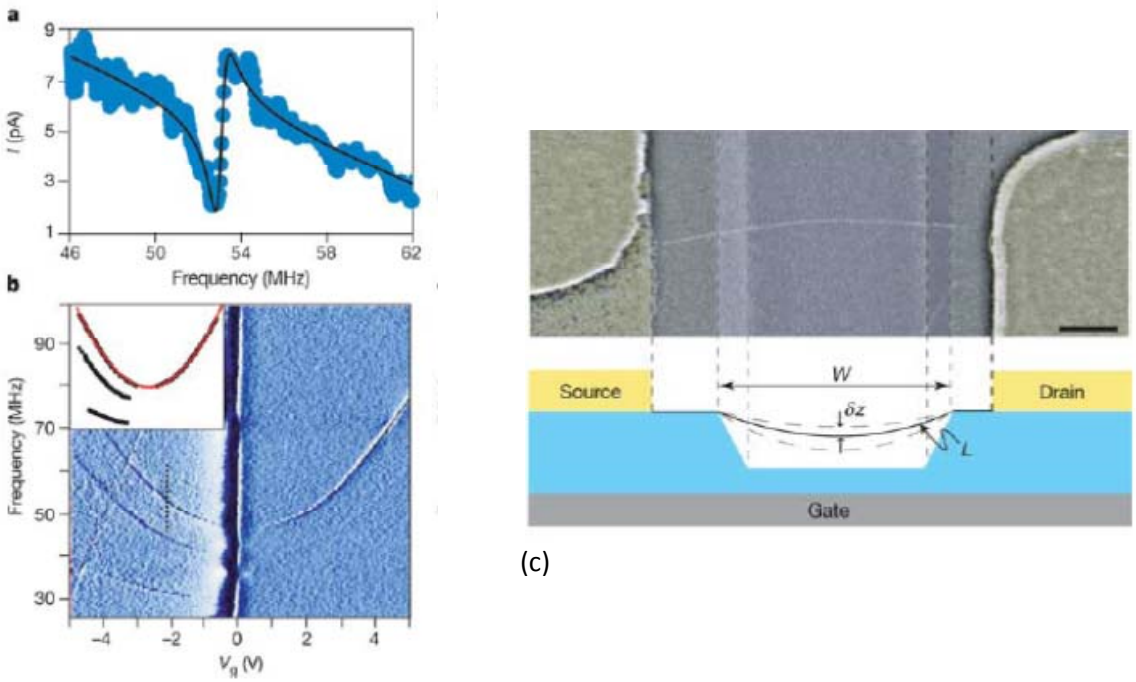

(c)

Fig. 3.2. (a) Detected current as a function of driving frequency. The solid black line is a lorenzian fit to the data with an appropriate phase shift between the driving voltage and the oscillation of the tube. The fit yields the resonance frequency f_0 = 55 MHz, and quality factor Q = 80. (b) Detected current as a function of gate voltage and frequency for two of the measured devices. (c) A false-color SEM image of a suspended device (top) and a schematic of device geometry (bottom). Scale bar: 300 nm (85).

Table 3.1 shows the properties of mechanical resonators that have been made so far using bottom-up fabricated devices, based on carbon materials and nanowires (42). All the NEMS posses relatively high resonance frequencies, between 300 MHz and 3 GHz. If we compare the quality factors and zero-point motion of these devices, it is clear that the nanowire performance is comparable to top-down fabricated devices since their thickness is of the order of 10-100 nm, about the size of the smallest top-down fabricated devices.

On the other hand, due to their low mass and high strength the frequencies of carbon-based resonators are high and their zero-point motion large. This means that when cooled to dilution refrigerator temperatures, carbon-based resonators would exhibit relatively large amplitude zero-point fluctuations in the ground-state. However, position detectors for bottom-up NEMS are still not as sophisticated as those for the larger top-down counterparts and non-driven motion at cryogenic temperatures (zero-point motion) nor active cooling is yet to be reported for carbon-based NEMS.

Group	Type	f_R (MHz)	Q_{RT}	Q_{cryo}	T_{min} (K)	ℓ (μm)	m (kg)	u_0 (pm)
Cornell	CNT	55	80		300	1.75	$7.4 \cdot 10^{-21}$	4.52
Delft	CNT	60	100		300	1.25	$1.0 \cdot 10^{-20}$	3.66
Berkeley	CNT	350	440		300	0.5	$5.3 \cdot 10^{-20}$	0.67
ICN	CNT	3120	8		300	0.77	$5.8 \cdot 10^{-20}$	0.22
ICN	CNT	154	20		300	0.265	$1.1 \cdot 10^{-19}$	0.69
ICN	CNT	573	20		300	0.193	$4.0 \cdot 10^{-22}$	6.03
ICN	CNT	167	200	2000	5	0.9	$1.4 \cdot 10^{-21}$	6.03
Berkeley	CNT	328.5	1000		300	0.205	$1.6 \cdot 10^{-21}$	4.01
CalTech	CNT	230		200	6	0.45	$4.8 \cdot 10^{-22}$	8.73
Purdue	CNT	0.9	3		300	12.6	$4.1 \cdot 10^{-16}$	0.15
Chalmers	CNT	62	50		300	2.05	$2.2 \cdot 10^{-17}$	0.08
Delft	CNT	360		120000	0.02	0.8	$5.3 \cdot 10^{-21}$	2.09
ICN	CNT	50	40	600	4	1	$1.3 \cdot 10^{-21}$	11.41
U. Wash.	CNT	410			64			
U. Illinois	CNT	4	240		300	6.2	$5.9 \cdot 10^{-18}$	0.59
LPMCN	CNT	73.6	160		300	2	$8.5 \cdot 10^{-21}$	3.66
CalTech	Pt NW	105.3		8500	4	1.3	$4.0 \cdot 10^{-17}$	0.045
CalTech	Si NW	215		5750	25	1.6	$1.9 \cdot 10^{-17}$	0.045
U. Penn.	GaN NW	2.235	2800		300	5.5	$1.9 \cdot 10^{-16}$	0.141
Yale	GaN NW	8.584	1008		300	2.04	$1.6 \cdot 10^{-17}$	0.245
Lyon	SiC NW	0.043	159000		300	93	$9.8 \cdot 10^{-15}$	0.141
Alberta	Si NW	1.842	4200		300	5.2	$2.4 \cdot 10^{-17}$	0.437
Alberta	Si NW	1.842	2000	10000	77	11.2	$4.6 \cdot 10^{-16}$	0.099
Penn. State	Si NW	1.928	4830		300	11.8	$2.4 \cdot 10^{-15}$	0.043
Penn. State	Rh NW	7.186	1080		0.3	5.8	$4.4 \cdot 10^{-15}$	0.016
CalTech	Si NW	96	550		300	1.8	$5.3 \cdot 10^{-18}$	0.129
Tsinghua U.	ZnO NW	26	5		300	12	$1.9 \cdot 10^{-14}$	0.004
U. Illinois	Si NW	0.208	10000		300	14.4	$5.1 \cdot 10^{-17}$	0.887
U. Mich.	SnO_2 NW	59	2200		300	2.5	$2.2 \cdot 10^{-16}$	0.025
Madrid	Si NW	2.2	2000		300	7.5	$5.5 \cdot 10^{-16}$	0.083
Cornell	SLG	70.5	78		300	1.1	$1.4 \cdot 10^{-18}$	0.287
ICN	FLG	32	64		300	2.8	$2.7 \cdot 10^{-17}$	0.098
Cornell	FLG	160	25		300	4.75	$4.5 \cdot 10^{-16}$	0.011
NRL	FLGO	57.6	3000		300	2.75	$7.8 \cdot 10^{-17}$	0.043

Table 3.1. Overview of recent experiments with bottom-up resonators. Several types of resonators are used: carbon nanotubes (CNT), nanowires (NW), single-layer graphene (SLG), and few-layer graphene (FLG) or graphene oxide (FLGO) sheets. The table shows the resonance frequency f_R and quality factors at room and cryogenic temperature (Q_{RT} and Q_{cryo} resp.). T_{min} is the lowest temperature at which the resonator is measured. m is the mass of the resonator and ℓ is its length. From these data, the zero-point motion u_0 is calculated (42).

Nevertheless impressive progress in understanding the electromechanical properties of bottom-up resonators has been made in recent years using so-called self-detecting schemes. In these schemes, the nanotube both acts as the actuator and detector of its own motion. Ultra-high quality factors up to 120 000 have now been demonstrated for carbon nanotube resonators at low temperatures (86), ultra-high operation frequency in range of GHz (87-89), as well as a strong coupling between electron transport and mechanical motion (90-91).

Recently, damping of mechanical resonators based on carbon nanotubes and graphene sheets (Fig. 3.3a, b) was investigated by Eichler *et al.* (92). It was found that damping in nano-scale systems was better described by a nonlinear instead of the common linear damping force. Linear damping model (with damping force $\gamma dx/dt$, where γ is the damping coefficient, x is the deflection of the resonator and t is time) have been used to describe the damping of resonators with dimensions that range from the metre-scale down to a few tens of nanometres.

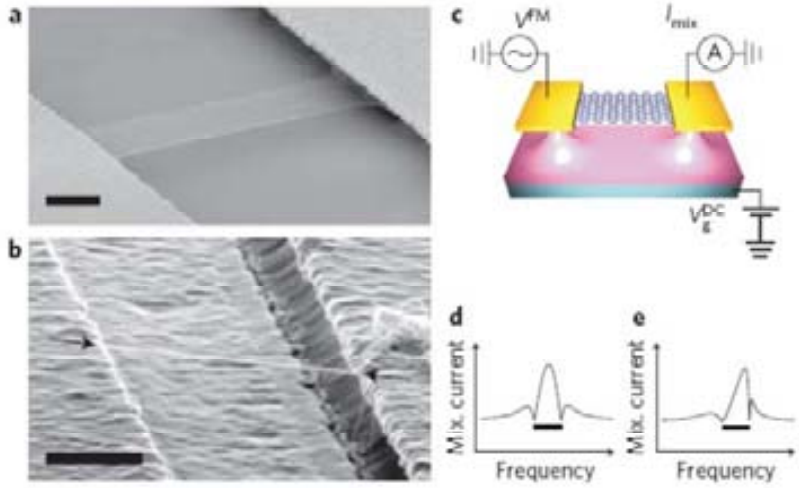

Fig. 3.3. (a) Scanning electron micrograph of a suspended single-layer graphene sheet with Au contacts. Scale bar, 500 nm. (b) Scanning electron micrograph of a nanotube grown by chemical vapor deposition over a prefabricated trench between two W/Pt contacts. The nanotube is marked by black arrows and white dotted lines. Scale bar, 500 nm. (c) Schematic of the actuation/detection setup. (d), (e), Schematic of the frequency response of the mixing current. The separation between the two minima (black bar) corresponds to the resonance width Δf. The resonance peak becomes asymmetric in the presence of a Duffing nonlinearity (e) (92).

However, this approach breaks down at the level of nanotube and graphene resonators and their behavior can instead be explained by a nonlinear damping force $\eta x^2 dx/dt$, where η is the coefficient of nonlinear damping. It was also demonstrated that the quality factor strongly varies with the driving force. By tuning the driving force it was possible to achieve the largest Q factor for a graphene resonator (100 000 at 90 mK).

Two explanations of the origin of the nonlinear damping were proposed: a standard dissipation channel (such as contamination), which alone would lead to purely linear damping, and geometrical nonlinearity, which can arise from the elongation of a doubly clamped resonator on deflection. The origin of the damping however remains an open question.

Nanoelectromechanical systems have been proposed for highly sensitive mass detection of neutral species and significant progress has been made in using nanofabricated CNT resonators for mass sensing (93-97).

In 2008 Jensen *et al.* reported measurements of a double-walled CNT resonator as a mass sensor (96). The experiment was performed in TEM chamber, which enabled precise extraction of the mass of the device. The frequency of the device was monitored while Au atoms were sent on the nanotube and are detected with sensitivity of $1.3 \cdot 10^{-25}$ kg/Hz (0.4 Au atom/Hz).

Later in 2008 mass sensing experiments using SWNT resonator in transistor configuration were reported by Lassagne *et al*. (94) and Chiu *et al.* (95). In the first experiment Cr atoms are evaporated on the nanotube in high vacuum and room temperature. The responsitivity of the device was reported to be 11 Hz/10^{-24}kg. In the second experiment Ar and Xe atoms were evaporated on the CNT resonator in 6K, and by measuring the shifts in resonance frequency mass of the adsorbed atoms as well as CNT mass were determined (Fig. 3.4).

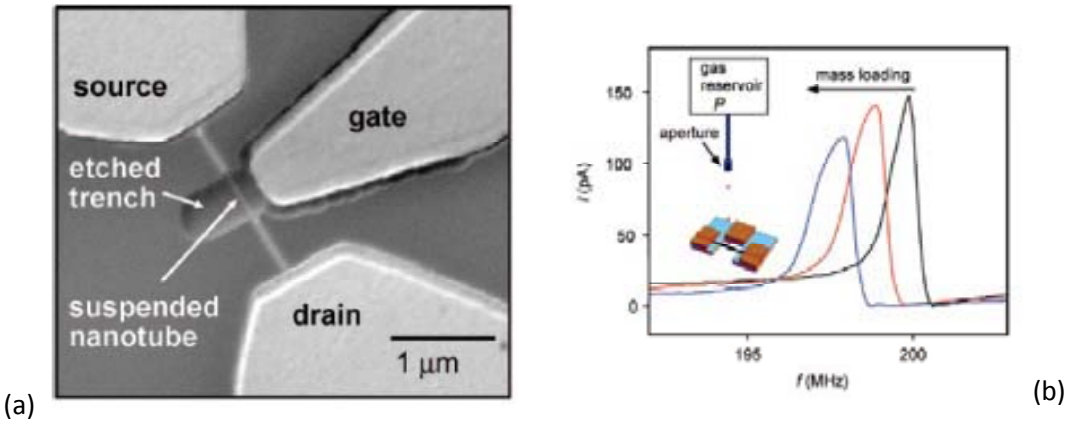

(a) (b)

Fig. 3.4. (a) SEM image of a suspended nanotube resonator used for mass sensing. (b) Main panel: mixing current *I* versus drive frequency *f* for a resonator device during mass loading by Xe. The black curve shows the initial resonance, the red curve after mass loading for ≈ 600 s, and the blue curve after mass loading for ≈ 1600 s. Inset: schematic diagram of the experimental setup for mass loading. Adapted from ref. (95)**.**

The ultimate mass sensing experiments with a resolution of 1.7 yg (1 yg = 10^{-24} g), which corresponds to the mass of one proton, were reported by Chaste *et al.* in 2012 (98). This gives an opportunity of determining mass of large molecules with sub-atomic precision, as well as monitoring chemical reactions in real time.

On the contrary, MWNT-based resonators have not attracted so much attention in the recent years. Theoretical simulations were performed with DWNTs in order to verify their vibrational behavior (99). The results showed that fundamental frequencies of double-walled carbon nanotubes are about 10% lower than those of single-walled carbon nanotubes of the same outer diameter.

For the vibration of double-walled carbon nanotubes, non coaxial vibration modes were predicted. This phenomenon was first reported by Yoon *et al.* (100), based on an elastic continuum multishell model. However, the vibration modes associated with the fundamental frequencies are almost coaxial, and non-coaxial vibrations are excited at higher frequencies. The non-coaxial vibration of

double-walled nanotubes begins at the third resonant frequency and does not significantly diminish the value of double-walled nanotubes as high-frequency nanoresonators (99).

The *in situ* observation of a multi-walled nanotube resonance was conducted with a scanning electron microscope (101). The potential of the MWNT as an ultrasensitive mass sensor was investigated, with a result of the nanotube responsivity of 1668.49 Hz/ag (1 ag = 10^{-18} gram). Even though this value is significantly lower than for SWNTs, it may be enough for some chemical and biological sensing applications.

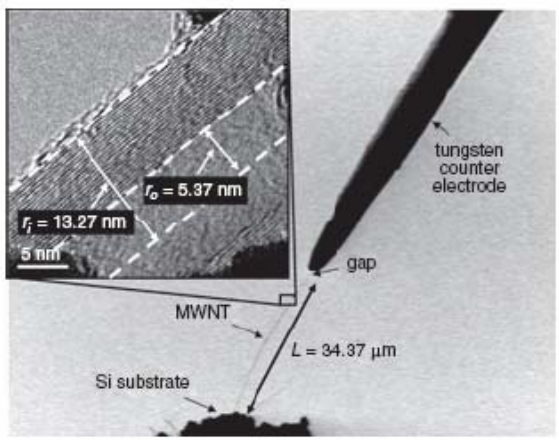

Fig. 3.5. Experimental setup of individual MWNT resonator, and SEM and TEM micrographs of individual MWNT resonator and its structural parameters. (101).

Graphene, being a single layer of carbon atoms, is the prototypical two-dimensional membrane. Its unparalleled strength, small mass per unit area, ultra-high aspect ratio, and unusual electronic properties make it an ideal candidate for NEMS. Resonators made of single and multi-layer graphene were reported by the group of McEuen in 2007 (102). Graphene flakes were deposited directly on top of the pre-fabricated trenches. Vibrations with fundamental resonant frequencies in the megahertz range were actuated either optically or electrically, by applying an AC voltage on back-gate, and detected optically by interferometry. Graphene resonators with electrical readout were reported in 2009 (103). Also CVD grown graphene has attracted a lot of attention, as drums (104) and large arrays of resonators were fabricated using transfer technique (105).

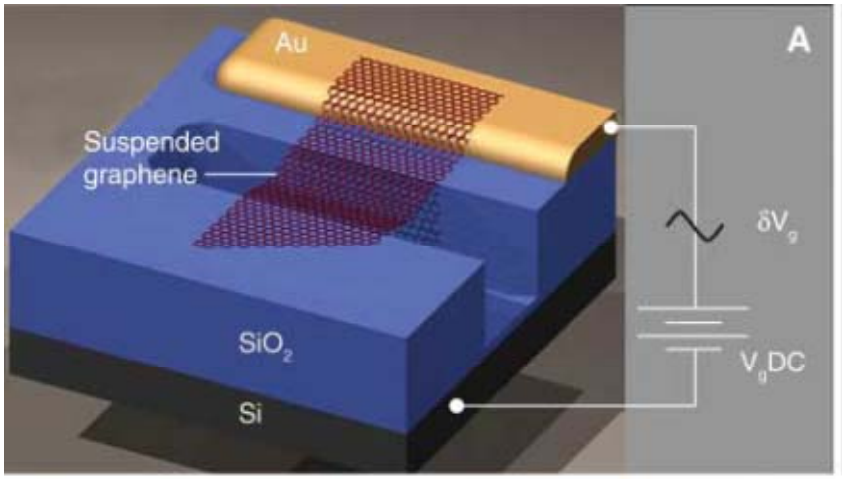

Fig. 3.6. Schematic of a suspended graphene resonator (102).

3.3 Carbon nanotube motors

As the nanometer length scale devices are being approached nowadays an entirely new set of phenomena are becoming relevant, which provide great challenges to the further miniaturization of devices. The precise atomic and electronic structure of devices, the chemical reactivity of its components and the quantum behavior are all issues of increasing importance at this scale. Engineering useful nanoscale mechanical devices will require an understanding of these effects and their impacts on device efficiency and reliability. Whereas micro-fabricated motors, actuators and oscillators are typically manufactured by conventional semiconductor processing techniques, their nanoscale counterparts are more difficult to realize.

Multi-walled carbon nanotubes (Fig. 3.7) offer a unique opportunity to construct nano-scale machines. They can be fabricated with near structural perfection, and their resistance to

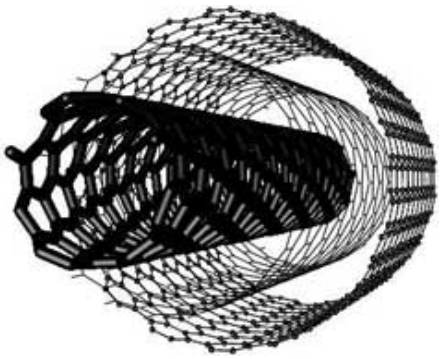

Fig. 3.7. Schematic of a MWNT as a key element for NEMS allowing two degrees of freedom, on one hand translation along the MWNT axis and on the other hand rotation around the MWNT axis (106).

deformation and the smoothness with which coaxial tubes can move relative to one another suggest that they could be ideal materials from which to build nanoscale motors and bearings. In addition, their one-dimensional tubular shape offers a natural track for motion. This restricts the motion (typically translation and/or rotation) to only a few degrees of freedom, much as bearings do in everyday machines. The tubular track has been the key component for the fabrication of nanotube-based switches (107), rotors (108-109), mass conveyors (110-113) and motors (114).

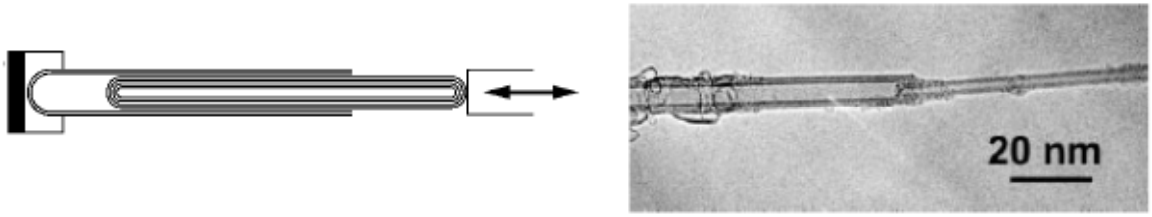

(a) (b)

Fig. 3.8. (a) Schematic representation of telescoping a MWNT by attaching a nanomanipulator to an open end of the MWNT. (b) TEM image of a telescoping nanotube (45)**.**

One of the early examples of an artificial MWNT-based NEMS is based on a telescoping structure made of multi-walled carbon nanotube (45). In the experiment of Cumings and Zettl one end of the outer shells was opened and a movable nanomanipulator was attached to the inner shells inside of a high-resolution TEM chamber. The schematics and TEM images from the experiment are shown in Fig. 3.8. In such a way it was possible to study the bearing properties of the system by pulling and pushing the core outside and inside the outer shells. The extruded core after releasing fully retracted to its previous position due to the restoring force of the van der Waals interaction acting on the extruded core shells. The resulting conclusosion is that the intershell resistance force against sliding of the core is negligibly small. An ideal low-friction and low-wear bearing demonstrated in this experiment has profound implications on the path to create various nanomechanical systems and has been viewed as one of the milestones in the roadmap of molecular manufacturing (115).

The ultra-low inter-shell friction in MWCNTs allowed fabrication of CNT-based nanomotors (108, 109, 114). First of all, Fennimore *et al.* built the first actuator that was a true MWNT-based NEMS device, in that it fully integrated electronic control and mechanical response. This distinguishes it from the previous related MWNT-based mechanical devices which require relatively large and complex external control systems such as the piezo-driven manipulator to achieve operation (45).

Fig. 3.3a shows the conceptual design of the electromechanical rotational actuator. The rotational element (R), a rectangular metal plate, is attached transversely to a suspended support shaft. The support shaft ends are fixed to electrically conducting anchors (A1, A2) that rest on the oxidized surface of a silicon chip. The rotor plate assembly is surrounded by three fixed stator electrodes: two ‘in-plane’ stators (S1, S2) are horizontally opposed and rest on the silicon oxide surface, and the third ‘gate’ stator (S3) is buried beneath the surface. The key component in the assembly is a single multi-walled carbon nanotube, which serves simultaneously as the rotor plate support shaft and the electrical feedthrough to the rotor plate; most importantly it is also the source of rotational freedom. It was possible to reliably flip the rotor plate alternatively between the extreme horizontal positions and to rotationally drive the actuators for various of cycles (Fig. 3.3b), with no apparent fatigue or degradation in performance.

(a)

(b)

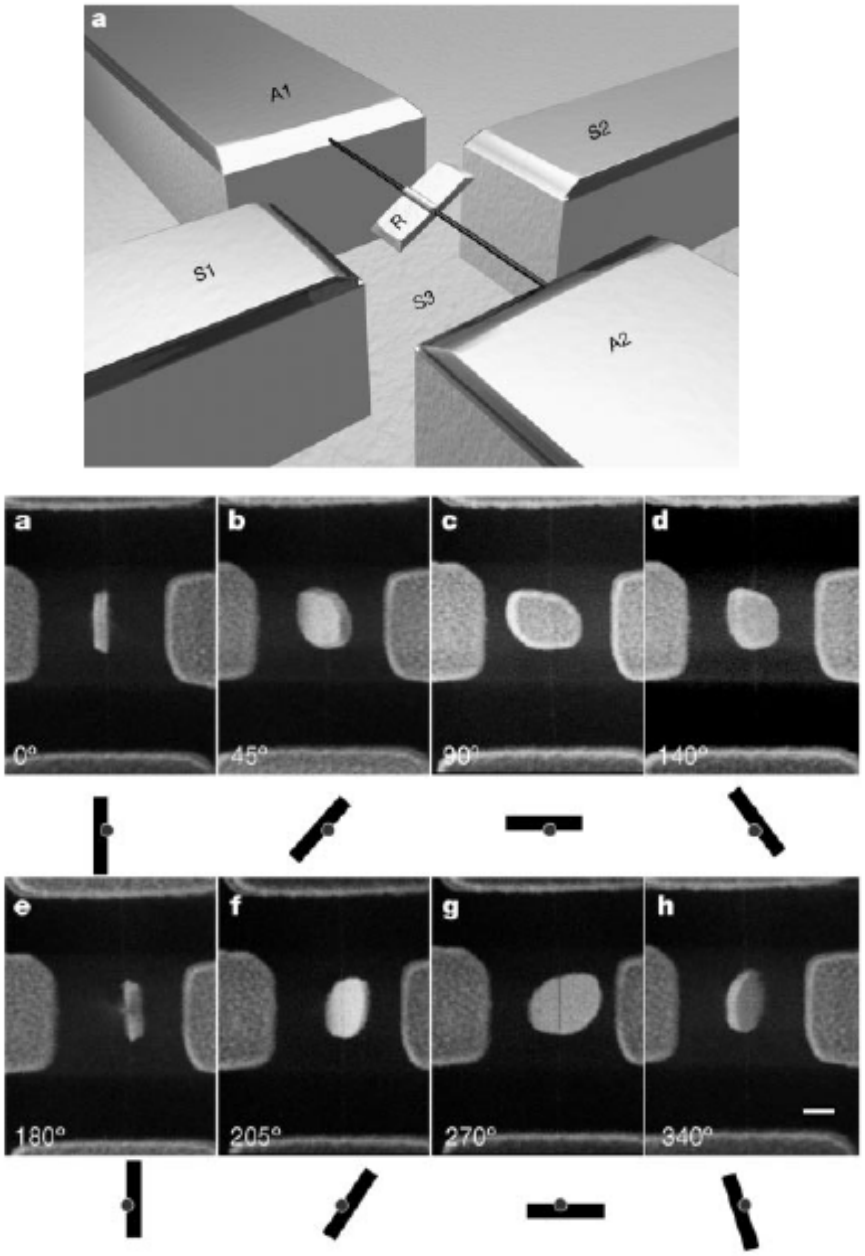

Fig. 3.9. (a) Conceptual drawing of the nanoactuator fabricated by Fennimore et al. (b) Series of SEM images showing the actuator rotor plate at different angular displacements. The MWNT runs vertically through the middle of each frame. The schematic diagrams located beneath each SEM image illustrate a cross-sectional view of the position of the nanotube/rotor plate assembly. Scale bar: 300 nm (108).

Another type of motor, recently fabricated by Barreiro *et al.* is the so-called thermal gradient motor (114). It consists of a mobile element, which can move along and/or rotate around the axis of the suspended nanotube, as shown in the Fig. 3.4a. The mobile metal cargo is attached to at least one short shell that can slide with respect to the other shells. To engineer the MWNT electrical breakdown technique was used, which does not remove the shells below the metal cargo, probably because the metal plate efficiently absorbs the heat generated in this portion of the tube, which prevents the tube oxidation in this part.

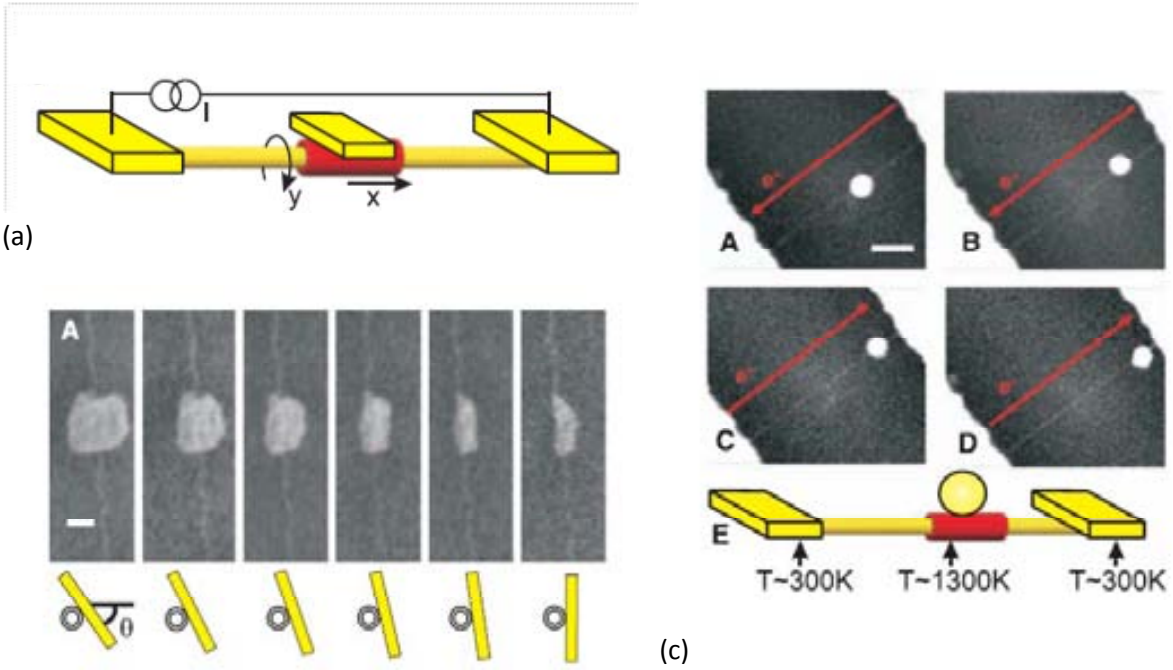

(a)

(b)

(c)

Fig. 3.10 (a) Schematic of a thermal gradient motor (b) Rotational motion. Top-down SEM images where the gold cargo is rotating stepwise. Scale bar, 100 nm. The cross sectional schematics below each SEM image represent the rotation of the plate around the nanotube (c) Translational motion. A to D: Top-down SEM images where the gold cargo (sphere) is moving along the nanotube. The direction of motion remains the same as the polarity of the current (red arrow) is reversed. Scale bar in (A), 400 nm. (E) Schematic illustration of the temperature along the nanotube caused by Joule heating. The motion of the cargo is driven from the hot spot to the cold region and is unaffected by the inversion of the current polarity. Adapted from (114)**.**

The motion was attributed to the large thermal gradient along the nanotube. The gold cargo was often observed to melt, which is indicative of a very high temperature (approximately 1200°C). However, the nanotube does not heat up homogeneously, because the heat is evacuated through the electrodes (Fig. 3.4b, c). The hottest spot of the device is in the middle of the suspended nanotube, while the temperature at the interface with the electrodes is expected to be near room temperature. In the presence of a thermal gradient along the nanotube (~1K/nm for the discussed device), there is a net current of phononic excitations moving from the hot spot toward the cooler regions, in that case from the centre of the suspended nanotube toward the electrodes. These phonons interact with the cargo and transfer momentum. As a consequence, the cargo moves towards the closest electrode.

The shape of the thermal gradient is independent of the direction of the electron current, which explains why the cargo does not change direction upon reversing the electron polarity. As potential application, thermal gradients could be used to drive the flow of fluids inside nanotubes or in nanofluidic devices or used for drug delivery by nanosyringes.

4. High-frequency nanotube mechanical resonators

This chapter is based on article in Appl. Phys. Lett. 99, 213502 (2011)

4.1 Introduction

Mechanical resonators have attracted considerable interest as ultra-sensitive detectors of mass (93-96) and force (92, 116, 117), and as macroscopic objects whose motion can be cooled to the quantum limit (81, 82, 118). A key parameter in these experiments is the resonance frequency f_0, which is often desirable to have as high value as possible. For instance, a high resonance frequency is expected to improve the sensitivity of mass sensing; it also makes the temperature at which quantum phenomena appear within reach of standard refrigerators.

Flexural motion at f_0 higher than 1 GHz was detected using singly and doubly clamped micro-fabricated resonators (119, 120). Single-wall carbon nanotubes have allowed the fabrication of nanoelectromechanical resonators with excellent properties (84-86, 93-96, 121, 122) but the highest reported resonance frequency is rather modest (below 600MHz).

In this chapter, we report on a simple and reliable method to fabricate high-frequency nanotube resonators where f_0 can be as high as 4.2 GHz for the fundamental eigenmode. The high-frequency resonators are achieved using a device layout in which the suspended nanotube is very short and under tension.

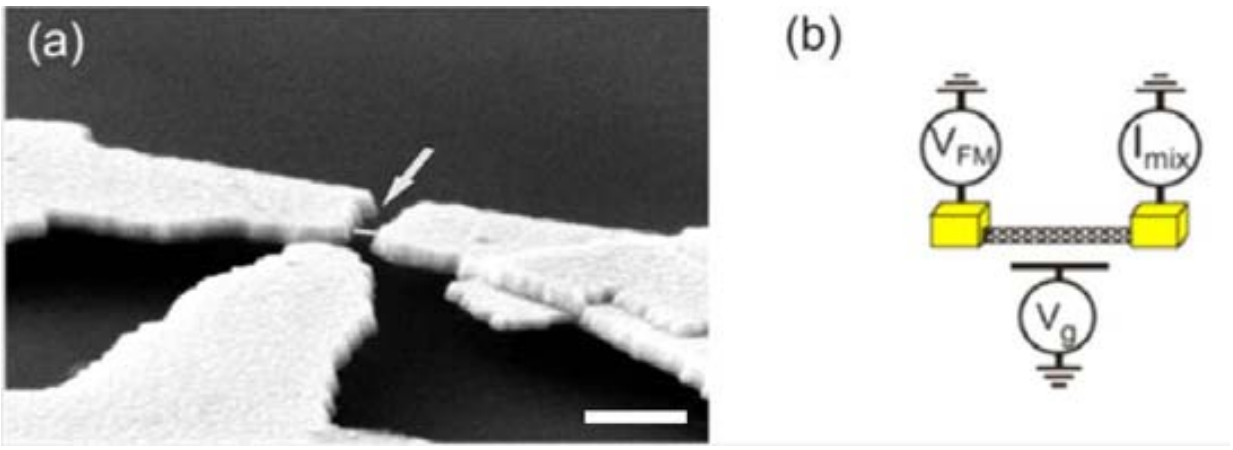

Fig. 4.1. (a) SWNT resonator after removing supporting oxide. A line was imposed in graphic program on top of SWNT for better visibility. Scale bar: 500 nm. (b) Schematic of the actuation/detection setup. A frequency modulated voltage V_{FM} is applied to the source of the device and the motion is detected by measuring the mixing current I_{mix} at the drain. Constant voltage V_g applied on the gate induces tension in the nanotube.

4.2 Fabrication and measurements

Nanotube resonators were fabricated using conventional nanofabrication techniques, as described in Annex A. First of all, CNTs were grown by chemical vapor deposition on a highly resistive silicon wafer coated with a 1 µm thick oxide layer. In order to achieve high-frequency resonators, care was taken to:

(1) design contact electrodes with a short separation of approximately 100 nm;

(2) select straight segments of nanotubes by atomic force microscopy (AFM) to minimize slack once the nanotube is suspended.

We used electron-beam lithography and Cr/Au evaporation to pattern contact electrodes as well as a side-gate electrode. The nanotubes were suspended by etching ~100 nm of the oxide with fluoridic acid (Fig. 1a and see *Annex A* for detail of fabrication).The measurements were performed in ultra-high vacuum chamber in temperature of ~4 K and pressure of order of 10^{-8} mbar. The motion was driven and detected using the frequency modulation (FM) mixing technique (Fig. 1b and *Annex B*).

4.3 Discussion

Figure 4.2a shows two mechanical resonances at 4.2 and 11 GHz for a device whose contact electrodes are less than 100 nm apart. The resonances consist of a central peak flanked by two lobes, which is consistent with the typical line shape of a mechanical resonance in FM measurements. These resonances correspond to flexural eigenmodes, since other eigenmodes are expected to have much larger resonance frequencies (f_0 = 240 GHz for the lowest longitudinal and twisting eigenmodes of a 110 nm long nanotube (123)). We assign the 4.2 GHz resonance to the fundamental eigenmode, since it is the lowest in frequency and possesses the highest current. Accordingly, the 11 GHz resonance corresponds to a higher-order eigenmode, which is likely the 3rd mode, since the 2nd mode is expected to be driven weakly due to the symmetry of the device (the gate electrode is symmetrically placed with respect to the nanotube). The ratio between the 11 and the 4.2 GHz frequencies is rather close to 3, the value expected for a nanotube under tension. One reason why the ratio is not exactly 3 could be related to the influence of the clamping electrodes.

We confirmed the mechanical origin of these resonances by depositing xenon atoms onto the nanotube *in situ* and observing a drop in the resonance frequencies (Fig. 4.2e). The reason for the drop in f_0 is the adsorption of Xe atoms onto the nanotube surface which increases the mass of the mechanical resonator. Both before and after the adsorption of Xe atoms, the maximum deviation in f_0 was 0.45MHz (obtained from 22 measurements of the resonance), which is much less than the 10.5 MHz drop in f_0 due to the adsorption of Xe atoms. Another signature of the mechanical origin is the strong temperature dependence of f_0 (Fig. 4.2c); we indeed studied dozens of mechanical resonators with the FM mixing technique and occasionally observed some low-amplitude resonances whose origin was purely electrical, but whose f_0 would not change with temperature. Figure 4.2d shows that the quality factor *Q* increases upon lowering temperature and reaches 1200 at 4K and for a driving excitation V_{FM} = 4mV. We emphasize that the quality factor varies with the driving excitation (*Q* increases by a factor of 3 upon increasing V_{FM} from 1 to 10 mV). It is not clear

whether this variation is due to nonlinear damping (92, 122) or is related to Joule heating (which is induced by the large applied voltage).

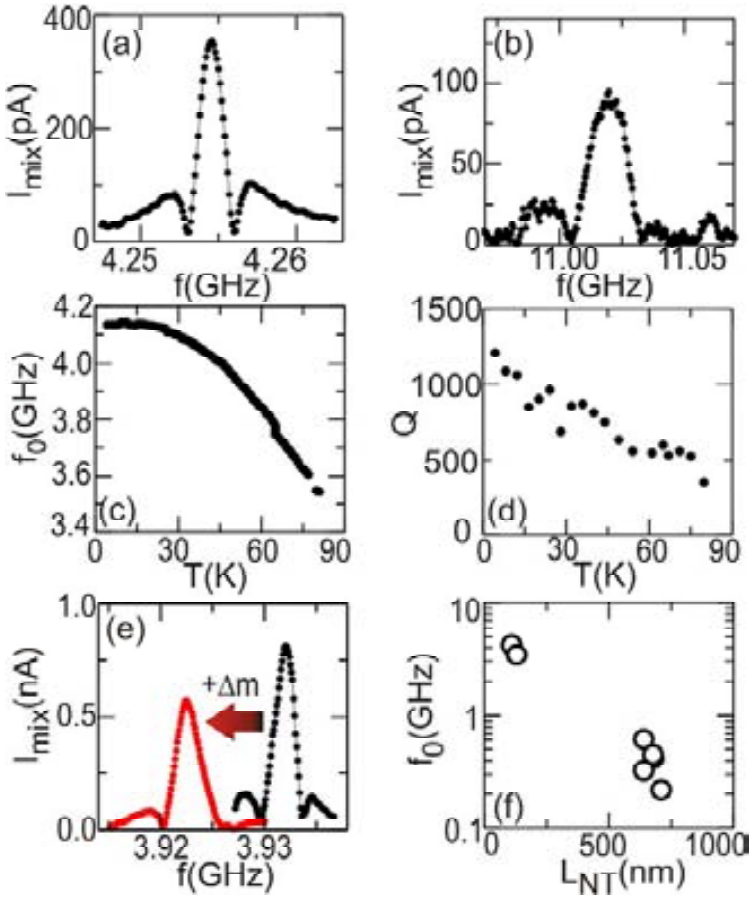

Fig. 4.2. (a) and (b) Mechanical resonances measured at 4K. The V_{FM} amplitude is 5 mV in (a) and 10mV in (b). (c) and (d) Temperature dependence of the resonance frequency and of the quality factor for the resonance in (a) measured with V_{FM} = 4 mV. (e) Frequency shift of the resonance after adding Xe atoms onto the resonator. Xe atoms were admitted in the sample chamber from a gas reservoir at 300K using a pinhole doser. (f) Resonance frequency as a function of the nanotube length at 4K for different resonators.

Two important parameters that allow us to tune the resonance to high frequency are the length of the suspended nanotube segment (L_{NT}) and the temperature. Indeed, Fig. 4.2f displays the resonance frequency of the fundamental eigenmode at 4K for the 7 resonators that were fabricated with the method described above; the resonance frequency increases as L_{NT} decreases, as expected for mechanical resonators. In addition, the resonance frequency dramatically increases upon lowering T as shown in Fig. 4.2c and in the upper curve in Fig. 4.3a. The latter behavior is related to the T dependence of the tensile stress within the nanotube: in our device layout (inset of Fig. 4.3a), the suspended parts of the clamping Au electrodes contract upon lowering T, thus they increase the tensile stress within the nanotube (the estimated contraction of Au from 300 to 4K is$|\Delta l_{Au}|$ ≈1.6 nm and is larger than that of Si which is $|\Delta l_{Si}|$ ≈ 0.2 nm (124). in Fig. 4.3a). By contrast, the resonance

frequency is weakly sensitive to the voltage applied on the gate, as it will be explained further in the text.

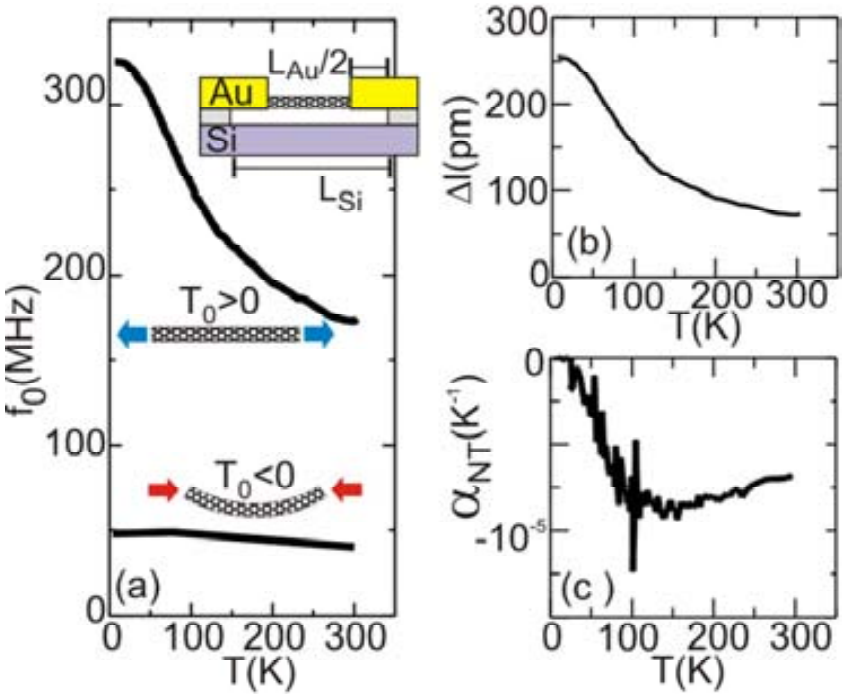

Fig. 4. 3. (a) Resonance frequency as a function of T for a 640 nm long nanotube (upper curve, the built-in tension T_0 is positive). For comparison, the lower curve corresponds to the measurement of the lowest resonance of a nanotube with slack (T_0<0) whose length is about 1 µm. The upper inset shows the schematic of the nanotube resonator. (b) Elongation imposed on the nanotube under tensile stress, obtained using L_{Au} = 520nm and L_{Si} = 1160 nm (L_{Au} is taken as twice the etched oxide depth measured with AFM). (c) Thermal expansion coefficient of the nanotube in (b).

From the T dependence of f_0, we evaluate the elongation Δl imposed on the nanotube using the relation:

$$f_0 = 0.5\sqrt{T_0/mL_{NT}} \qquad (4.1)$$

valid for a beam under tensile stress and using Hooke's law for a hollow cylinder $\Delta l = T_0 L_{NT}/E\pi(r^2 - (r - 0.167\ nm)^2)$ with built-in tension T_0. Here m = 2.6 ag is the mass of the nanotube, L_{NT} = 640 nm its length, r = 0.85 nm its radius, and E = 1.25 TPa its Young's modulus (L_{NT} and r were measured with AFM before the nanotube suspension). Figure 4.3b shows that the elongation and its variation with T are very small (of the order of 100 pm).

We are now in a position to estimate the thermal expansion coefficient (TEC) of an individual nanotube, a property that has not been measured thus far. For this, we use the definition of the TEC

$$\alpha_{NT} = \frac{\Delta l_{NT}}{\Delta T}\frac{1}{L_{NT}} \qquad (4.2)$$

together with the hypothesis of the conservation of length $\Delta l_{NT} = \Delta l_{Si} - \Delta l_{Au} - \Delta l$. Figure 4.3c shows that the TEC of the nanotube is negative and that its magnitude is rather large (10^{-6} – 10^{-5}

1/K). We obtain similar results for the other nanotubes (for which f_0 could be measured from 300 to 4 K). Interestingly, this TEC is similar to what was recently measured in graphene (125, 126) and also to the TEC estimated using numerical simulations on unclamped nanotubes (127).

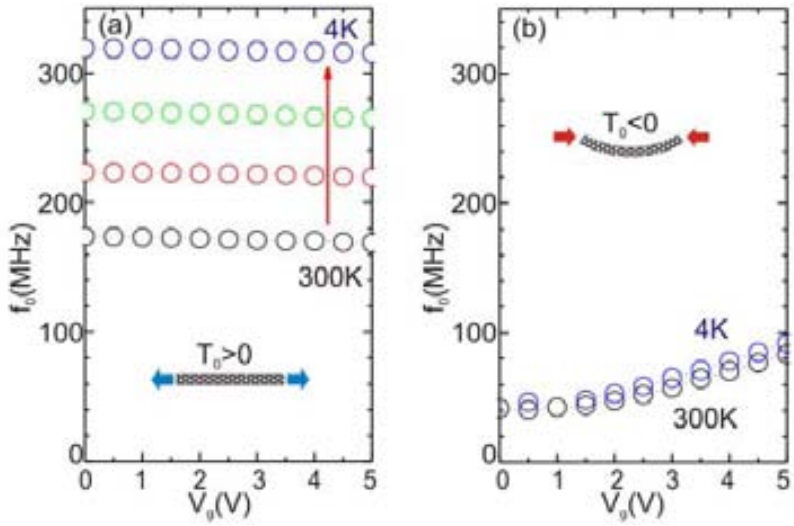

Fig. 4.5. (a) Resonance frequency of a nanotube under tensile stress as a function of V_g for various T (4, 91, 153, and 300K). (b) Same measurement as in (a) for a nanotube with slack. We present only the data of the lowest measured resonance. The nanotubes in (a) and (b) are the same as those in Fig. 4.3a.

Figure 4.5 shows the resonance frequency as a function of V_g (applied on the backgate) at different temperatures and for a device fabricated with the process described in *Appendix A* and having contact electrodes separated by ~640 nm. The resonance frequency is weakly sensitive to V_g. This V_g dependence of f_0 differs greatly from what is measured in nanotube resonators with slack, where $\delta f_0/f_0$ is much larger and positive (Fig. 4.5 b). The latter behavior is well-documented and is attributed to the tension T_e that builds in the nanotube as it bends towards the backgate upon increasing V_g (85) (121) (103). The fact that this behavior is not observed in the resonators fabricated with the process described in this chapter (Fig. 4.5a) is an indication that the nanotube is under tensile stress and that the built-in tension T_0 is much larger than T_e ($T_0 >> T_e$ since $f_0 \sim \sqrt{T_0 + T_e}$ for a beam under tensile stress and that f_0 is not affected by the tension induced by the electrostatic force).

Finally, we discuss mass sensing with ultra-high frequency resonators. Mechanical resonators are widely used as inertial balances to detect small quantities of adsorbed mass through the shifts in resonance frequency. Among the other, the sensors are based on crystals (128, 129), thin films (130) and currently, also MEMS, which can reach mass resolution of down to 7zg (93). With scaling down the devices to nano scale one can expect even better properties, due to their extremely low mass and high Q. Mass resolution in order of zg (1zg = 10^{-21}g) have been achieved (94, 96), opening many fascinating possibilities, such as direct measurements of mass of individual molecules (131).

Such sensitivity also enables the observation of minute mass fluctuations that arise from the adsorption and desorption of atomic species upon the surfaces of NEMS devices (132, 133).

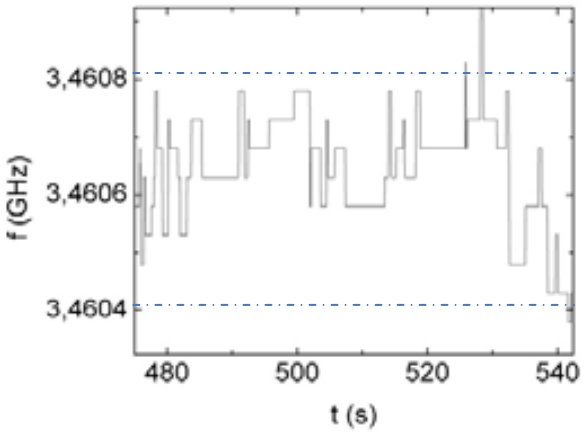

Fig. 4.6. Mass Resolution. Frequency of the first eigenmode measured as a function of time.

Even though the measurement techniques are challenging, the principles of mass sensing is rather simple. CNT resonator can be described by harmonic oscillator with an effective mass m_{eff}, spring constant k and resonance frequency:

$$f_0 = \frac{1}{2\pi}\left(\frac{k}{m_{eff}}\right)^{1/2} \qquad (4.3)$$

Mass sensing consists of monitoring shifts of resonance frequency (df_0) induced by the change of mass of the resonator due to adsorption of atomic species. The shift in frequency df_0 is related to deposited mass dm by (131):

$$dm = \frac{2m_{eff}}{f_0} df_0 \qquad (4.4)$$

Mass responsivity R is an important parameter to evaluate the performance of resonator for mass sensing. High R allows better sensitivity (94):

$$R = \frac{f_0}{2m_{eff}} \qquad (4.5)$$

We analyze mass sensing with a resonator of length *l* = 100 nm, diameter *d* = 4nm and resonance frequency measured at 3.4 GHz. The evolution of the resonance frequency as a function of time is shown in Fig. 4.6.

For the first eigenmode $m_{eff} = 0.7m_{CNT}$, where m_{CNT} is the mass of the CNT resonator. For m_{CNT} = $1200 \cdot 10^{-24}$ kg and f_0 = 3.4606 GHz we obtain $R \approx 2$ kHz/yg (yg=10^{-24}g).

To calculate mass resolution of the device one has to measure the fluctuations of the resonance frequency. The standard deviation is given by $\sigma f_0 = \langle (f_0 - \langle f_0 \rangle)^2 \rangle^{1/2}$. For the values from the Fig. 4.6. σf_0 is 0.2 MHz. Using the value of R calculated before we obtain mass resolution of 100 yg, which corresponds to the mass of 60 protons.

Also experiments with mass sensing were performed with this device. Xe atoms were sent on the CNT resonator at actuated at the resonance frequency; however the signal was lost very quickly. Nevertheless, the high mass sensitivity and stable signal suggest that ultra-short CNT resonators are very promising for mass sensing applications.

4.4 Conclusions

In conclusion, we have reported on a simple method to fabricate high-frequency nanotube resonators under tensile stress. The tensile stress increases upon lowering temperature, since the suspended Au electrodes contract. High frequency resonators made from nanotubes hold promise for various scientific and technological applications, such as mass sensing and experiments in the quantum limit. Also our device layout allows us to estimate the TEC of an individual nanotube. In future high-speed, high-density nanotube circuits, a knowledge of the nanotube TEC will help address thermal management issues.

Finally, we have shown that high-frequency resonators can be very useful for mass sensing applications. Due to their low mass and GHz operation frequency they offer very high responsitivity and mass sensitivity in order of yg.

5. Multi-walled Carbon Nanotube Resonators

5.1 Introduction

Carbon nanotube mechanical resonators have attracted much attention for a number of potential applications. Due to their low mass they are ideal for ultra-low mass and force detection (93-96) and (92, 116, 117). Nanotubes are also exceptionally stiff, which results in high resonance frequency and makes them good candidates for the central vibrating element for NEMS working in MHz and GHz frequencies (84). From the scientific point of view high-frequency devices are interesting for experiments that manipulate and entangle mechanical quantum states (42, 78, 134, 135).

In the recent past main focus was placed on investigating SWNT resonators due to their excellent properties, such as high Q factor, low mass and high mass sensing resolution. On the contrary, MWNT resonators have never received that much attention. The main advantage of MWNT resonators is that they enable us to study systems with different diameters and mass. Using electrical breakdown technique it is also possible to study change of resonance frequency as a function of number of shells. As mentioned before, nanotube resonators could be useful for mass-sensing applications; therefore it is interesting to verify if MWNT resonators can also serve for this purpose.

Various approaches to detection of vibrational motion of nanotubes have been reported so far. Detection of vibrations of MWNT resonators has been achieved with transmission or scanning electron microscopy (136-139) and field-emission (140). Bending-mode vibrations with frequencies up to 3.1 GHz of carbon nanotube resonators were also mechanically detected by means of scanning force microscopy (73). Up to now no measurements of MWNT resonators were reported using mixing technique. This method, successfully employed to measure vibrations of SWNT resonators, is especially interesting because it allows all electrical actuation and readout, and makes possible integration with current electronic systems (84, 92).

5.2 Fabrication and measurements

The nanotube resonator used in these experiments is shown in Fig. 5.1. The resonator consists of a MWNT synthesized by arc-discharge evaporation. The nanotube is connected to two Cr/Au electrodes patterned by electron-beam lithography and metal evaporation on a highly-conductive Si substrate, with a 1 µm thermal silicon dioxide layer. The nanotube is released from the substrate during a buffered HF etching step. All the details about fabrication can be found in *Annex A*.

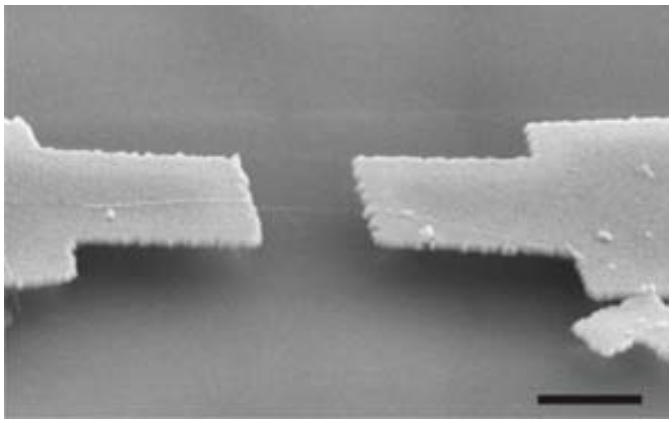

Fig. 5.1. Suspended MWNT resonator. The AC voltage (V_{FM}) is applied to the source and the constant voltage V_g is applied to back-gate to induce the tension. Scale bar: 1 µm.

The suspended samples were then introduced in the ultra-high vacuum system (UHV) and cooled down to temperature of approximately 4K. The motion was driven and detected using the frequency modulation (FM) mixing technique (see *Annex B* for details). The metallic contacts served as source and drain and gate voltage V_g was applied directly to highly-conductive substrate.

5.3 Discussion

First of the measured devices had length L= 1.2 µm, r = 9 nm and room temperature contact resistance of R = 34 kΩ. At 4K the nanotube behaved as a p-doped semiconductor, conductance as a function of gate voltage V_g is shown in Fig. 5.2a. We measured four eigenmodes at frequencies of 110, 283, 580 and 1038 MHz (Fig 5.2b).

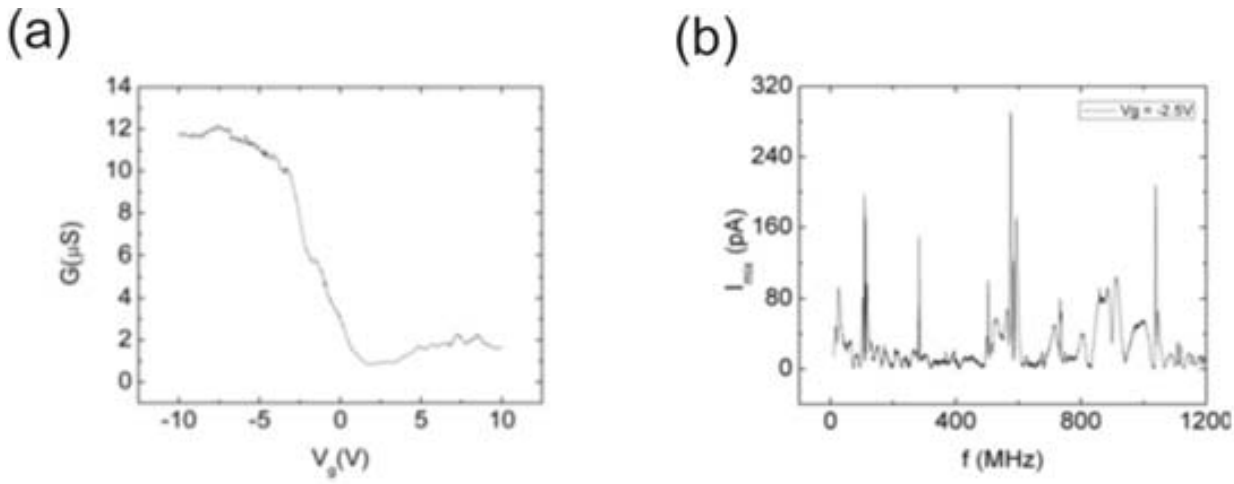

Fig. 5.2. (a) Conductance of MWNT resonator as a function of gate voltage at 4K (b) Resonance peaks at 110, 283, 580 and 1038 MHz; measurements at 4K, V_g = -2.5 V and V_{FM}=80mV.

According to Garcia-Sanchez *et al.* resonance frequencies can be calculated using the elastic beam theory (73). The first eigenmode is given by:

$$f_n = \frac{\beta_n^2}{4\pi}\frac{r}{L^2}\sqrt{\frac{E}{\rho}} \qquad (5.1)$$

Where β_1^2 = 22.37, ρ = 2200 kg/m^3 (density of graphite), E the Young modulus, r and L nanotube's radius and length, respectively. We assume the value of E to be 0.3 TPa, as it was done previously in ref. (73). From equation (5.1) the first eigenmode of the resonator should have the frequency of 129 MHz, which is in agreement with measured frequency of 110 MHz. The relations between higher modes and the first one (f_n/f_1) are also given by the elastic beam theory. Experimental and calculated values of resonance frequencies are shown in Table 5. 1 and details of elastic beam theory can be found in *Annex C*.

Eigenmode	*Measured frequency*	*Calculated frequency*	*f_n/f_1 measured*	*f_n/f_1 theoretical*	*Q factor*
f_1	110 MHz	129 MHz			55
f_2	283 MHz	303 MHz	2.57	2.76	100
f_3	580 MHz	595 MHz	5.27	5.41	52
f_4	1,038 GHz	979 MHz	9.43	8.90	148

Table 5.1. Measured and calculated resonance frequencies of MWNT resonator.

Experimental and theoretical values are in good agreement, confirming that indeed elastic beam theory is suitable for MWNT resonators. The possibility of fabricating nanotube devices with pre-determined frequencies and all-electric actuation and readout is very promising for future applications, for instance in telecommunication industry. The resonance frequency shows no dependence on V_g, which suggests that the tube is under very high tension (88). This can be an advantage, since the device persists at fixed frequency, while gate voltage can be tuned to obtain the best signal.

The biggest disadvantage of the device is the low quality factor. The Q factor oscillates between 50 and 150, for comparison, for SWNT resonators at similar conditions it can reach up to 120 000 (86). Low Q factor is a big drawback for mass and force sensing. However, with the recent work on non-linear damping it may be possible to increase the Q factor by optimizing either device parameters or actuating AC voltage (92).

For the second device we investigated how the conductance and resonance frequency of the device changes while reducing the number of shells using the electrical breakdown technique (*Annex A*).

Before applying breakdown technique the device had L = 1.2 µm and r = 15nm. In Fig. 5.3b the evolution of conductance of the device as a function of V_g is shown for different number of shells removed (Fig. 5.3a). The black curve shows the conductance of the nanotube before applying the electrical breakdown. With removing shells the conductance decreased and also changed the shape; in red and green curves we observe almost no slope: the tube changed from semiconducting to metallic. This transition between semiconducting and metallic properties was observed before and can be explained by the fact that only one or two outer shells contribute to the conductance, depending on whether they are semiconducting or metallic the curve can have different shape (141).

In the lowest, blue curve of Fig. 5.3c we observed the onset of Coulomb peaks. This is when approximately only three shells are left from the device. This is a proof that with burning of the shells we can reduce the size of the device in a way that it changes from field effect transistor (FET) to single-electron transistor (SET).

At low temperatures the nanotube can exhibit single-electron tunneling behavior. This is due to the fact that the metal/carbon nanotube contacts form tunnel barriers with small (<1 fF) junction capacitances. This effect was first observed by Bockrath *et al.* (142) in ropes of carbon nanotubes and later in individual CNTs by Tans *et al.* (143). The CNT-based SETs have been considered particularly interesting, because of their relatively high charging energy E_C (typically, E_C>2 meV) and operation on temperatures of ∼4 K.

SETs consist of a conducting island connected by tunnel barriers to two metallic leads. For temperatures and bias voltages that are low relative to a characteristic energy required to add an electron to the island, electrical transport through the device is blocked. Conduction can be restored, however, by tuning a voltage on a close-by gate.

In the second part of the experiment we measured how mechanical vibrations changed with reducing the number of shells of the tube. For this device only one eigenmode was measured at 240 MHz when no shells had been removed (Fig. 5.4a). For four and three more shells removed we did not observe any peak corresponding to mechanical resonance. This may be due to very low value of dG/dV_g for red and green conductance curves, which causes I_{mix} too low to detect (see *Annex B*). After removing total of 11 shells we measured a resonance peak at 282 MHz (Fig. 5.4b). The frequency increased because while burning shells we decreased the mass of the device. Therefore burning shells of MWNT resonator can be an effective way of tuning its frequency. Removing 11 shells changed the frequency by 42 MHz, which gives 3.8 MHz/shell.

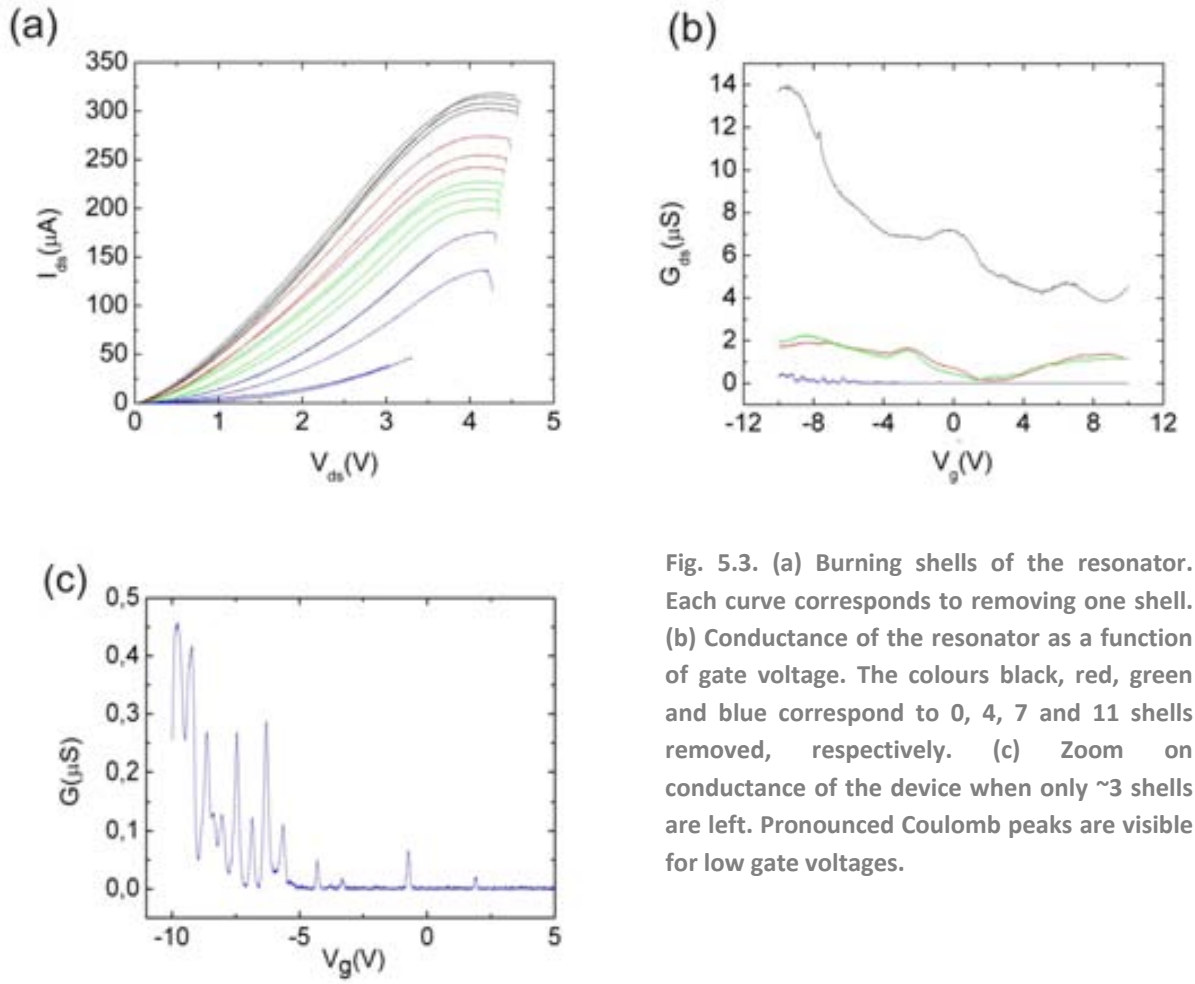

Fig. 5.3. (a) Burning shells of the resonator. Each curve corresponds to removing one shell. (b) Conductance of the resonator as a function of gate voltage. The colours black, red, green and blue correspond to 0, 4, 7 and 11 shells removed, respectively. (c) Zoom on conductance of the device when only ~3 shells are left. Pronounced Coulomb peaks are visible for low gate voltages.

Both of the peaks show dependence on V_g which is a proof that they are mechanical resonances and that the device has a slack, i.e. the length of the suspended nanotube is bigger than the length of the trench (85, 88). The Q factor of the resonator is 250, which is more than twice as good as for the previous device.

We can calculate the change in mass of the tube:

$$\frac{dm}{m} = 2\frac{df}{f} \quad (5.2)$$

Where $\frac{dm}{m}$ is a relative change of mass of the nanotube, df is the change of frequency and f is the frequency of the device. From the equation (5.2) we calculated that after removing 11 shells mass of the device decreased by 35%.

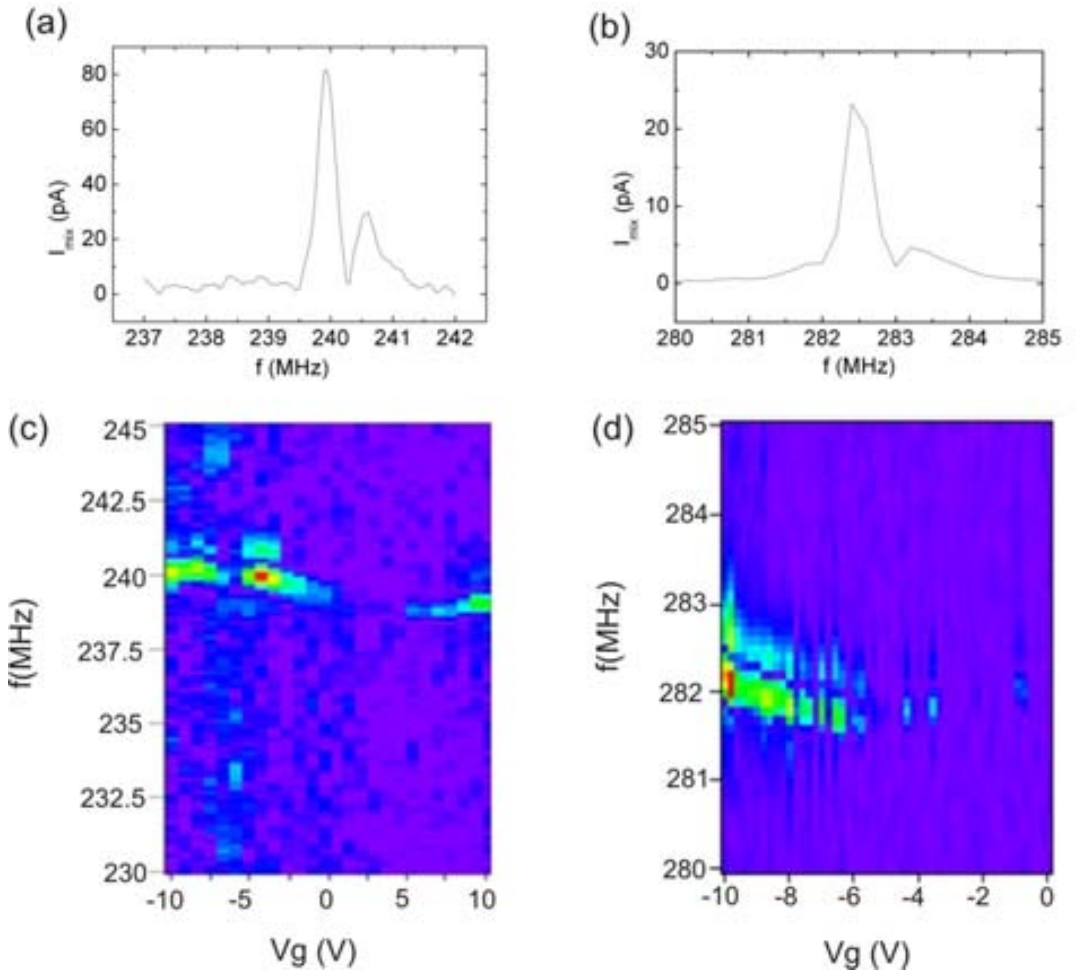

Fig. 5.4. (a) Resonance frequency before the applying the electrical breakdown technique; V_g = -5V, V_{FM} = 50 mV. (b) Resonance frequency after removing 11 shells; V_g = -9.3V, V_{FM} = 50mV. (c) and (d) Frequency as a funtion of gate voltage for 240 and 282MHz resonance, respectively.

5.4 Conclusions

To conclude, we have reported frequency mixing measurements of MWNT resonators. The main advantage is the possibility of fabricating electromechanical components with pre-determined frequencies. The frequency can be further tuned by burning the outer shells or changing (nanotube under tension) or changing the gate voltage (nanotube with slack). The electrical actuation and readout make them good candidates for applications in electronic industry for radio-frequency telecommunication devices. In limited range it is possible to perform mass sensing with the resonators.

6. Micro-fabricated heaters for controlled thermal gradient CNT motor

In collaboration with Neus Sabate and Marc Salleras (Centro Nacional de Microelectronica, Barcelona).

6.1 Introduction

Thermal gradient motor is a novel type of nanoscale device with unique properties reported first by Barreiro *et al*. (114). In the presence of a large thermal gradient (~1K/nm) along the nanotube, there is a net current of phononic excitations moving from the hot spot toward the cooler regions. If a cargo is attached to a movable part of an engineered MWNT phonons can interact with it and transfer momentum. As a consequence, the cargo moves from the hot spot towards the cold.

The biggest disadvantage of the motors reported so far is the lack of control of the direction of motion, i.e. it occurs always from the middle of the CNT towards one of the contacts. In order to control the motion we propose a device layout in which the CNT motor is suspended between two heaters, as shown in Fig. 6.1. By changing the temperature at the ends of the motor the cargo can be moved back and forth. In this experiment the challenge is to integrate the device with a micro-scale heater, which can reach very high temperature (~1300K). To fabricate a complete device a top-down technique typical for MEMS has to be combined with the bottom-up approach used for nanotube devices.

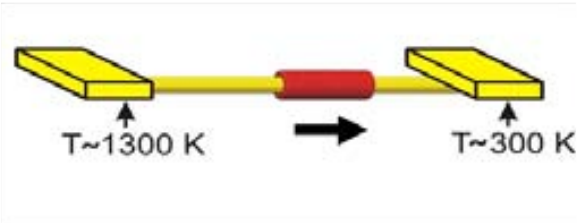

Fig. 6.1. Controlled thermal gradient motor. The arrow points the direction of phononic current along the nanotube (yellow) which induces the motion of the cargo (red).

Since the 90s the interest in MEMS micro-heaters has increased rapidly, as they have become key components in various types of sensors, such as wind sensors (144), humidity sensors (145) and gas sensors (146, 147). A MEMS micro-heater that emits heat by applying a current to a resistor (Joule heating) has the advantage of low power driving as well as a very short response time. In particular, micro-heaters are becoming increasingly important in portable electronics applications where low-voltage and low-power designs are required. Several investigations have been conducted on micro-heaters that use SiC (148), platinum (149-152), poly-silicon and single crystal silicon (153), TiN (154) and tungsten (155-159) as the heating layer. Various studies of temperature distribution uniformity over the heating plate through control of the heat distribution were previously conducted (160).

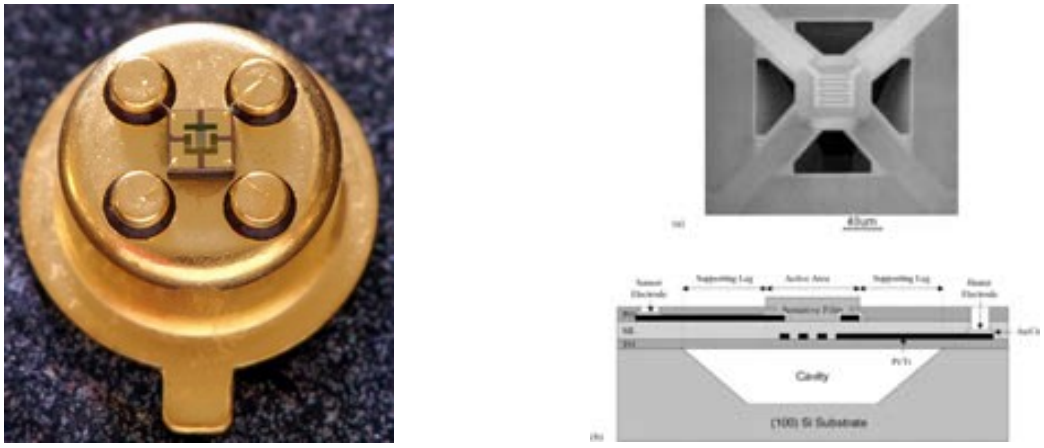

Fig. 6.2. (a) Commercially available MEMS Micro Hot Plates chemical sensor applications (161)**. (b) Structure of a micro-machined gas sensor element (a) front view; (b) cross-sectional view** (162)**.**

Recently, also commercially available micro-hotplates, for example Kebaili Corporation KMHP-100 (Fig. 6.2a), have appeared on the market. They can be used for instance in medical, industrial, military, automotive, environmental, agricultural, space and homeland security applications.

We are in interested in fabricating a micro-heater which will allow us to induce a controlled temperature gradient along the nanotube and induce motion of a nanotube thermal motor. The heater should have following properties:

(1) High temperature operation (up to 1200˚C);
(2) Fabrication process compatible with CNT (this excludes for example sputtering or dry etching);
(3) Possibility of fabricating a CNT motor suspended between two heaters (this excludes large micro-hotplates, since the temperature is maximum in the middle of the heater).

On the contrary, we are not interested in the properties important for the industry, such as uniform temperature distribution or low power consumption. To our knowledge, no heaters reported in literature so far are fulfilling those requirements; therefore we need to design our own devices. For that purpose we have developed two types of heaters: metal (platinum and gold) heater and silicon heater.

6.2 Platinum and gold based micro-heaters

6.2.1 Design, simulations and optimum geometry

One approach to fabricating micro-heaters is to use Joule heating of a thin metal layer, for example platinum or tungsten. The biggest advantage of those heaters is high temperature operation (up to 700˚C), limited only by materials melting point and thermo- and electromigration (158, 163). The temperature can be easily controlled by monitoring change in the heater resistance

In various works platinum was used as a resistive heater for micro hot plates (155-157, 164), due to its high melting point and compatibility with CMOS technology. As an industry standard, a Pt resistance temperature detector (RTD) has the best stability and repeatability, and it offers virtually linear temperature-resistance response over the temperature range from -50°C to 550°C. In this experiment, we used the Pt heater as a self-sensing resistive temperature meter to determine its average temperature variation (165).

One of the important issues is the isolation of the metal layer from the substrate, which typically acts as a heat sink. Usually, in micro-hotplates the metal resistive heater is sandwiched between freestanding thin-films of, for example, silicon nitride or silicon dioxide (161). The freestanding membranes thermally and electrically isolate the metal micro-heater from the silicon substrate, and provide the micro-hotplate with a low thermal mass. This approach, however, cannot be applied to a CNT motor, due to large membrane size (tens to hundreds of microns) and incompatible fabrication methods (dry etching and sputtering).

For this reason we designed a device layout in which a thin metal layer is deposited on top of a suspended silicon bridge (Fig. 6.3). Metal thin film serves as a heater and the air gap between Si bridge and sample surface provides good thermal isolation. The Si layer has to be non-conductive, so that the Joule heating comes only from the metal. It should be possible to suspend a nanotube between two heaters and by heating one side at a time control the movement of the cargo deposited on the motor.

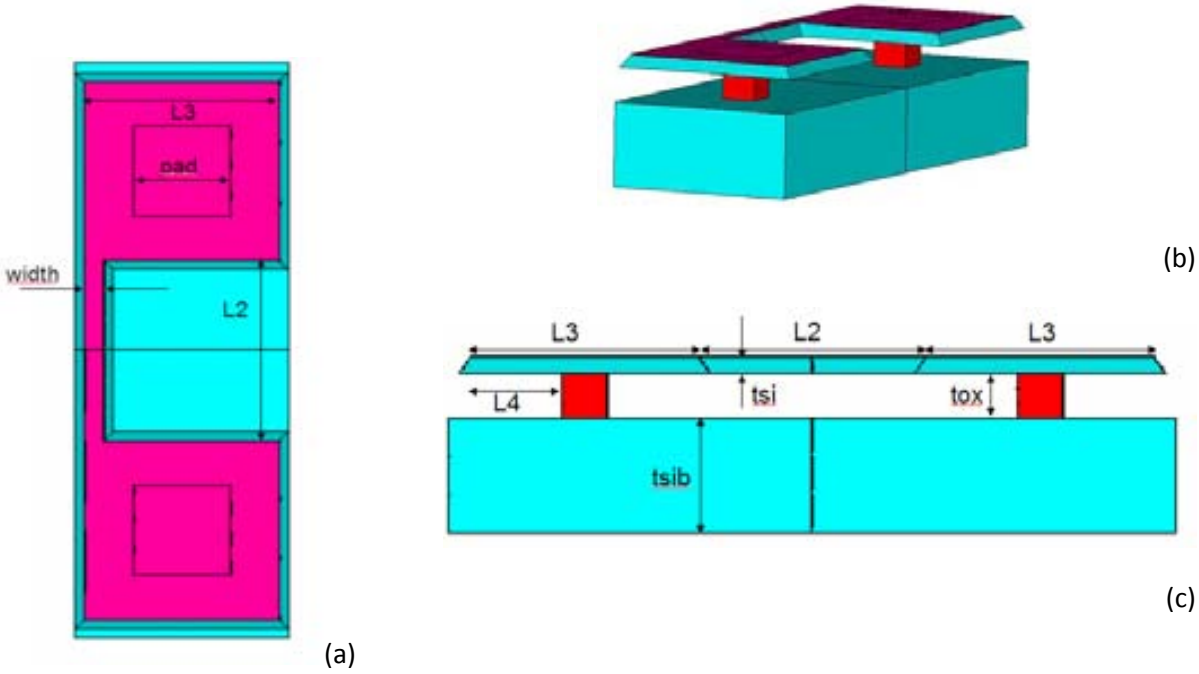

Fig. 6.3. (a), (b) and (c) Geometry of the model. Blue, red and pink correspond to silicon, silicon oxide and platinum, respectively).

Parameter	*Value*
width	**1µm**
L2	**10µm**
L3	**10µm**
pad	**5µm**
L4	**4µm**
tpt	**50nm**
tsi	**0.7µm**
tox	**2µm**
tsib	**5µm**

Table 6.1. Default values of the parameters used in calculations.

Simulations of the structure were performed in ANSYS by Marc Salleras from CNM-IMB in Barcelona. Various geometries were analysed in order to optimize the maximum temperature and deflection of the beam and default parameters are shown in Table 6.1. The platinum resistivity ρ used in the model is temperature dependent according to:

$$\rho = \rho_0 \cdot \left(1 + \alpha\left(T - T_0\right)\right) \tag{6.1}$$

Where: T_0 = 300 K, ρ_0 = 212 nΩ·m, and α = 1850 · 10^{-6} K^{-1}.

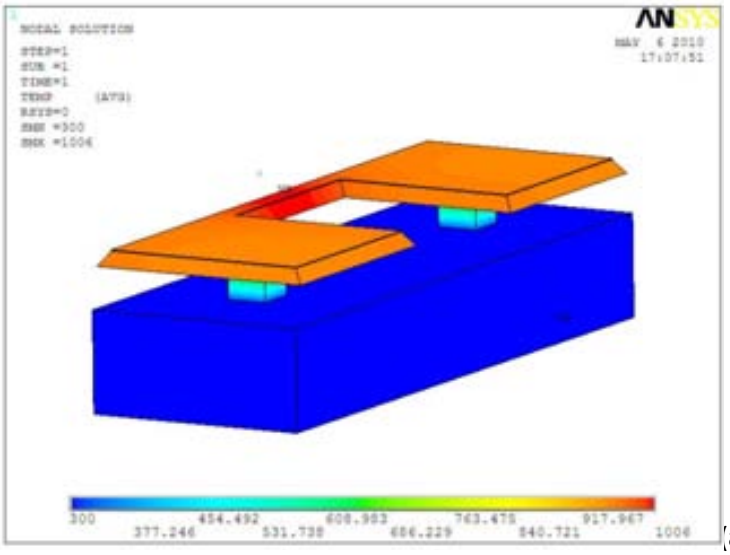

(a)

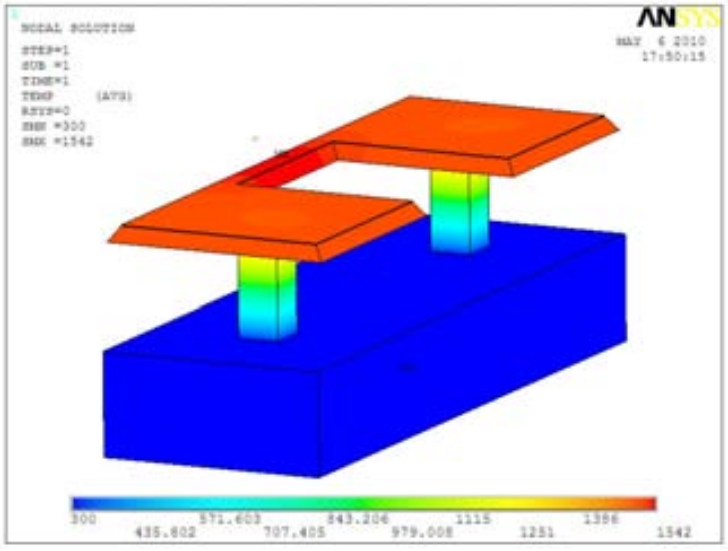

(b)

Fig.6.4. Temperatures obtained for a voltage difference between pads of 0.5V. For SiO_2 thickness of (a) 2 µm and (b) 5 µm, maximum temperature corresponds to approximately 700 and 1200°C, respectively.

The temperature in Fig. 6.4a plot shows that 700°C can be reached with only 500 mV applied between the pads. However, the current density of Φ_I = 1.5·10^{11} A/m^2 exceeds by two orders of

magnitude the maximum current density allowed to neglect electromigration ($\Phi_I = 10^9$ A/m^2). The total power dissipated on a beam of length *L*, width *W* and thickness *D* is given by:

$$P = \Phi_I^2 \cdot W \cdot L \cdot D \cdot \rho \qquad (6.2)$$

Therefore to increase the amount of power generated by Joule effect wider, longer and thicker platinum tracks are needed. However, by increasing track length its deflection during heating is also increased. On the other hand, the major thermal gradient takes place in the silicon oxide layer. To increase the thermal resistance to the heat sink we need thicker oxide layers with smaller cross section.

Using an oxide thickness of 5 µm instead of 2 µm results in maximum temperature of approximately 1200°C for the current density of $\Phi_I = 1.5 \cdot 10^{11}$ A/m^2 (Fig. 6.4b).

6.2.2. Fabrication

To fabricate the heaters we used SOI (silicon on insulator) wafer, with top oxide of 120 nm, highly resistive Si (100) layer of 350 nm and bottom layer of SiO_2 of 1 µm. The wafer was diced in 8x8 mm chips, with the edges along the (100) plane.

The heaters of various lengths (10-100 µm) were fabricated according to the fabrication scheme shown in Fig. 6.5. First of all the heaters were defined by means of e-beam lithography. Then in the openings silicon oxide layer was removed by means of wet etching. The metal layer consisted of 1-20 nm chromium adhesion layer, followed by 75-100 nm Pt layer evaporated directly on the Si. Devices after the lift-off are shown in the Fig. 6.5c.

6.2.3 Etching optimization

The most challenging part of the fabrication was optimization of the etching process in order to obtain suspended devices. During the process top SiO_2 layer of 120 nm, Si layer of 350 nm and bottom SiO_2 layer of 1 µm have to be removed. Various tests were performed to obtain the optimum etching recipe. Below different approaches to wet etching of those materials are discussed.

To remove Si layer either KOH or TMAH (tetramethylammonium hydroxide) can be used. KOH is one of the most commonly used silicon etch for micromachining silicon wafers. It is anisotropic and etching rate is strongly affected by the crystallographic orientation of the silicon. The (110) plane is the fastest etching primary surface. The ideal (110) surface has a more corrugated atomic structure than the (100) and (111) primary surfaces. The (111) plane is an extremely slow etching plane that is tightly packed, has a single dangling-bond per atom, and is overall atomically flat.

(a)

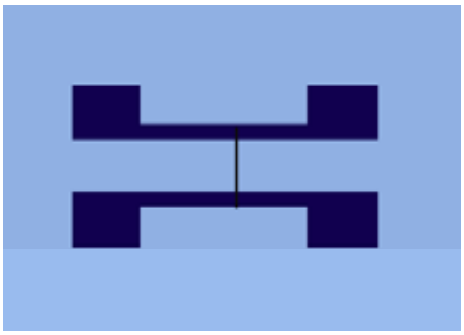

1. Heater structure is defined in PMMA by means of e-beam lithography.

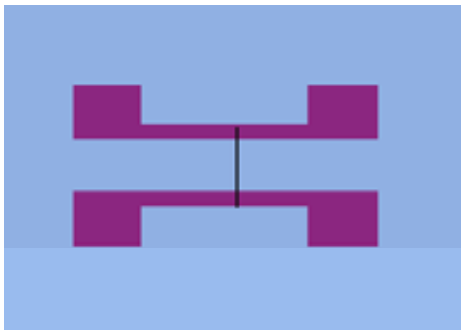

2. The SiO2 is etched in the openings.

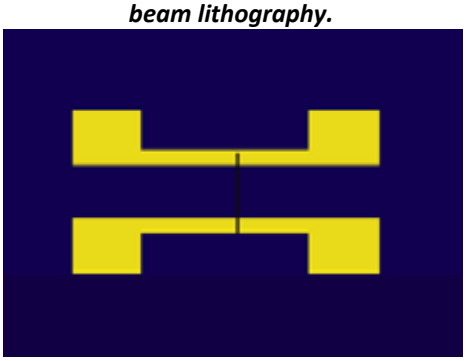

3. Metal evaporation and lift-off

4. Top SiO_2, Si and bottom SiO_2 are etched. The structure is suspended.

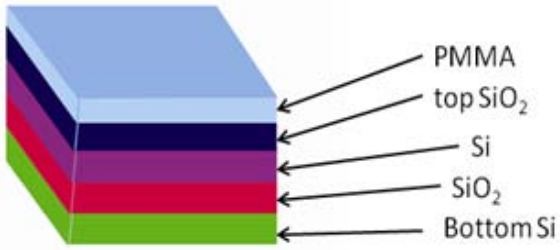

(b)

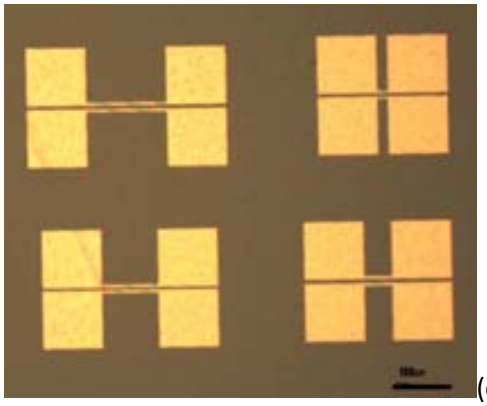

(c)

Fig. 6.5. (a) 1-4: Top view of the fabrication process for Pt (Au) heater. Black line symbolizes a CNT motor. (b) Structure of the SOI wafer coated with PMMA. (c) Optical image of gold heaters of different lengths (150, 100, 50 and 15 µm) before the etching.

The strongly stepped and vicinal surfaces to the primary planes are typically fast etching surfaces. As with all wet-chemical etching solutions, the dissolution rate is a strong function of temperature. Significantly faster etch rates at higher temperatures are typical, but less ideal etch behaviour is also common with more aggressive etch rates. Also, heavy boron doping can significantly harden the silicon and sharply reduce the etch rate (166-167).

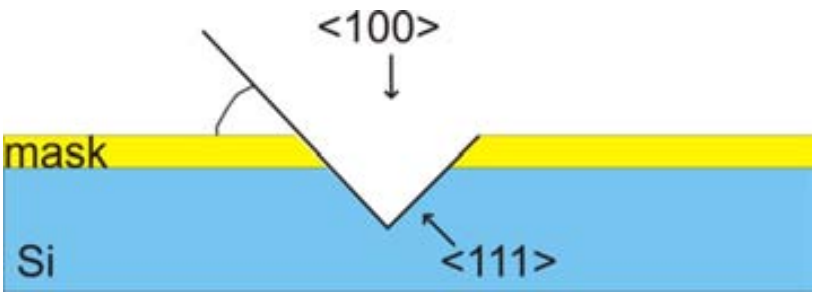

Fig. 6.6. Schematic etching of the silicon (168).

TMAH is similar to KOH etching and it is also commonly used for fast removal and silicon micromachining. The orientation dependence of the TMAH etch rate is similar to KOH and varies similarly in accordance to the atomic organization of the crystallographic plane. The main difference is that it does not affect SiO_2.

	TMAH (25%) (nm/min)	*KOH 40% (nm/min)*	*HF 49% (µm/min)*
Thermal silicon oxide	<0.1	44	1.4
Si (100)	600	600	-----

Table 6.2. Etching rates for TMAH, KOH and HF 49% (courtesy of M. Duch and M. Gerboles from cleanroom of the CNM, Bellaterra, Spain and ref. 169**).**

After various tests we found out that the best was to use KOH 40% in the temperature of 70°C. The etching rate for Si (100) is ~1 µm/min and for SiO_2 ~44 nm/min (Table 6.2). After 2 min in the KOH, both the top SiO_2 and the Si are removed.

The bottom SiO_2 layer has thickness of 1 µm and the heaters have a typical width of 5-10µm. To effectively suspend the heater it is important to use HF of proper concentration. For nanotube applications, such as resonators, we usually used buffered 5% HF with etching rate of approximately 100 nm/min. This concentration is too low to etch under the heater (estimated time 30 min). Therefore we use HF with concentration of 49% and etching rate of 1 µm/min (Table 6.2). The tests confirm that this concentration allows fast etching without destroying the metal layer.

Tests were also performed to find optimum drying procedure. Hot IPA drying is not appropriate and the structures collapse due to surface tension. The best was found to be drying in critical point dryer. After this drying the majority of the structures are suspended.

After imaging various devices after etching it was seen that metal layer is usually not sticking well to the Si surface, as shown in Fig. 6.7a. To improve the adhesion we performed temperature annealing in 300°C in Ar (500 ml/min) and H_2 (100 ml/min) ambient for 30 min before the etching. This visibly improved the adhesion, even though at the edges of the device it was still not perfect (Fig. 6.7b)

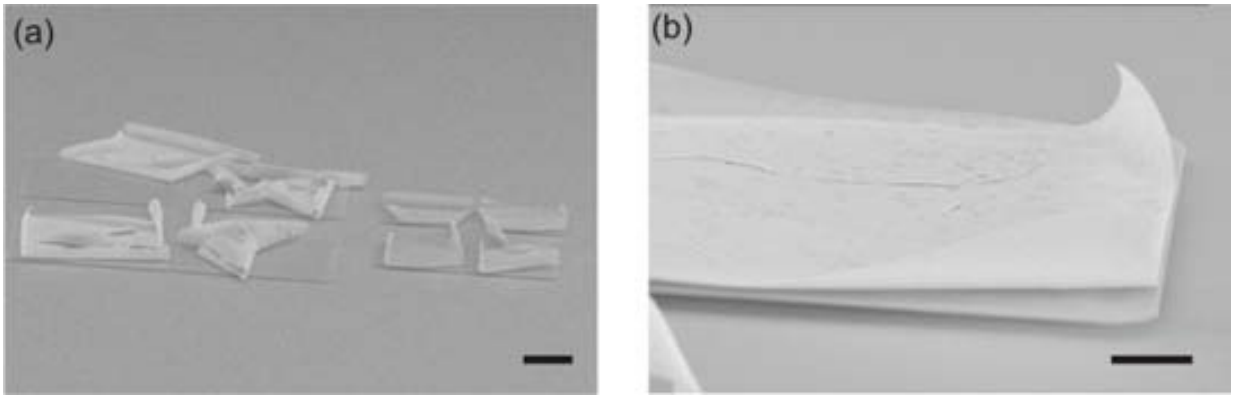

Fig. 6.7. SEM image of platinum micro-heaters with 5 nm Cr and 75 nm Pt after the etching (a) without annealing, scale bar 20µm (b) with annealing. In both cases platinum layer was removed from the surface during the etching process, scale bar 3µm.

6.2.4 Adhesion layer thickness optimization

In order to optimize platinum adhesion, we tried different thickness of chromium as the adhesion layer. We fabricated devices with 0.5, 10 and 20 nm of Cr and 75 nm of Pt (Fig. 6.8) and performed temperature annealing. It did not make a visible change in the devices after the etching. Due to the adhesion problems, it was impossible to fabricate good devices with Pt as a resistive heater.

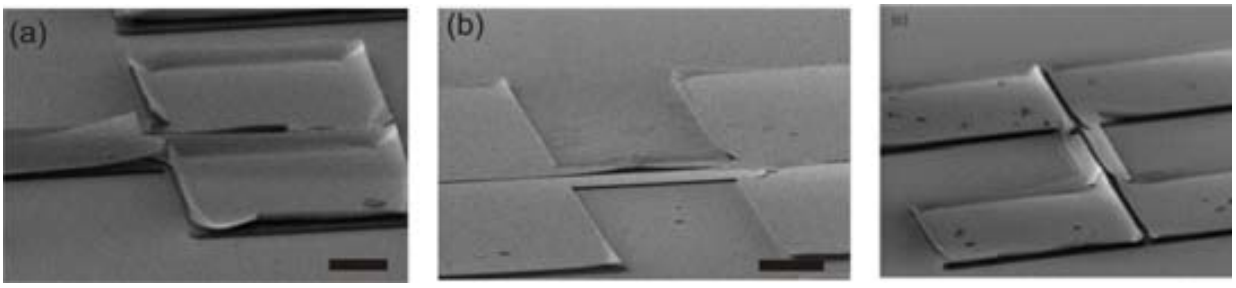

Fig. 6.8. Test etching of platinum heaters with different thickness of adhesion layer. Scale bar 20µm. (a) 0.5nm Cr and 75nm Pt. (b) 10nm Cr and 75nm Pt. (c) 20nm Cr and 75nm Pt.

6.2.5 Heating layer optimization: gold heaters

As next step, we fabricated the same type of heater with gold instead of platinum. Gold has lower melting point (1200°C) and for high current densities in the device electro-migration can be an issue. The big advantage, as it is shown below, is that the adhesion to silicon is much better than for platinum.

The fabrication procedure was the same as for the Pt heater, with the difference of evaporating 5 nm chromium and 75 nm of gold as a top metal layer.

The first etching test was not satisfactory; Fig. 6.9a shows poor adhesion of the metal layer to the Si. To improve adhesion we performed the same high temperature (300°C) annealing in Ar and H_2 atmosphere as for the platinum heaters and also increased thickness of Cr and Au layers to 10 and 100nm, respectively. Those improvements resulted in good adhesion of the metal during the etching, as shown in Fig. 6.9b and 6.9c. So-fabricated heaters were ready for temperature characterization.

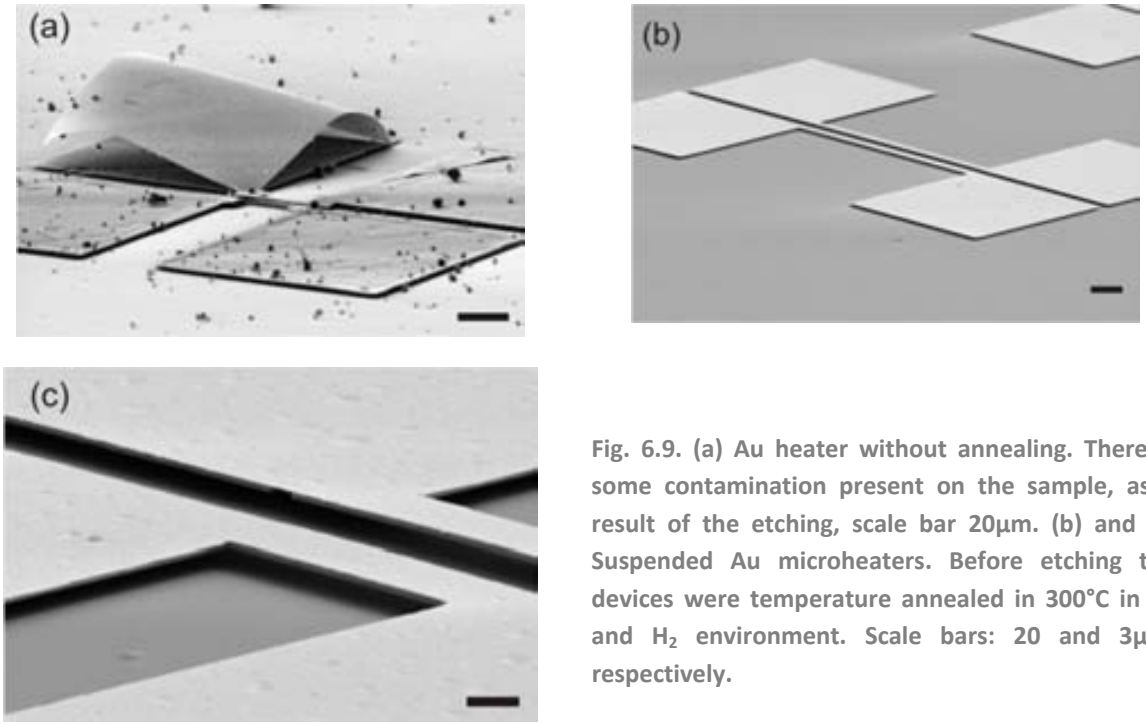

Fig. 6.9. (a) Au heater without annealing. There is some contamination present on the sample, as a result of the etching, scale bar 20µm. (b) and (c) Suspended Au microheaters. Before etching the devices were temperature annealed in 300°C in Ar and H_2 environment. Scale bars: 20 and 3µm, respectively.

6.2.6 Temperature characterization

To extract the temperature of the heaters, we measure the change in device resistance. The resistance dependence on temperature is described by equation (6.1).

First of all, we extracted α coefficient for the Cr/Au layer. The suspended gold heater of l = 20 µm and w = 2 µm was wire-bonded in TO-8 sample holder and characterized in the oven in air. The sample was slowly warmed up to approximately 200°C and then cooled down to room temperature, with the resistance constantly monitored. We used four-point measurements to eliminate the influence of the contacts. Even though to measure the resistance we had to apply small voltage to (-0.01÷0.01 V), it did not influence the heating of the device.

From the measurements we extracted the value of temperature coefficient α of $18 \cdot 10^{-4}$ K^{-1}, which is comparable with the macroscopic value of $20 \cdot 10^{-4}$ K^{-1}.

Next step of heater characterization was performing test heating. For thermal measurements devices were bonded on the printed circuit board with thin Al wires and placed in vacuum chamber with pressure of $3 \cdot 10^{-5}$mbar. Current (I_{in}) was applied to the device in order to induce Joule heating, which was detected by measuring change in resistance. Keithley 2400 multimeter was used as a current source and the voltage drop on the device (V_{out}) was measured with DAC, as shown in the Fig. 6.10a. Resistance of the heater was calculated from:

$$R = \frac{V_{out}}{I_{in}} \qquad (6.3)$$

(a) (b)

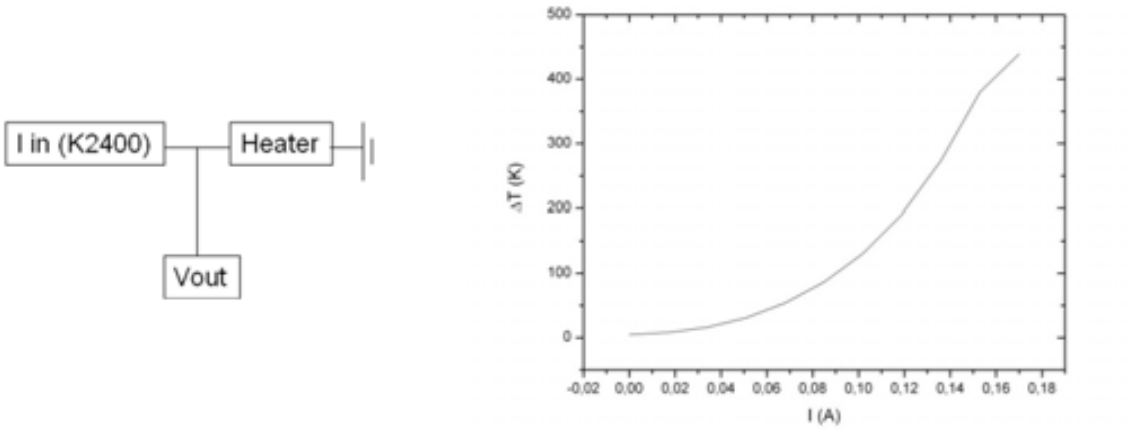

Fig. 6.10. (a) Schematic of measurements (b) Change of the average temperature of the Au heater ΔT as a function of applied current I.

According to eq. 6.1 we can extract the average temperature change of the device ΔT. ΔT is measured with respect to the room temperature. The maximum temperature ΔT = 435°C is obtained for I = 0.18 A (Fig. 6.10b) and the dissipated power P = 486 mW. At this point the device broke.

Assuming parabolic distribution of the temperature on the device we extract the maximum temperature in the middle of the bridge, which is approximately 650°C. This is comparable with the results of previously fabricated heaters (158) and can be enough to drive the CNT thermal motor.

6.2.7 Integration with CNT motor

Final step of the experiment was to integrate the system with the CNT motor. Here the two approaches: top-down approach of fabricating the heater and bottom-up approach of fabricating nano-devices need to be combined to obtain the final device. Fabrication steps were as follows:

1. Deposition of MWNTs on SOI chip with pre-fabricated marks
2. EBL for gold heater and cargo
3. Etching of the top SiO_2 layer
4. Metal evaporation (10 nm Cr/100 nm Au)

5. Lift-off
6. CVD annealing (30 min, 300C, Ar = 500ml/min, H_2 = 100 ml/min)
7. Electrical breakdown of the MWNT with cargo
8. Etching (KOH and HF)
9. Critical point drying

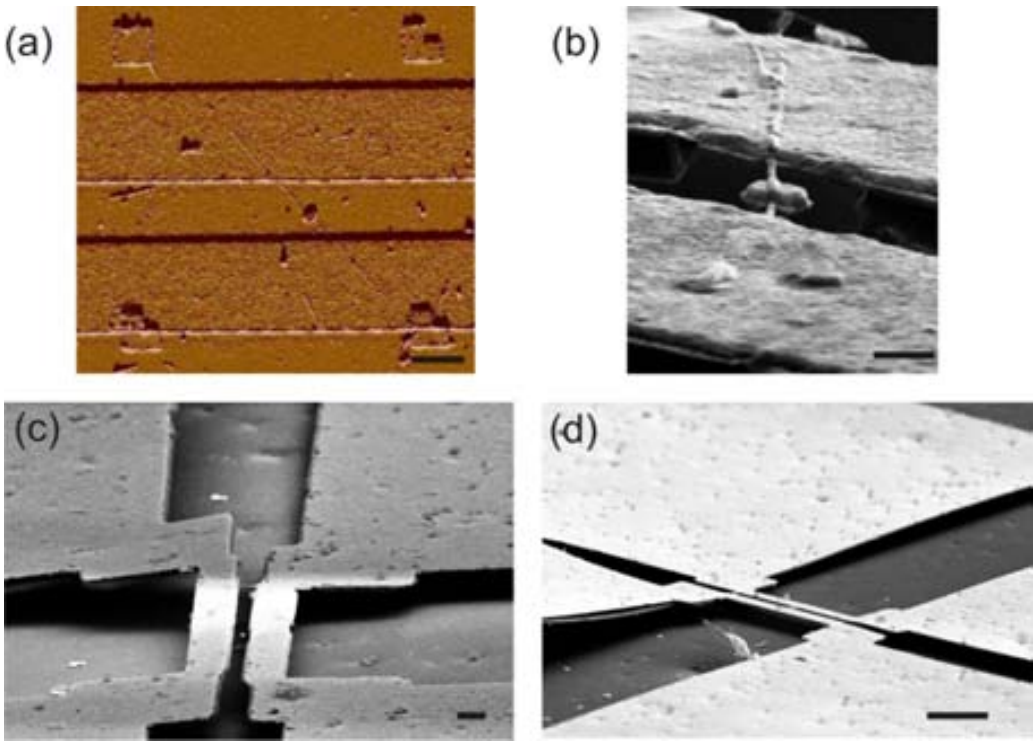

Fig. 6.11. Thermal gradient motor. (a) AFM image of the device before the etching, scale bar 1µm. (b) SEM image of the device after etching, scale bar: 1µm (c) and (d) The heater after etching. Silicon layer is strongly deformed, most probably during the internal stress. Scale bars: 3 and 10µm, respectively.

The advantage of this fabrication scheme is that it requires only 2 EBL steps (alignment marks and contacts) which reduce fabrication time. The disadvantage is that etching with KOH is anisotropic, therefore the heater has to be aligned with respect to the (100) plane of the Si and the MWNT has to be long enough to bridge two heaters (Fig. 6.11a).

Various unexpected problems appeared while integrating the heater with a CNT motor. The main drawback was that after etching we observed large deflection of the Si beam (Fig. 6.11c, d). This destroys the nanotube. This deflection stems from internal stress of the Si layer, which arises during the production of SOI wafers. For micro scale applications this deflection may not be crucial, but the nanotubes are very fragile and even nanometer scale deformation may cause breaking of a suspended CNT.The other disadvantage is underetching under the nanotube, as seen in the Fig. 6.11b, which can also lead to breaking or poor contact resistance. Unfortunately, those effects are impossible to control with wet etching and we conclude that it is impossible to reliably combine the gold heaters with CNT motors.

6.3 Silicon Heaters

6.3.1 Design and simulations

Another type of heater for CNT thermal motor application is based on Joule heating of non-suspended silicon beam. Crystalline silicon and poly-silicon have been used for fabricating micro-heaters for gas sensing and successfully integrated on lab-on-a-chip hybrid MEMS gas chromatograph (170).

Compared to previously reported Si microheaters our design is relatively simple, see for example ref. (171-172). The proposed heater consists of the highly-doped Si beam covered by a layer of a SiO_2. The current is injected into Si beam, which serves as a heater. The oxide layer electrically isolates the CNT from the heater. Top Pt layer has two functions. First of all, it works as a temperature sensor and secondly provides an electrical contact for the nanotube (Fig. 6.12). In the final device a CNT motor was suspended between two heaters, separated by ~1 µm. The main advantage of this type of device is eliminating deformation of the beam during etching of the substrate. Also silicon is supposed to withstand high current densities and reach high temperatures.

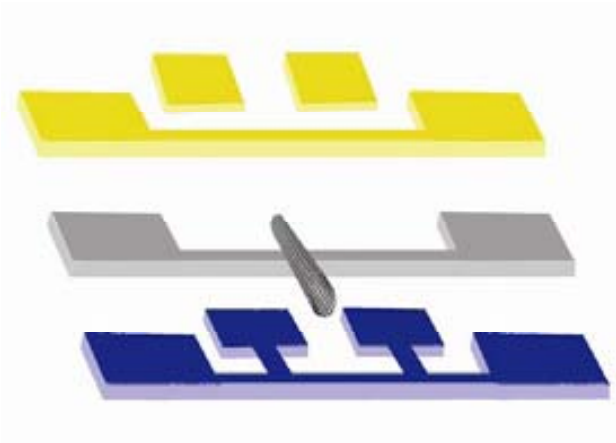

Fig. 6.12. Si heater scheme. Bottom (blue) represents highly doped Si heater, middle (grey) insulating SiO_2 and top Pt (yellow) is a temperature sensor and provides electrical contact for a CNT. On top of SiO_2 a CNT is suspended.

For the device as shown above in fig. 6.12 ANSYS simulations were performed by Marc Salleras in order to optimize beam geometry. First of all, study of the new design, with the silicon beam with oxide below, was performed for variations of the beam length and width. The device geometry and parameters are shown in Fig. 6.13 and Table 6.3. The resistivity value of doped Si $8.87 \cdot 10^{-7} \Omega \cdot m$ corresponds to a doping with phosphorous of concentration $p = 10^{21}\ cm^{-3}$ (173).

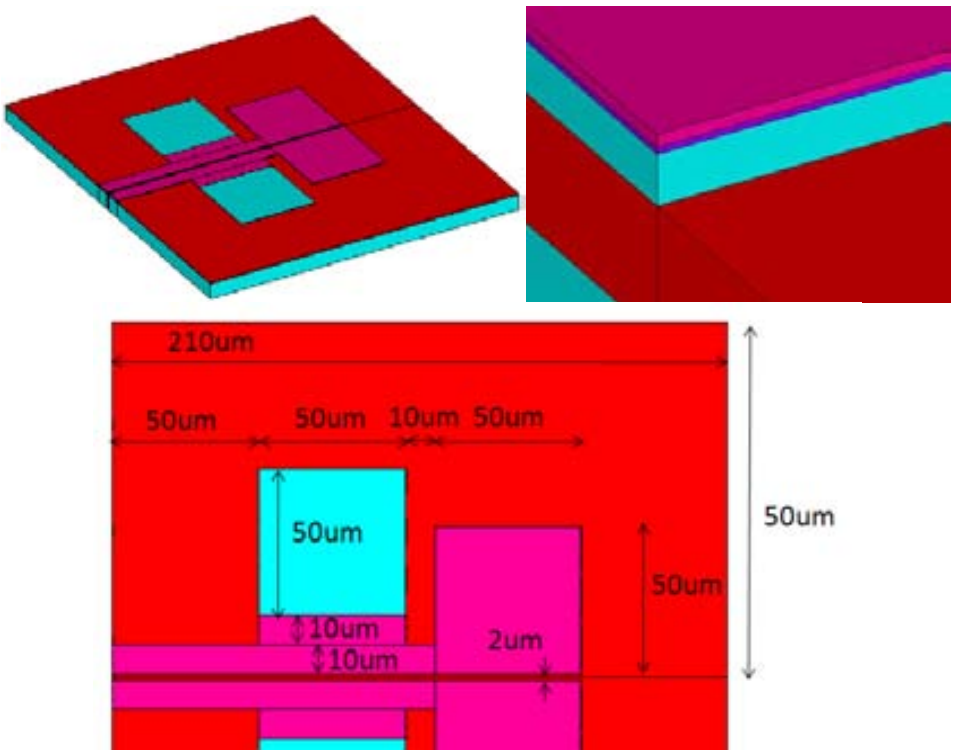

Fig. 6.13. Schematics of the silicon heater. Red corresponds to oxide, light blue is silicon, purple is dielectric and pink is metal.

Material	*Thickness*
Silicon bulk	10 µm
Buried oxide	1 µm
Device layer (Silicon)	350 nm
Dielectric layer (SiO_2)	100 nm
metal layer (Pt)	100 nm

Table 6.3 Fixed parameters for simulations of the beam.

The only two parameters which are varied are the total beam length and the beam width. The total length values used are 100 µm and 200 µm (which correspond to 50 µm and 100 µm in the half model) and default value for the width corresponds to 10 µm. The maximum electrical field between the silicon device layer and the metal layer on top of it, assuming the dielectric layer of 100 nm, the voltage drop of 5 V, and the metal layer fixed at ground, corresponds to $E_{max}= 5 \cdot 10^7$ V/m. The maximum electrical field allowed according to CMOS standards for thermal oxide is 10^9 V/m.

Beam length	*Beam width*	*Maximum temperature*
100 µm	10 µm	460 °C
200µm	10 µm	140 °C
100µm	5 µm	467°C
200µm	5 µm	135°C
50µm	10µm	1357°C

Table 6.4. Maximum temperature of the beam as a function of Si beam length and width.

By optimizing beam geometry high temperatures can be achieved. We showed that increasing the beam length, reduces the maximum temperature (Table 6.4). On the other hand, the beam width is not a significant parameter when trying to increase the maximum temperature with the same voltage. Another analysis was to reduce the length and see how much does the maximum temperature changes. The highest temperature of 1357°C was achieved or a beam of 50 µm length (Fig. 6.15). The results of temperature distribution were simulated for a voltage drop of 5 V.

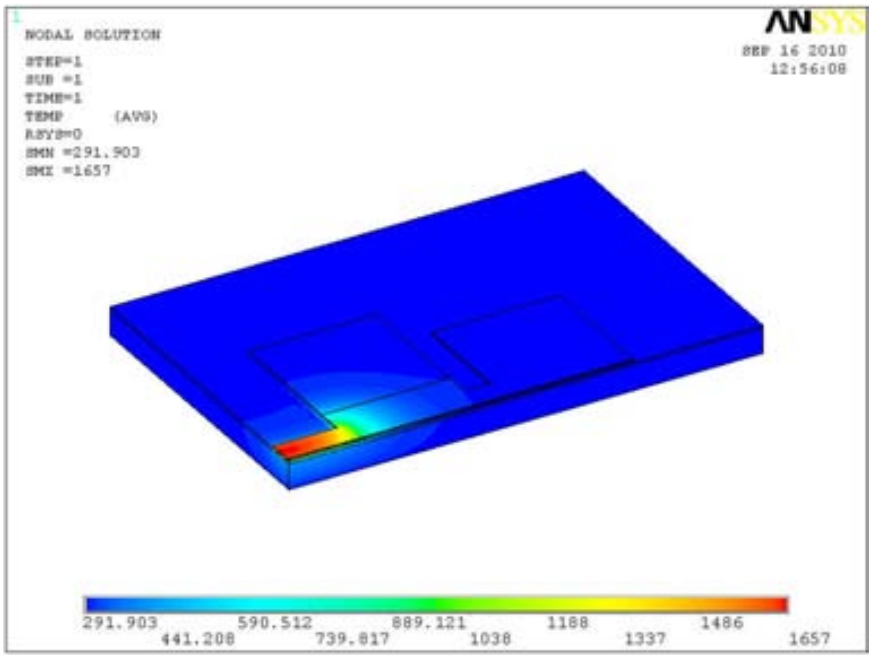

Fig. 6.14. Temperature distribution on silicon device layer (in kelvin). A maximum temperature of 1357°C is achieved with 5 V applied and a current density of $7.6 \cdot 10^{10}$ A/m^2.

6.3.2 Fabrication

To fabricate the heater we used a SOI wafer with 1 µm of bottom SiO_2, 400-1200 nm of highly doped ($p = 10^{21}cm^{-3}$ phosphorus doping) Si with (100) orientation and 320 nm of top SiO_2 layer. As before, the wafer was diced in 8x8 mm chips.

The heater was achieved by means of micro- and nanofabrication compatible with CNTs. The structure was first patterned by means of EBL and metal evaporation, and then the wet etching was performed to obtain the final device.

The fabrication of silicon heater is more challenging than the fabrication of gold heater and consists of three lithography steps. First of all, the contact pads for the heater are deposited directly on silicon. Then the heating/sensing circuit is patterned on SiO_2 and finally they are connected with thin Au layer. This layer serves only as an etching mask and is removed in the end of the process (Fig. 6.16).

During the etching first the SiO_2 layer of 320 nm is removed with buffered hydrofluoric acid 5% for 5 min and then Si is removed with 40% KOH at 70°C for 3 min. In the last step gold layer is removed from the connections between contact pads and platinum tracks (Fig. 6.15 a, b). The heater is finally rinsed in IPA and dried under a gentle flow of N_2 (Fig. 6.15c).

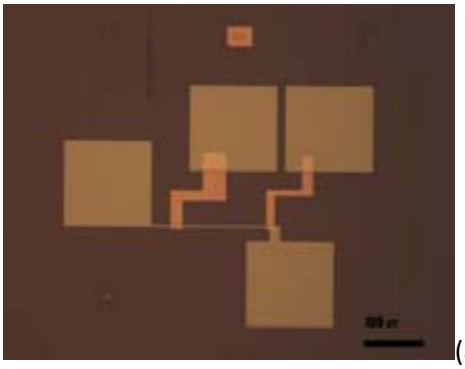
(a)

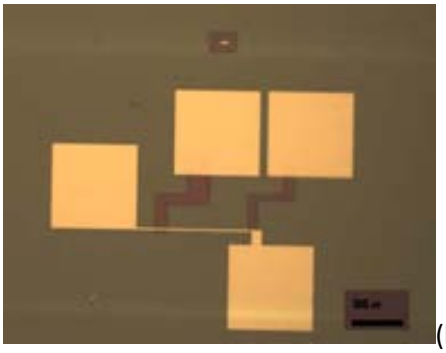
(b)

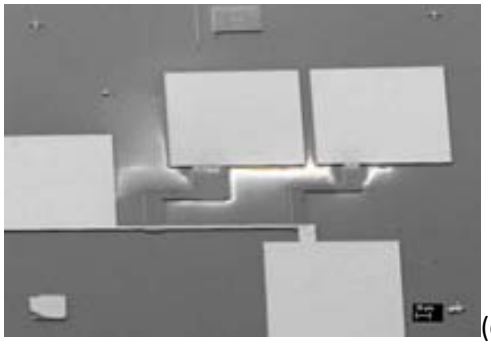
(c)

Fig. 6.15. Optical image of a silicon heater during fabrication. (a) Before the etching. (b) After the etching and removing Au. (c) SEM image of the finished device. Scale bar: 10 µm.

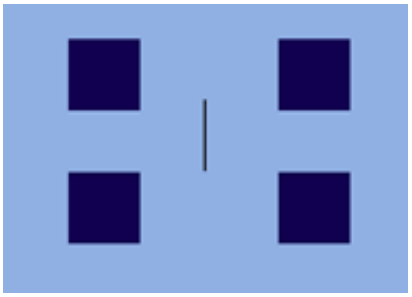

1. Openings for contact pads for silicon heater, made in PMMA by means of e-beam lithography. The black line represents a CNT.

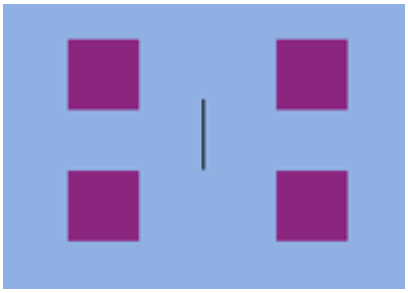

2. Etching of SiO_2 inside the openings

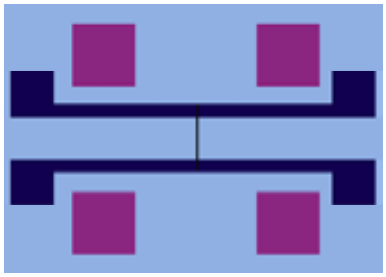

3. Second e-beam lithography to define heater/sensor tracks and sensor contact pads.

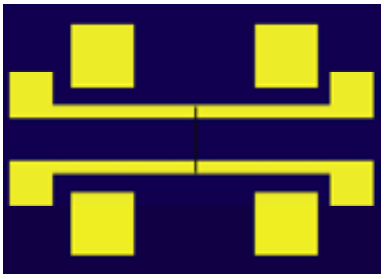

4. Metal 1 (5nm Cr/ 75nm Pt) evaporation and lift-off

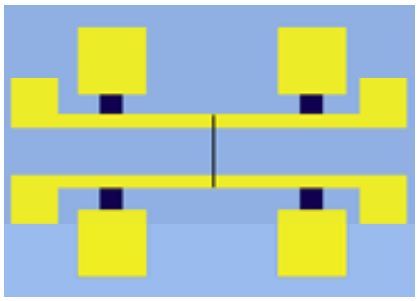

5. Third e-beam lithography to define tracks for Si heater

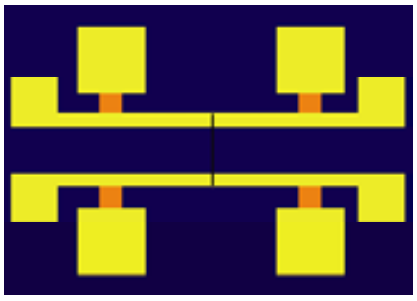

6. Metal 2 (5nm Cr/ 40nm Au)evaporation and lift-off

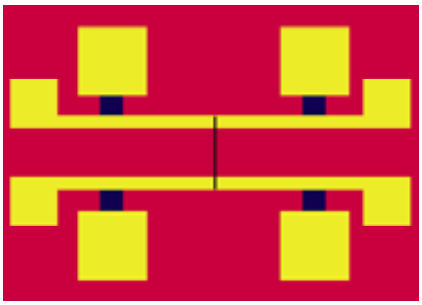

7. Etching. Top SiO2 and Si are removed. Metal 2 is removed

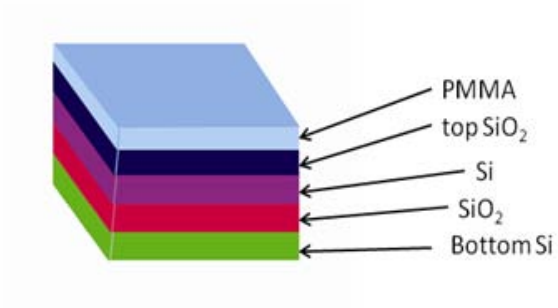

SOI chip covered with PMMA.

Fig. 6.16. Top view of fabrication process for Si heater with a nanotube suspended in the middle.

6.3.4 Si heater temperature characterization

To obtain the temperature coefficient of resistance α, the change in resistance of Pt thin film was measured as a function of temperature, in the same way as for Au heater. For both heating and cooling of the sample the R(T) relation was linear as expected, and the linear fit yielded α of $8.3 \cdot 10^{-4}$ K^{-1} for heating and $8.9 \cdot 10^{-4}$ K^{-1} for cooling. For further calculations the average α of $8.6 \cdot 10^{-4}$ K^{-1} is used. This value is about four times lower than the macroscopic value of $3.8 \cdot 10^{-3}$ K^{-1} (174).

For thermal measurements the device from fig. 6.15 was bonded on the printed circuit board with thin Al wires and placed in vacuum chamber with pressure of $3 \cdot 10^{-5}$mbar.

The device consisted of independent heating and sensing circuits. Keithley 2400 multimeter was used as a current source for the silicon heater (Fig. 6.17a). The current was directly injected into the heating circuit leading to Joule heating of the beam.

To control the device temperature Pt sensor was used (Fig. 6.17b). A precise constant resistance resistor (R_T) of 2 kΩ was connected with the Pt sensor (R_{Pt}) in series. When the heating process began, a constant, low voltage was imposed on these two resistors (100mV), and the resistance change of R_{Pt} led to a corresponding change of the voltage drop of R_T. Thus, the average temperature variation of the Pt layer during the heating process could be examined by recording the voltage variation at the joint point of R_{Pt} and R_T, indicated as V_T. The R_{Pt} was calculated from:

$$R_{Pt} = \frac{V_T}{V_{in} - V_T} R_T \qquad (6.4)$$

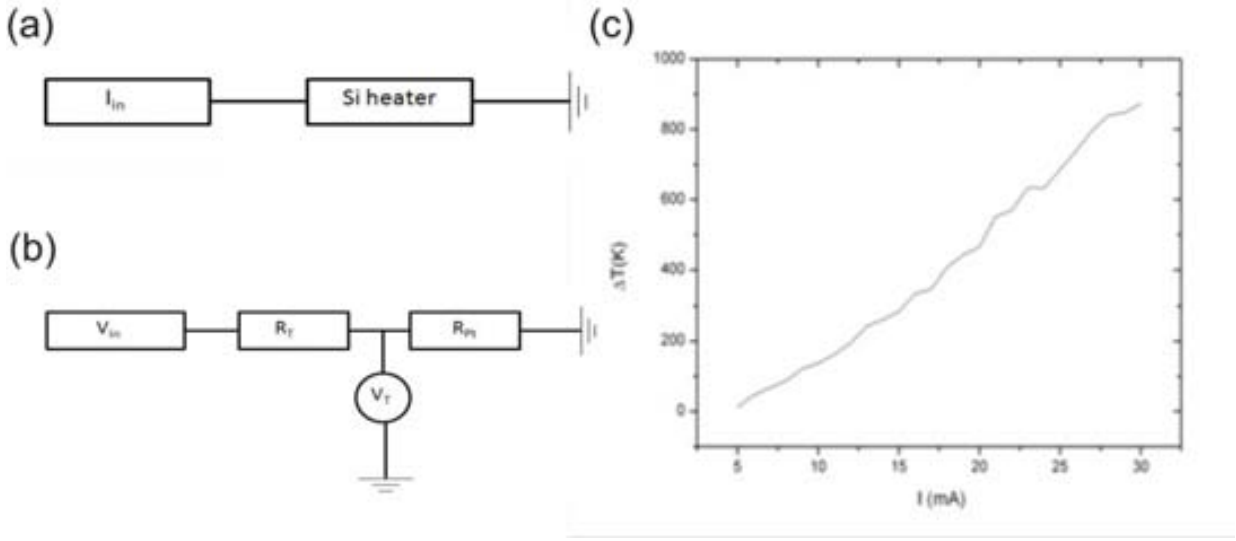

Fig. 6.17. (a) Si heater operating circuit (b) Pt temperature sensor. (c) Average temperature of the heater as a function of applied current.

To calculate the temperature of the platinum we use equation (6.1). At applying 30 mA on the Si heater (which corresponded to voltage of 5.7V between the contact pads) the heater broke. The maximum temperature was 850°C for dissipated power of 171 mW (Fig. 6.17c).

This value, however, is only estimation. One has to take into account that standard Pt RTD is reliable only up to 550°C; therefore the value of T_{max} can have a big uncertainty. Apart from that, the high

temperature achieved seemed promising for inducing large thermal gradients along the carbon nanotube.

6.3.4 Integration with nanotube motor and etching problems

Integration of the MWNT motor with the heater is similar as described in section 6.2.7. First of all, MWNTs were deposited on chips with pre-fabricated marks, and then good nanotubes were searched for with AFM microscope. The nanotubes should ideally be aligned parallel to one of the chip edges. Then on top of the nanotube we performed lithography steps to define a heater and cargo, and finally the etching, as described in section 6.3.3.

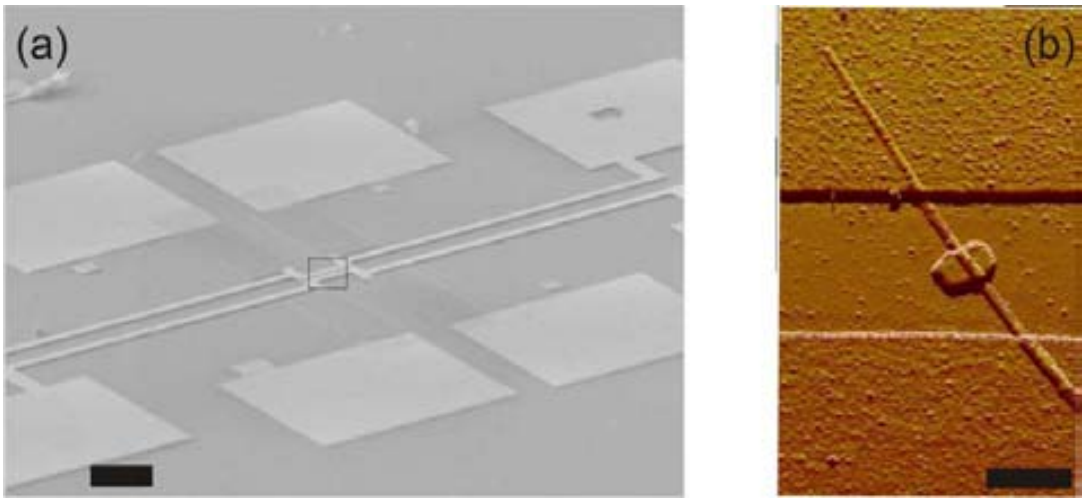

Fig. 6.18. (a) SEM image of the silicon heater with nanotube after the etching. Nanotube motor is located in the rectangle. Scale bar: 20 μm. (b) AFM image of the nanotube motor. Scale bar: 500 nm.

After fabricating various devices (Fig. 6.18) we noted two problems after the etching:

(1) In all devices the nanotube was not suspended between the contacts;
(2) In some devices silicon heater's resistance was infinite.

To investigate the source of the problems focused ion beam (FIB) cross section was done in the region of the nanotube and the heater. In the Fig. 6.19a a silicon heater is shown with a nanotube, which is not suspended between the contacts. The contacts are cut with the direction marked by the arrow. From the Fig. 6.19d one can see that the MWNT is lying on the surface and the Si layer underneath was etched away. This is possible when the liquid can enter under metal mask. In principle, it should not happen. However, if the adhesion between metal and nanotube is not good we can expect capillary forces to enhance the penetration of liquid under the contacts.

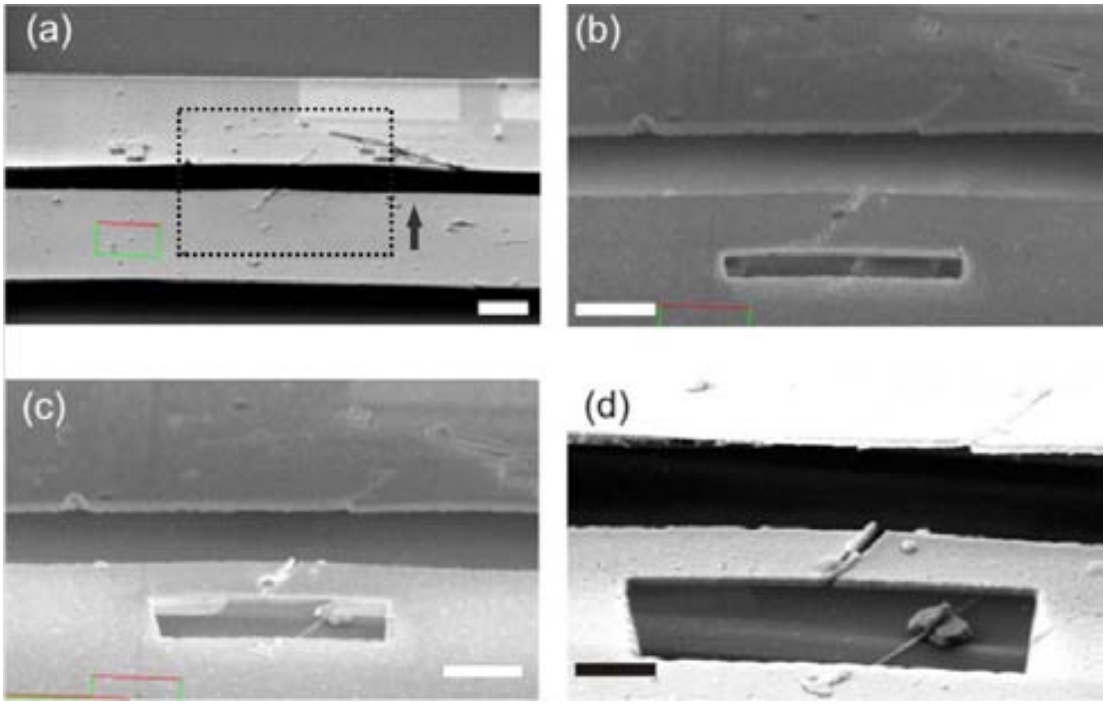

Fig. 6.19. FIB cross-section in the region of MWNT. Dotted rectangle marks the region of the CNT motor and the arrow marks direction of the cut. Scale bar: 1 μm. The cut was performed by J. Llobet (CNM-IMB).

To understand better how the structure of Si heater under the Pt tracks is we cut perpendicularly to the track. In the Fig. 6.20 cutting is shown step by step.

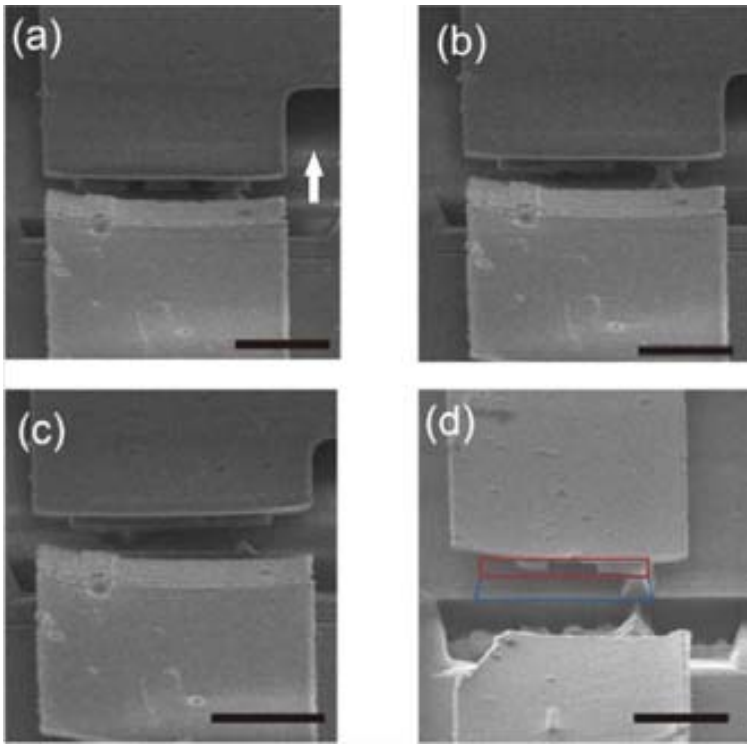

Fig. 6.20. (a) – (d) FIB cross-section of the the Si heater (J. Llobet). Arrow points the direction of the cut. In (d) red and blue lines correspond to the expected SiO_2 and Si shapes after the etching, respectively. Scale bar: 1 μm.

The red and blue shapes mark the desired shapes of SiO_2 and Si layers, respectively. Apparently, major parts of those layers were etched away. The reason why the HF and KOH can penetrate under the platinum mask is probably the poor adhesion of the metal to the surface, which was also observed in the case of platinum heaters. Also it is probable that Pt layer had some pores through which the liquids can enter.

6.3.5 Bi-metallic layer for silicon heaters

To improve adhesion of the Pt layer to the surface we introduced second metal layer under platinum: gold. From our previous experience gold sticks well to both Si and SiO_2 and sustains etching in HF and KOH.

A test structure consists of a MWNT placed between two large contacts of 5 nm Cr, 50 nm Au and 5 nm Cr, 50 nm Pt. We performed the etching as described in section 6.3.3: buffered hydrofluoric acid 5% for 5 min, 40% KOH at 75°C for 3 min and finally gold was removed for 1 min. After etching and drying the sample in hot IPA the nanotube remined suspended between the electrodes. Also we performed FIB cross section of the contact structure, which revealed no defects in Si structure.

Using the bi-metal layer can solve the problems of adhesion during the etching, however it requires one more EBL step to complete the nanotube motor and make the process too time consuming. Therefore we decided not to continue with this approach.

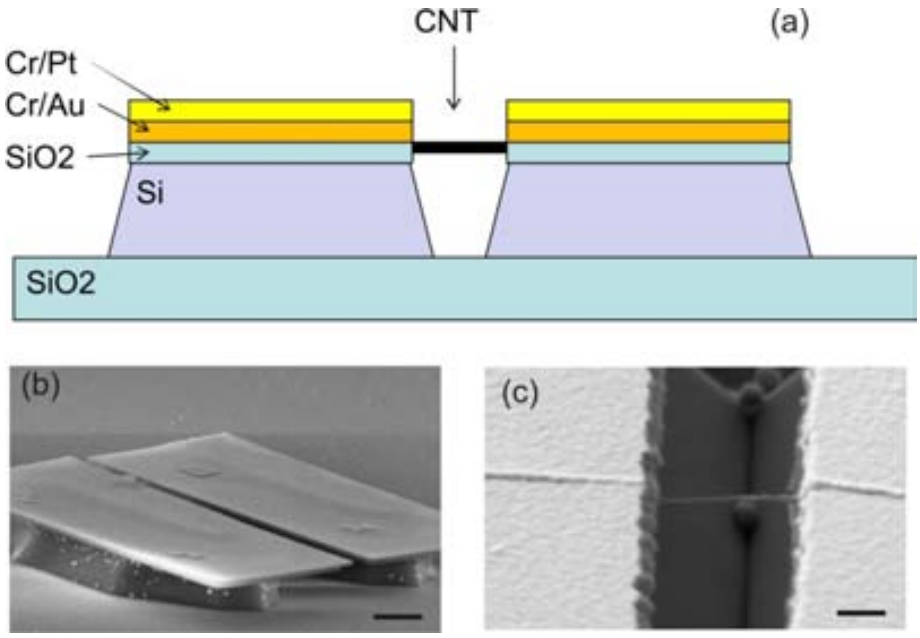

Fig. 6.21. Silicon heater with platinum-gold thin layer. (a) Schematic of the motor with bi-metallic layer (b) tilted SEM image of the heater tracks (b) nanotube suspended between the contacts, scale bar: 1 μm.

6.4 Conclusions

We report fabrication of two types of micro-heaters for high temperature applications. Even though it was impossible to integrate those heaters with CNT motor, they can be useful for other purposes, such as growing nanowires or other nanostructures. Big advantage is that the structures grown on top of the heaters are already electrically connected and ready for electrical or transport measurements.

The main advantage of the gold heater is fast and easy fabrication (one lithography step) and small size (20x2 µm). If the heater is to be used for a prolonged time, to avoid electromigration it is recommendable to apply low frequency AC voltage (not tested in this thesis).

For a non-suspended silicon heater the main advantage is for sure lack of maximum current density, which allows passing big currents and achieving high temperatures. The preliminary results with double metal layer are optimistic, however the fabricating process is very time consuming. After some modifications the heater can have other applications, for instance in gas sensing.

7. Graphene heaters: a way to all-carbon electronics

7.1 Introduction

In the recent years graphene has attracted a huge amount of attention because of its outstanding electrical, mechanical and chemical properties. Strong sp^2 bonds lead to thermal conductivity ~10-20 times higher than silicon, 5-10 times higher than copper and comparable to the one of isotropically pure diamond. The outstanding thermal conductivity of graphene films provides another advantage for using graphene for heating applicatons: it quickly delivers heat to the environment. For macro-scale applications transparent, conducting films of graphene are used to replace indium tin oxide (ITO) in displays, solar cells and transparent heaters. Those heaters can reach sizes of 4x4 and 9x9 cm^2 and maximum temperatures of 100 and 65°C, respectively (175).

In the micro-scale understanding power dissipation is a challenge in modern and future electronics. It is also an interesting domain for fundamental research at the intersection of electron-phonon interactions. The energy dissipation and transport in CNTs and graphene can be better understood by measuring their temperature during Joule heating by electrical current flow. Assuming a uniform heating rate per unit length $P/L \approx I^2(R - R_C)/L$, where R is the total resistance, R_C is the resistance of two contacts the temperature profile $T(x)$ of a CNT on a substrate (Fig. 7.1a) can be described as (176-177):

$$T(x) = T_0 + \frac{P}{gL}\left[1 - \frac{\cosh(x/L_H)}{\cosh(L/2L_H)}\right] \qquad \text{for} - L/2 < x < L/2 \qquad (7.1)$$

Where T_0 is the temperature of the contacts at the two ends, $L_H = (\frac{kA}{g})^{1/2} \approx 0.2\mu m$ is the characteristic thermal length along the CNT, k is the thermal conductivity and g is the net heat dissipated to the substrate per unit length.

For a suspended (Fig. 7.1b) CNT the temperature profile can be described as (178):

$$T(x) = T_0 + \frac{P}{2kAL}\left[\left(\frac{L}{2}\right)^2 - x^2\right] \qquad (7.2)$$

For $-L/2 < x < L/2$. Power dissipation is assumed to be uniform along the CNT length.

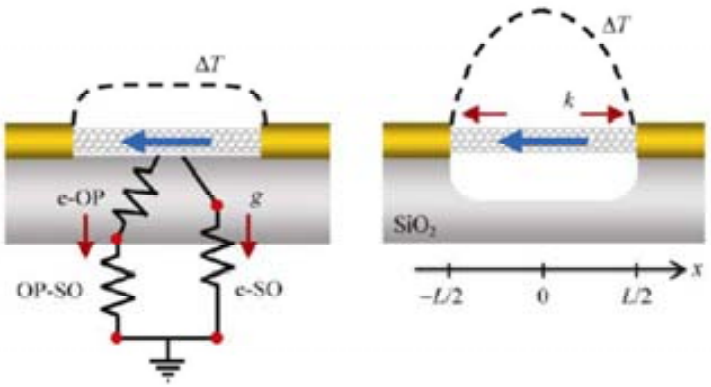

Fig. 7.1. Supported and suspended CNTs. Red arrows show direction of heat flow. In the supported CNT, electrons scatter with device optical phonons, which then couple with the substrate. Electrons may also dissipate energy directly to surface-optical phonons of the substrate. Adapted from (179).

Since graphene is considered a promising material in this context, various studies were performed in order to understand power dissipation and Joule heating of mono and bilayer graphene on the surface (180, 181).

Graphene is able to carry very high electrical currents without sustaining damage. Applying a source-drain bias V of a few volts across the sample induces a large current flow I of a few milliamperes. For a sample of width of ~1µm and thickness of 0.35 nm, this results in extremely high current density J of a few 10^8 A/cm^2. For comparison, J is only a few times larger in carbon nanotubes and for both materials, it is several orders of magnitude larger than in present-day interconnects (109, 182). The effects of a large electrical current passing through a mesoscopic, conducting device include electromigration and Joule heating (183-185).

The power dissipated is related to local current density and electric field (F) in samples larger than the carrier mean free path (*p=JF*). Therefore a graphene field effect transistor (FET) with large applied bias should have regions of varying power dissipation related to local charge density and electrostatic profile, which results in spatial modulation of the device temperature (Fig. 7.2).

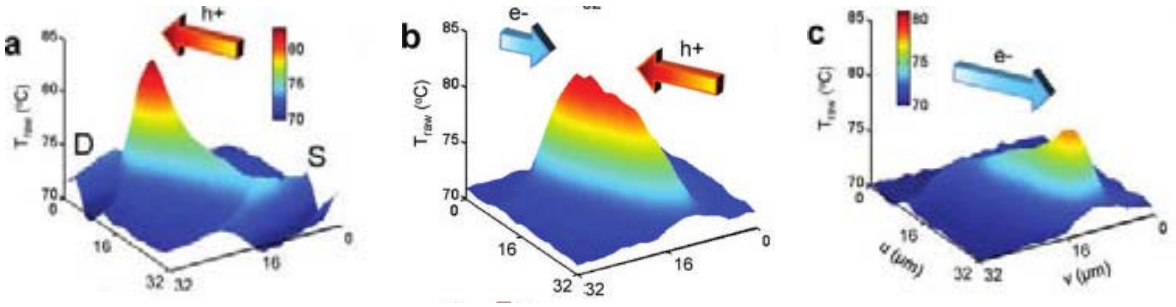

Fig. 7.2. Electrostatics of the monolayer graphene FET hot spot. Imaged temperature map at (a) V_{GD} = -3.7 V (hole doped), (b) V_{GD} = 3 V (ambipolar), and (c) V_{GD} = 12.2 V (electron-doped conduction) with corresponding V_{SD} of 10, 12, and 10 V, respectively (approximately same total power dissipation). Adapted from (180).

7.2 Fabrication

To fabricate graphene heaters we used exfoliated graphene on highly doped Si chip covered with 495 nm of SiO_2. This specific thickness enabled us to see the graphene flakes under the optical microscope (Fig. 7.2a). We chose big flakes of approximately 3-5 layers, because they are more mechanically robust, which may be an advantage during the etching.

Then we deposited alignment marks by means of e-beam lithography and metal evaporation on the pre-determined positions with good graphene flakes. To structure graphene we used reactive ion etching (RIE) of 10% oxygen plasma at 20W for 3-4 min. As a mask a double layer of PMMA 950 was used, with openings made by means of e-beam lithography. In the exposed region (pink in Fig. 7.2b) all the graphene is removed, while the regions covered with PMMA (green in Fig. 7.2b) stay intact. After performing lift-off to remove the PMMA mask we are left with various parallel heaters of size 1x3 µm and separated by approximately 1 µm.

Next step was to deposit MWNTs on the surface. It was done randomly by spin coating nanotubes from the solution. To place the nanotubes on top of the heaters we used AFM option called Nanoman, which allows manipulation of the nanoscale objects on the surface. With Nanoman it is possible to move nanotubes over distances of a few microns and place them directly in the middle of the heater (Fig. 7.4). The biggest drawback of this method is that it is very time consuming, but on the other hand it allows precise manipulations of the devices.

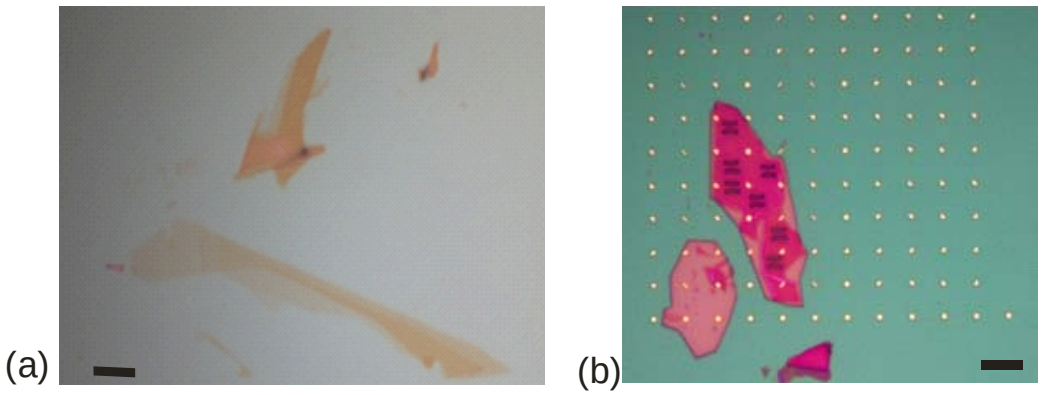

Fig. 7.3. (a) Optical image of a few-layer graphene. (b) Graphene with mask for RIE. Scale bar: 10 µm.

Finally, metallic contacts for the graphene heaters and a cargo on top of the nanotube were fabricated by means of e-beam lithogprahy and metal evaporation. AFM image of contacted device is shown in the Fig. 7.5a.

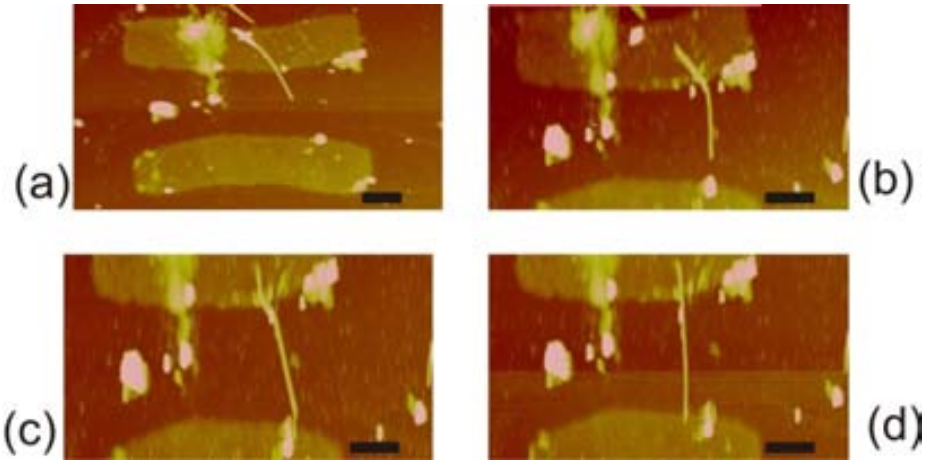

Fig. 7.4. Nanoman manipulation of MWNT. (a)-(d) Sequence of images showing alingning of a MWNT between two graphene contacts. With AFM It is possible to move the nanotube with great precision over a distance up to a few microns and place it on pre-defined position. Scale bar: 300 nm.

The contact resistance of multi-layer graphene was normally between 1 and 10kΩ. The contact resistance of the MWNT was typically in order of MΩ. To reduce the resistance the samples were annealed in 270°C in Ar and H_2 for one hour. This caused dramatic drop of contact resistance of the nanotubes, typically down to 20-100 kΩ.

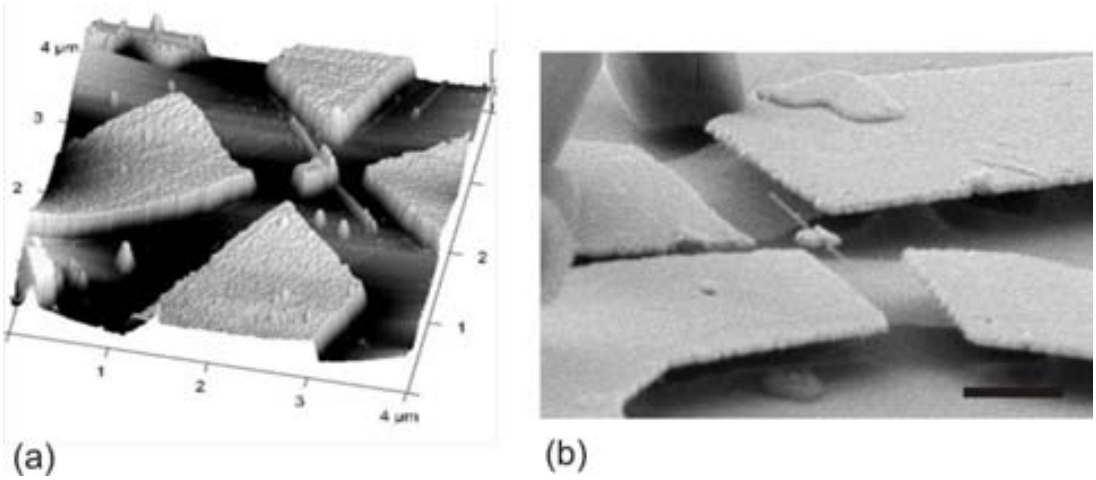

Fig. 7.5. (a) AFM image of a thermal motor with graphene heaters. (b) SEM image of suspended device. Scale bar corresponds to 1µm.

Afterwards, we applied electrical breakdown technique to remove a few outer shells of the nanotube and enable the movement of the cargo along the nanotube. So prepared devices were suspended by removing ~300 nm of SiO_2 in buffered hydrofluoric acid and dried in critical point dryer (Fig. 7.5b). For the details of nanofabrication see *Annex A*.

Electrical breakdown and etching are the critical steps in the fabrication of the devices, because of the high risk of breaking of the MWNTs. Up to now it was impossible to fabricate a good device, however the work remains in progress.

7.3 Graphene mechanical cleaning

One of the problems related to graphene devices is contamination due to residues from nanofabrication, which can introduce background doping and reduces electron mobility. For samples

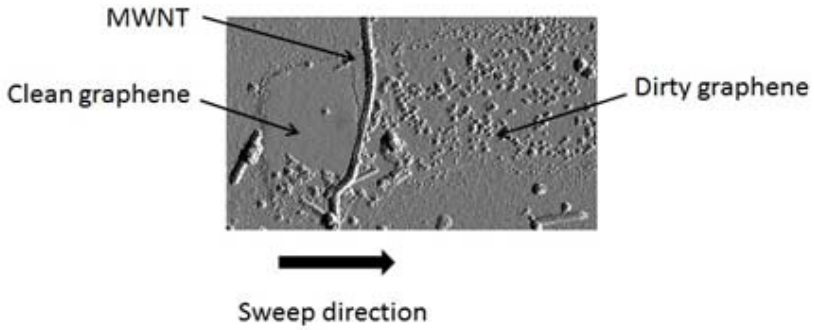

Fig. 7.6. Mechanical cleaning of graphene. The contamination is removed from the surface by sweeping a MWNT.

of high electronic quality, post-lithography cleaning treatments are therefore needed. A simple and highly reproducible method to remove contamination of graphene was proposed by Moser *et al*. (185). The method consists of applying high current (up to a few milliamperes for a device of few microns wide) through the graphene device. The high current density is shown to remove contamination adsorbed on the surface. Recently, mechanical cleaning based on contact mode atomic force microscopy was reported to remove residues and significantly improves the electronic properties (186).

Here, we present a mechanical cleaning of graphene with a carbon nanotube. While moving a MWNT on top of graphene with AFM tip, we observed that the nano-scale contamination is effectively removed (Fig. 7.6). This method is non-invasive and allows cleaning large graphene surfaces (up to 1x1 µm with one sweep). With growing efforts of integrating garphene and CNTs it can be useful for fabricating future devices.

7.4 Graphene heating properties

Thermal characterization of graphene heaters was performed in the SEM/FIB chamber (CrossBeam 1560 XB, Zeiss) in the clean-room of CNM-IMB, Barcelona. The samples were measured in vacuum of ~10^{-6} mbar to minimize the influence of the environment and were imaged using the SEM imaging. We used two tungsten tips to contact the source and drain of a graphene heater. The tips were then connected to the external voltage source. While increasing the current passing between the source and drain we should observe Joule heating of the device. Since the device is suspended the only heat sink should be the contacts and the temperature is expected to be the highest in the middle of the device. During the heating we recorded SEM images with the speed of 1 frame per 200 µs. This enabled us to further correlate SEM frames with I-V values registered by the LabView program.

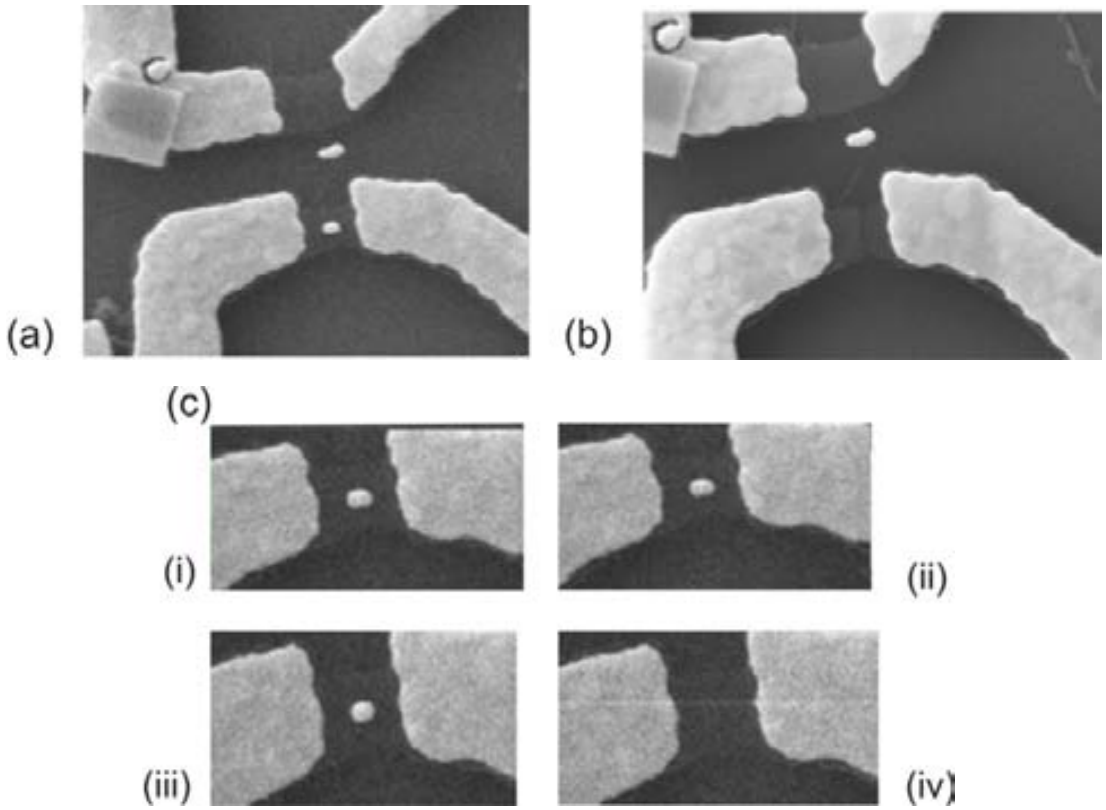

Fig. 7.7. (a) Device before experiment, arrow marks current direction (b) Device after heating. The plate evaporated and graphene is broken. (c) Sequence of images taken while increasing source-drain voltaget: (i) I=0, V=0; (ii) V=2.7 V, I = 190 μA; (iii) V = 2.9 V, I = 207 μA; (iv) V=3V, I=214μA.

To verify the temperature range of graphene heaters we deposited some Au plates on top of the devices (Fig. 7.7). While increasing the current we observed melting/evaporation of the material, meaning that the heater reached temperature of ~1200°C. Some of the devices broke after the gold evaporated, but some stayed as before and their conductance increased. This is a proof that the heaters can reach extremely high temperature and operate for various cycles.

Afterwards we investigated the heat transfer between graphene heater and a CNT. For that purpose we use one of the devices where the CNT was broken during the electrical breakdown. On one side that nanotube is in contact with the heater, on the other side it was probably touching the substrate (Fig. 7.8a). With increasing the power dissipated on the graphene the heat was transferred to the nanotube and the gold cargo melted and evaporated (Fig. 7.8b, c). This is a proof that heating with graphene can create extremely high temperatures without destroying it and induce thermal gradient on the nanotube comparable with the one reported in ref. 114.

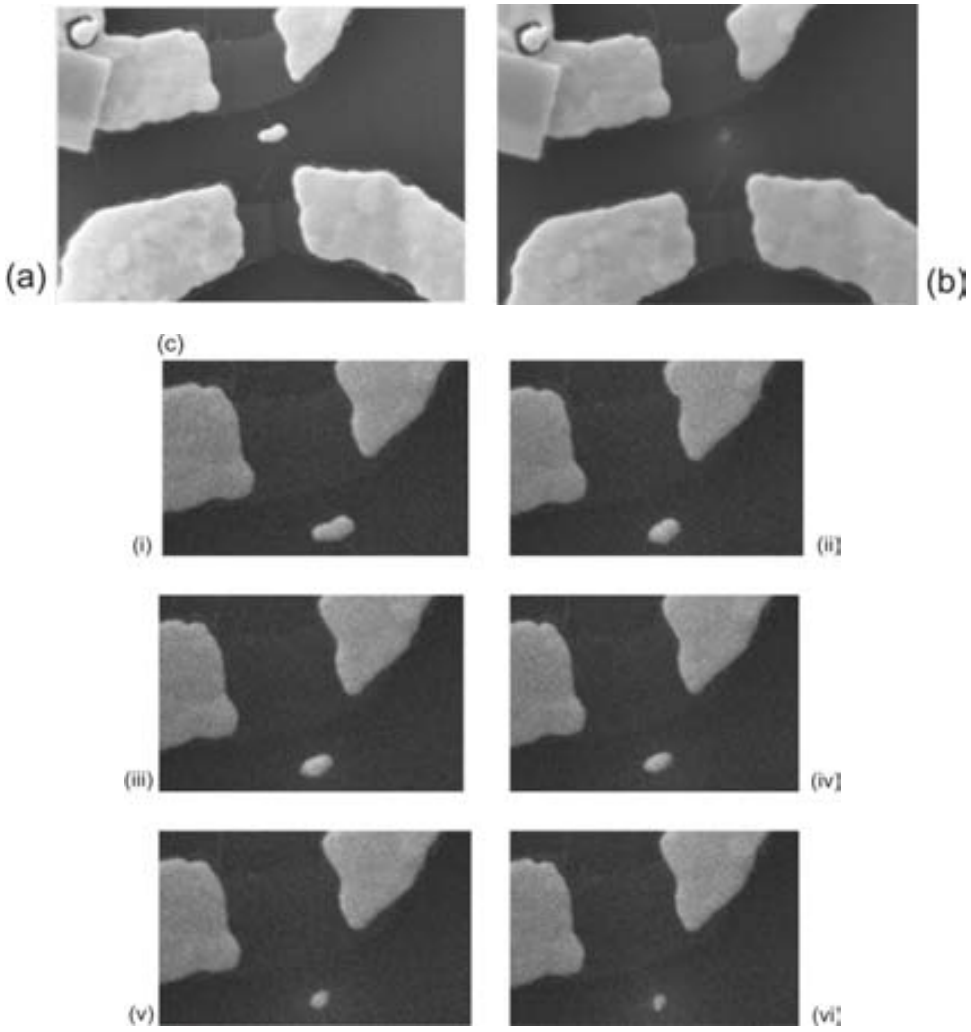

Fig. 7.8. (a) Device before applying the current (b) Device after heating experiment. The cargo deposited on the nanotube melted and evaporated, however both graphene heater and the nanotube are not damaged (c) Sequence of images taken during the heating. Plate deposited on top of the nanotube melts and evaporates. The images are a little out of focus due to high charging of the sample.

7.5 Conclusions

We report a way of fabricating devices which integrate graphene and carbon nanotubes. The suspended graphene can work as an effective heater, operating with temperatures up to 1200°C. The high temperature can not only finally enable experimental realization of controlled thermal gradient motor, but also be applied in future micro and nanoscale heaters, for instance in gas sensing. The devices in similar configuration can also have application as all-carbon transistors and coupled resonators, being another step forward in the direction all-carbon electronics.

8. Carbon Nanotube Electron Windmill

In collaboration with Mariusz Zdrojek.

8.1 Introduction: Chiral currents in CNTs

Carbon nanotubes are cylindrical forms of rolled graphene sheets and most of them have chiral atomic arrangements and since a chiral nanotube has a helical structure it is natural to imagine that a current can also flow along a screw line along the tube's circumference even though the applied electric field is along the axial direction (Fig. 8.1). Therefore, under applied electric field the velocity of electrons passing through the CNT can be divided into two components, as shown in the Fig. 1. The first component is a translational velocity along the tubule axis (J_z), and the other is a cyclic velocity along the tubule circumference, so called chiral current (J_c). The chiral angle of the current is defined as $\alpha = \tan^{-1}(J_z/J_c)$.

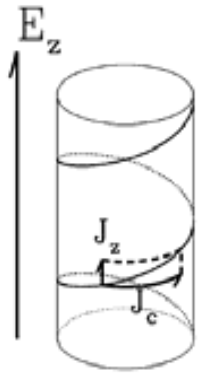

Fig. 8.1. A schematic diagram of a chiral current on a tubule under an applied electrostatic field E_z along the tubule axis. Jz and Jc denote translational and cyclic components of the current, respectively (187).

First-principle calculations by Miamoto *et al.* suggested that chiral currents in nanotubes are not significant (187). However this was a consequence of the metallic structure of the investigated nanotube. Recent studies by Lambert *et al.* show that non-metallic CNTs can carry large chiral currents (188).

Following a standard notation (28), also described in Introduction, lattice vectors a_1 and a_2 are introduced. They are defined as $a_1 = (\sqrt{3}/2, 1/2)a$ and $a_2 = (\sqrt{3}/2, -1/2)a$, where $a = \sqrt{3}a_{c-c}$ and a_{c-c} = 1.44Å is the carbon-carbon bond length. In this notation, (n,m) CNT, where $(0 \leq m \leq n)$ are integers, is then defined by a transverse chiral vector $C_h = na_1 + ma_2$, which wraps around the CNT circumference and a longitudinal translation vector T. We are interested in resolving the velocity component v_x, parallel to the C_h. In Fig. 8.2 the black curve show the total velocity v_x carried by the right-moving electrons. For metallic (8,8) nanotube the total transverse velocity is zero, in agreement with previous calculations. However, for non-metallic nanotubes the total velocity is non-

zero. Moreover, energy dependence of the chiral currents on energy is surprisingly rich. They can change sign and oscillate as the energy of the electrons is increased (188).

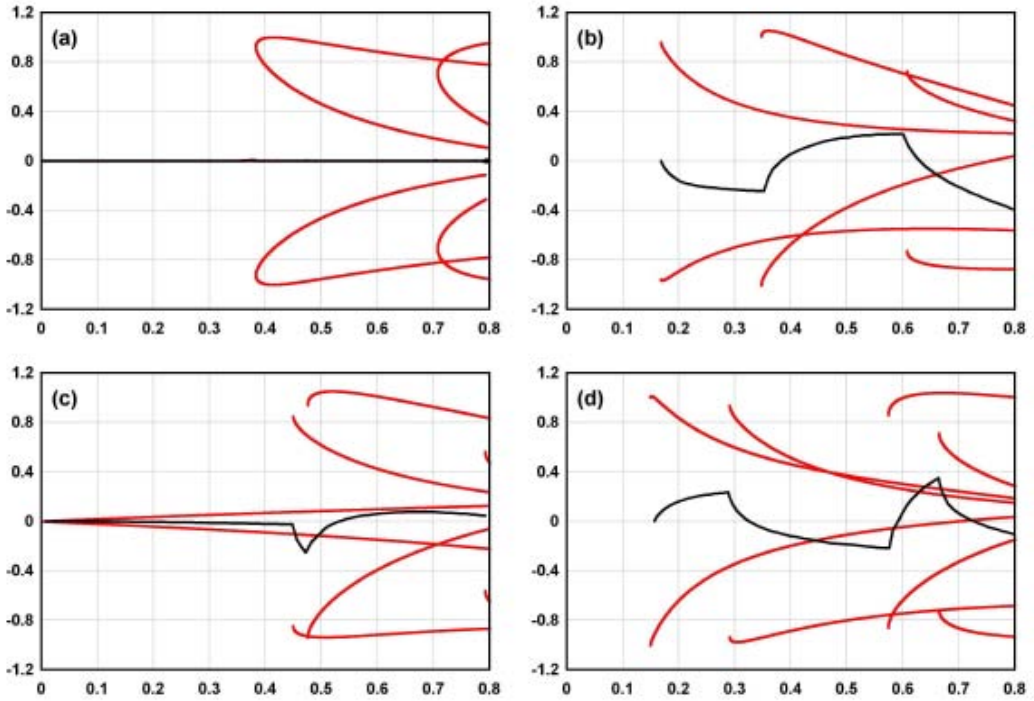

Fig. 8.2. Velocity components for the (8,m) family of CNTs plotted against the energy E (eV), where m = 8, 4, 5, 6 in figs (a) to (d) respectively. The red curves show the transverse velocities $v_x(q, k+y(q,E))/v_F$ of right-moving electrons belonging to individual channels q. The black curves show the total velocity v(n,m). Adapted from (188).

The value of chiral angle which maximizes chiral current in the tube is of 18°. The existence of chiral currents also can generate a large internal magnetic field. According to Lambert et al. for longitudinal current of order 10^{-4}A the field can reach 0.1 T, which is enough to produce spintronic effects and contribution to the self-inductance.

Chiral nanotubes and nanowires are interesting for possible applications related to external magnetic fields (189) and nanoscale inductors (190). Also it has been proposed to use chiral tubes as building blocks in chiral nanomotors. Up to date various systems such as CNTs, boron-nitride nanotubes (191), single-walled gold nanotubes (192) and iron-filled CNTs (193) have been studied.

The new mechanism to drive a CNT motor using chiral current was proposed by Bailey *et al.*. It is based on a double-walled nanotube, where part of the achiral outer tube has been removed and the outer tube is clamped with metal electrodes (194). The chiral inner tube serves as a rotor, see Fig. 8.3a.

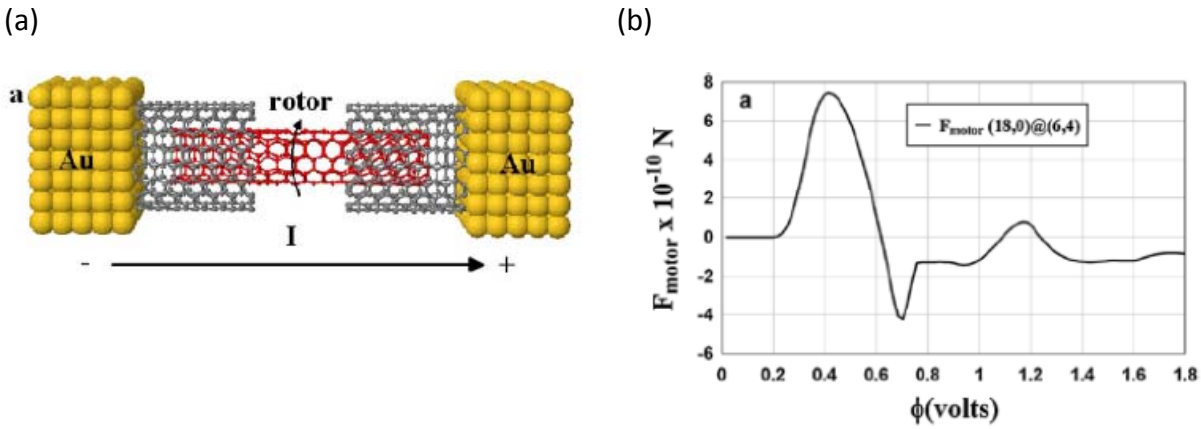

Fig. 8.3. (a) Design of the electron windmill. The inner tube (red) rotates with respect to the outer (grey). Outer tube is attached to gold electrodes, which serve as electron reservoir. (b) Tangential force (Fmotor) exerted on (18,0)@(6,4) nanodrill as a funcion of voltage applied across the device. Adapted from (194).

In that configuration the driving force arises when DC voltage is applied across the device. It produces a "wind" of electrons (therefore the name – electron windmill) coming, for example from left to right. The incident part of the current moving along the chiral vector of the achiral tube posses zero angular momentum, but after interacting with the inner chiral tube the outgoing current possesses a finite angular momentum. The details of the calculations can be found in ref. 194. To explain it briefly, one can say that momentum of the right moving electron is $M=m_e \cdot v_x$, where $m_e$is mass of electron, and v_x is the chiral velocity. Then the total momentum carried by the electrons induces a force on the inner tube causes its rotation. In Fig. 8.3b driving (tangential) force for on (18,0)@(6,4) nanodrill as a function of applied voltage is shown. The maximum force is in the order of magnitude of 10^{-10} N. It is also interesting that the force can change sign, meaning the rotor will change the direction of motion.

The important question is, whether the driving force can exceed the inter-shell nanotube friction. For approximately 4000 overlapping atoms between inner and outer tube static friction F = 10^{-15} N/atom and dynamic friction $F_c = 4 \cdot 10^{-12}$ N. It is almost three orders of magnitude lower that the driving force.

There could be many possible applications of electron windmills. Similar to the spin torques in magnetic point contacts and tunnel junctions, a CNT windmill may have applications in nanoscale memory elements. The other application could be switches, when an inner tube rotates by predetermined angle. While in contact with a reservoir of molecules it can also serve as a nanofluidic pump.

8.2 Sample preparation and measurements

The device consists of a MWNT synthesized by arc-discharge evaporation in standard transistor configuration, with the channel length of typically 1 um. Then a few outer shells were removed with burning technique and a small (250x400 nm) cargo is placed on top of the nanotube by means of e-beam lithography and metal evaporation (Fig. 8.4a). In the last step the device is suspended by means of wet etching, with around 300 nm of the substrate removed and hot IPA drying (Fig. 8.4b). In total, the fabrication of each device requires three lithography steps (alignment marks, contacts and cargo), making it very time consuming. The fabrication process is described in details in the Annex A.

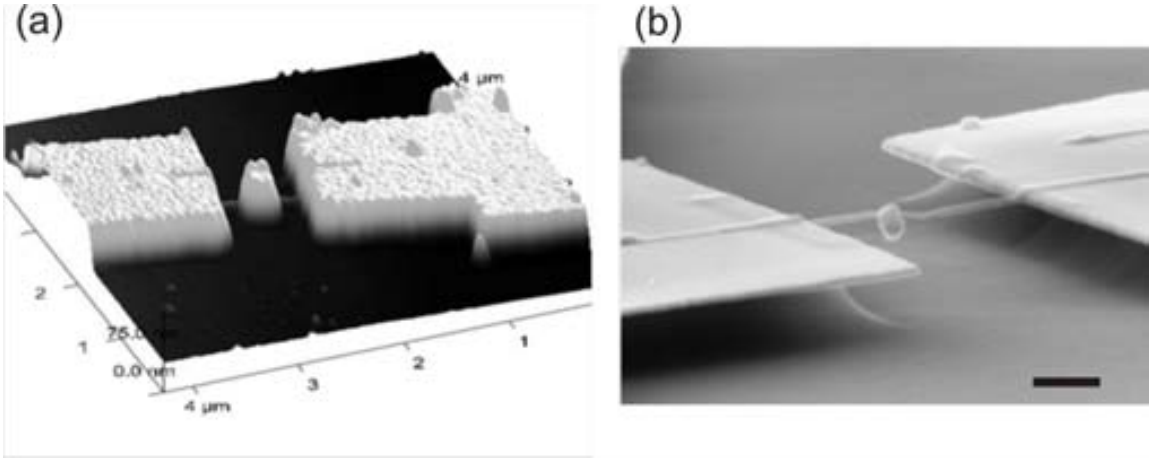

Fig. 8.4. Electron windmill. (a) AFM image of device before suspending. (b) SEM image of a suspended device. Scale bar: 1 µm.

The measurements were performed in the SEM/FIB chamber (CrossBeam 1560 XB, Zeiss) in the clean-room of CNM-IMB, Barcelona. The samples were measured inside the vacuum of ~ 10^{-6} mbar to minimize the influence of the environment and were imaged with the SEM during the measurements.

The measurement set-up is shown in the Fig. 8.5a. We used two tungsten tips to contact the source and drain of a nanotube device. The tips were then connected to the external voltage source (DAC), controlled by the LabView program. The back-gate voltage was applied through the stage of the SEM chamber also connected to the external source (Keithley 2400). The main advantage of this setup is the ability to image the device in real time (Fig. 8.5b), so if any movement is observed it can the correlated to a certain source-drain and gate parameters. The typical I-V characteristic is shown in Fig. 8.5c. The wait time between increasing voltage of a step of 1 mV was from 50 to 100 ms.

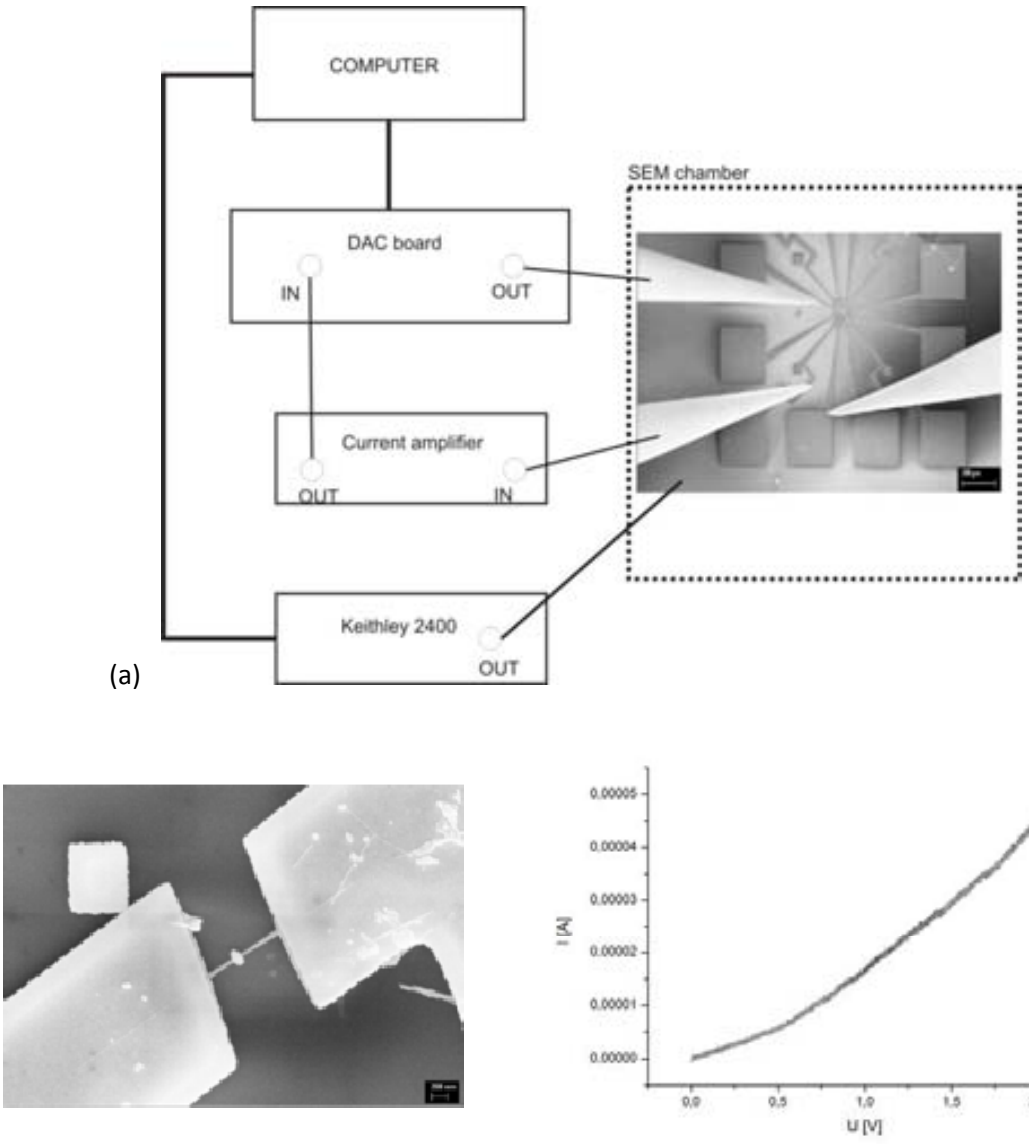

Fig. 8.5. (a) Measurement scheme. The tungsten tips inside the SEM chamber are contacted to the large contact pads, which are source and drain of windmill device. (b) SEM image of a device during the experiment. With SEM we can image the devices in real time. (c) Typical I-V curve for electron windmill. Even though the highest chiral currents are predicted for low voltages we increase the voltage to induce Joule heating of the sample.

8.3 Discussion

Even though chiral currents were predicted to be the highest for low voltages, we increased the voltage almost to the point of CNT breaking. This was to induce Joule heating along the CNT, which is an effective way of removing organic residues from the carbon surface, such as PMMA. It also leads to removing of the dangling carbon bonds of the outer shell, left after shell-burning. Dangling bonds, along with the PMMA residues, can be one of the factors which lead to increasing of the inter-wall friction and therefore obtruding the rotation.

After measuring various samples of different diameters and different number of shells removed, we did not observe the rotation of the metal cargo. That would suggest that either the devices are not properly engineered or the driving electron torque is not big enough to overcome the friction.

8.3.1 Rotating the plate with electric field

In order to verify if the cargo has the possibility to rotate we repeated the experiments of Bourlon *et al.* in which the motor is actuated with electric field (109).

The suspended CNT motor was placed between two side-gates and highly-doped Si substrate back gate. The plate was asymmetrically positioned with respect to the tube so that the longer section can be electrostatically attracted to one of the side electrodes. In that experiment we tried to rotate the cargo with the electric field. The voltages up to 80V are applied to the Si backgate and the nanotube is imaged with the SEM.

This experiment was performed to check if the devices were well fabricated and whether the inner tube was free to rotate with respect to the outer one. Indeed, for various devices rotation can be achieved for high electric fields, as shown in the Fig. 8.6. Importantly, the plate stays in its position when the bias is switched off. This means that the rotation is not enabled through the torsion of the tube. The latter would return the plate to the initial position. However, those devices do not rotate while passing the current. That would suggest that friction force is higher than expected.

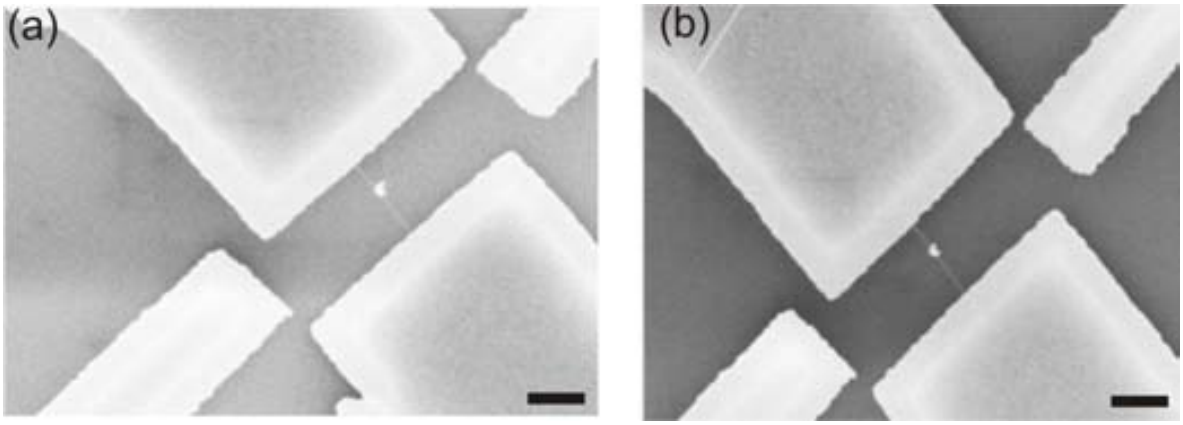

Fig. 8.6. Rotating the plate with electric field. (a) CNT windmill before the experiment (b) and after applying 80V on the backgate. Scale bar: 1 μm.

8.3.2 Influence of CNT edges

Important factors that can impede device rotation are defects and structural irregularities at nanotube edges. To investigate nanotubes structure we took TEM images of randomly dispersed MWNTs from the same batch as the ones used for fabricating the motors. In the majority of nanotubes we did not observe defects in the centre of the tube. On the contrary, region close to the edges of nanotubes very often was defective and irregular. With edges such as in Fig. 8.7b and c it is impossible for the inner tubes to rotate with respect to the outer walls.

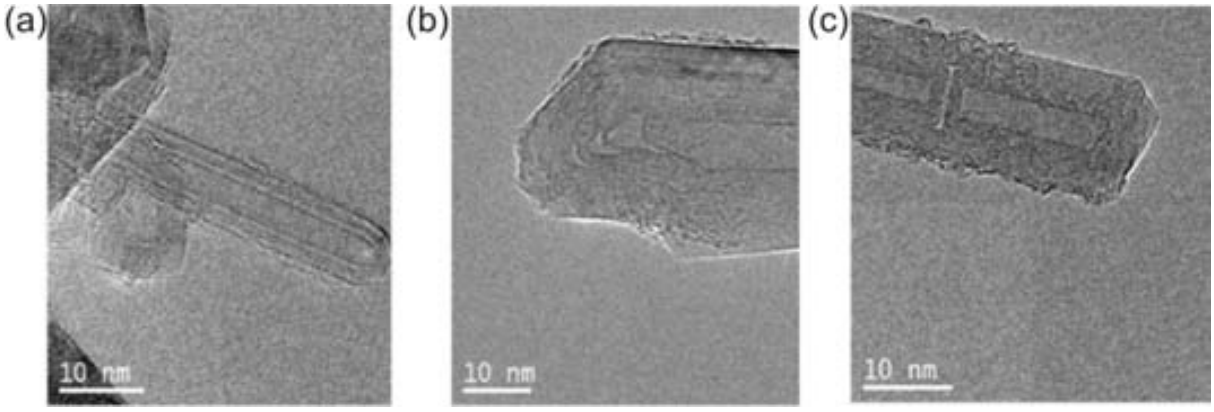

Fig. 8.7. (a-c) TEM images of MWNTs of the same origin as the ones used for the windmill experiment. Some of the tubes show irregular and defected edges which can obtrude rotation (courtesy of MariaJose Esplandiu).

The big drawback is that is impossible to spot irregular edges of the tubes during the fabrication process, since they are invisible in AFM or SEM. To overcome the problem we designed a new device layout that enables to remove the influence of the nanotube ends, shown in the Fig. 8.8a.

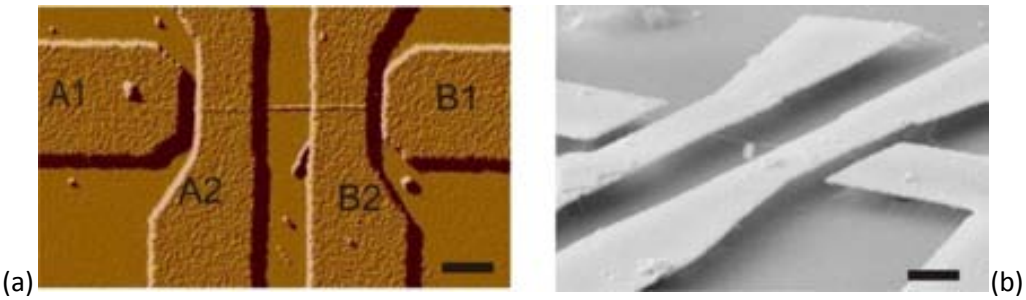

Fig. 8.8. (a) Improved design of CNT windmill. The actual device is between two inner electrodes, outermost parts of the tube will be destroyed, to reduce the influence of the nanotube ends. (b) SEM image of fabricated device. Scale bar 1 μm.

The modified design consisted of four contacts, two on the right (A1, A2) and two on the left (B1, B2). The A2 and B2 contacts served as actual source and drain for the windmill device. After suspension in SEM chamber between outermost contacts, A1 and B1, and inner contacts, A2 and B2 respectively, we passed high current, until the nanotube between them was broken. Now the edges of the MWNT, under A1 and B1 were not anymore connected to the motor. This procedure was repeated for approximately 10 devices (Fig. 8.8b); yet we did not observe the rotation while performing the experiment.

8.3.3 Friction force estimation with AFM

The final step of the experiment was to estimate the inter-wall friction of fabricated devices. It is predicted that the inter-wall friction is low (195), but as mentioned before, the dangling bonds or irregularities at the edges of the tube may increase the friction and obtrude the movement. The static friction depends on the number of overlapping atoms, which in our case was much bigger than in the calculations.

To determine the friction in our devices we used the AFM in contact mode. To calculate the contact force between the tip and sample it is important to obtain a good force curve, as shown in Fig. 8.9.

The basic approach to obtaining a good force curve entails adjusting the Z motion of the piezo relative to the sample and shifting the graph so the pull-off point of the tip displays on the graph. The force curve clearly illustrates the relation between the setpoint and the cantilever deflection voltage.

Deflection sensitivity, extracted from the force curve, allows conversion from the raw photodiode signal in volts to deflection of the cantilever in nm. Sensitivity is equal to the inverse of the slope of the force curve while the cantilever is in contact with hard sample.

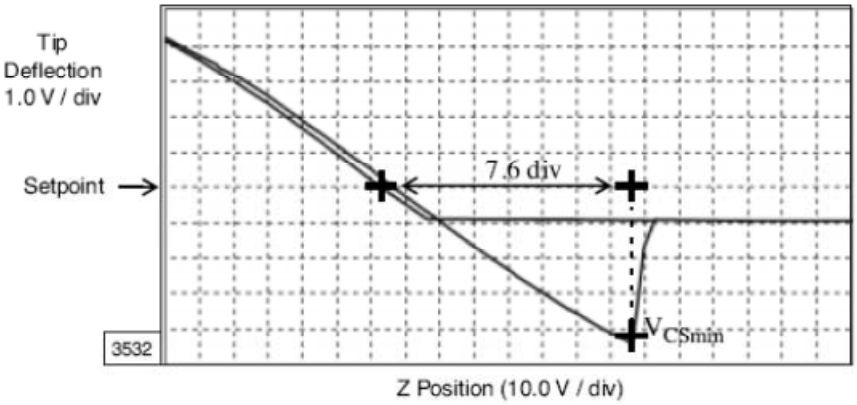

Fig. 8.9. Example of a force curve. Inverse of the slope of the force curve is equal to the deflection sensitivity (196)**.**

Because the setpoint defines the value of the deflection signal maintained by the signal loop the force curve can be used to calculate the contact force of the tip on the sample when the spring constant k of the cantilever is known. The contact force is defined by the equation:

$$F = kd \qquad (8.1)$$

Where d is the deflection of the cantilever measured from the setpoint in nanometers (196).

To measure the force, we push on the cargo on top of the suspended motor increasing the deflection up to the point that the plate rotates (Fig. 8.10). The determined friction force was about 70-80 nN, for the Olympus micro-cantilever OMCL-AC160 TSG-W2 with the k= 42 N/m.

However, it was only estimation. The real force value can be slightly different due to the fact that the calibration was made on the SiO_2 surface and not on the nanotube. Still, the estimated value of friction is two orders of magnitude bigger that values of driving force calculated in ref. 194.

Assuming a region of overlapping atoms of ~1.2 µm and tube radius of 10 nm we obtain static friction of 1 MPa. This value is comparable with the ones reported earlier in literature: 0.85 ±0.15 MPa (109) for inter-shell friction of a MWNT and 0.25-0.75 MPa for crystalline graphene (197).

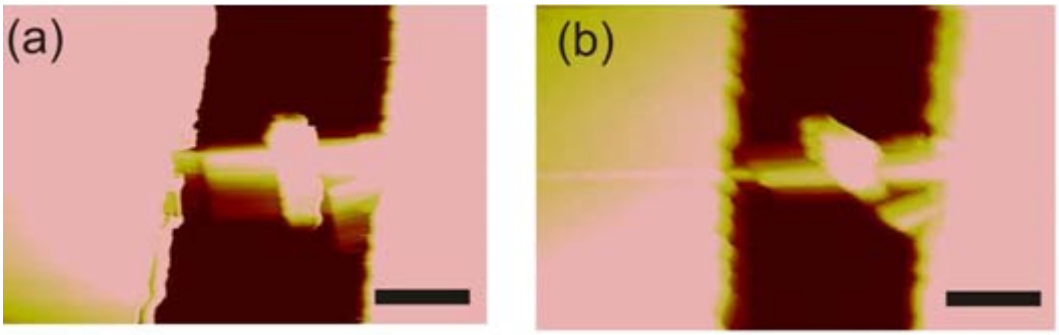

Fig. 8.10. Moving the cargo with AFM tip. (a) cargo in the initial position (b) cargo rotated after being pushed with AFM tip. The determined friction force is about 70-80 nN. Scale bar: 1 µm.

8.4 Conclusions

We assume that high friction is the main reason why the experiment was not successful. Moreover, we have no control over the chiralities of MWNTs used in the experiment, i.e. we cannot optimize the electron force induced on the motor.

Another aspect is the real magnitude of the chiral currents. According to calculations by Wang (198), the ratio of the current along the circumference and the axis is a very small constant, which depends on chiral angle and diameter. In the paper it is stated that for a nanotube with diameter of 1 nm this ratio is only 10^{-2}-10^{-3}. If this is true, the ratio is indeed too small to yield any significant effects.

Annex A: Nanofabrication

Preparing the nanotube devices is a very important, and also time-consuming, part of the experiment. That is mainly because of the small size and big sensitivity of the devices, which require a lot of attention and good optimization of the fabrication process.

The techniques used for nanofabrication are constantly changing and new methods and approaches are being developed. In this section the standard fabrication methods, such as electron beam lithography (EBL), metal evaporation and lift-off atomic force microscopy (AFM), and wet etching are presented. They were used, among the others, to fabricate devices presented in this thesis.

A.1 Substrate preparation

For fabricating nanotube devices an oxidized Si wafer, with 1 μm of SiO_2 on top is used as a substrate. Depending on application the Si layer can be highly conductive or highly resistive. If the Si layer is used as a back gate, for instance for CNT motors and low frequency resonators, it is necessary to use a conductive substrate. The wafers (Cemat Silicon S.A.) are n-doped with Ar, with resistance 0.002-0.005 Ωcm.

For high frequency carbon nanotube resonator devices the highly resistive substrate is needed. It is to avoid parasitic capacitance while applying high frequency AC signal to the device.

The wafers used for graphene fabrication require pre-determined thickness of SiO_2 (495nm), in order to be able to locate the graphene in the optical microscope.

The wafers are cut into 8x8mm chips. The first step of the fabrication is cleaning the chips in acetone and in high power ultrasonic bath. During this process all the organic contamination or dust are removed. Then the chips are rinsed in isopropanol alcohol (IPA) and dried with N_2.

A.2 Nanotube growth/deposition

In this thesis devices based on single-walled (SWNT) and multi-walled (MWNT) carbon nanotubes are presented. Depending on the type of nanotubes different procedures are applied to deposit them on a chip.

A.2.1 MWNT deposition

The MWNT are obtained from Instituto de Carboquímica, Zaragoza. The tubes are grown by means of arc discharge. The nanotubes produced by arc discharge are purer (up to about 90% pure) than those produced in the laser ablation. The principles of growth methods are presented in *Chapter 2*.

The MWNTs come in a form of a black powder. The way of depositing the nanotubes is as follows. A small amount of MWNTs is placed in dicloroethane (DCE) and in an ultrasonic bath, until a homogenous solution is achieved, typically for 30 min. A drop of the solution is then placed on the chip and spun at the rate of 600 rpm for 10 s and 1200 rpm for 15 s. This procedure is repeated for 4-5 times.

The advantage of this method is that it is fast and allows depositing big amounts of MWNTs on the substrate. The disadvantage is, however, that the location is fully random; therefore we need to locate the tubes with respect to the alignment marks. The details of locating CNTs with AFM are explained in section A.5. It is also important to notice that CNTs do not dissolve in DCE, therefore the solution is stable only for a short time.

A.2.2 SWNT growth

The SWNT are grown in the catalytic vapor deposition (CVD) process. The principles of CVD growth are presented in *Chapter 2*. First of all, the catalyst solution is prepared. It consists of 80 mg Fe, 4 mg Mo, 60 mg Au and 60 ml methanol. It is left to stir for 24 hours before the first use or placed for 30 min in ultrasonic bath before the following use.

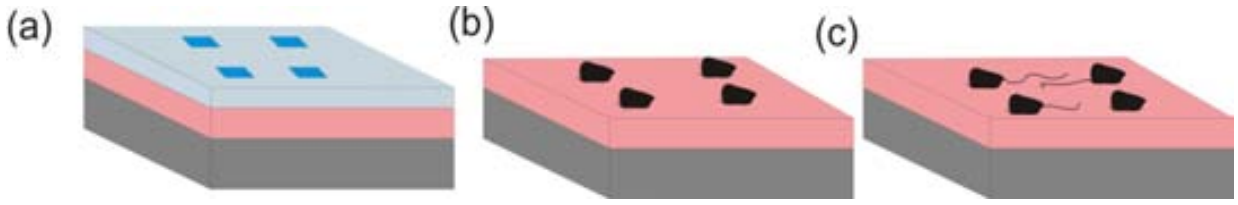

Fig. A.1. Schematics of catalyst deposition and CVD growth process. Blue, pink and grey correspond to PMMA, SiO2 and Si, respectively. (a) Openings are made in the PMMA by means of e-beam lithography. (b) Catalyst is deposited in the openings and PMMA is dissolved in DCE. (c) After CVD SWNTs have grown from the catalyst pads.

The catalyst is then deposited in specially prefabricated openings. Those openings of size 100x100 nm are made by means of electron beam lithography in PMMA 950. Then the PMMA is dissolved in DCE, leaving catalyst pads on the SiO_2 substrate. The pads are usually separated by 24 µm on the area of 200x200 µm (Fig.A.1).

The growth is then performed in the CVD oven (Fig. A.2a). First of all, the oven is purged with 500 ml/min of Ar, 500 ml/min of H_2 and 550 ml/min of CH_4 in room temperature for 10 min. Then H_2 and CH_4 flow is turned off and the chamber is heated up in Ar atmosphere. When the temperature reaches 900°C H_2 with the rate 500 ml/min is switched on to activate the catalyst. After 10 min of activation the H_2 rate is reduced to 100 ml/min and CNT synthesis is started by increasing CH_4 flow rate to 550 ml/min. The growth usually lasts 20 min. Then the CH_4 flow is turned off and the chamber is cooled down. The AFM image of SWNTs is shown in Fig. A.2b.

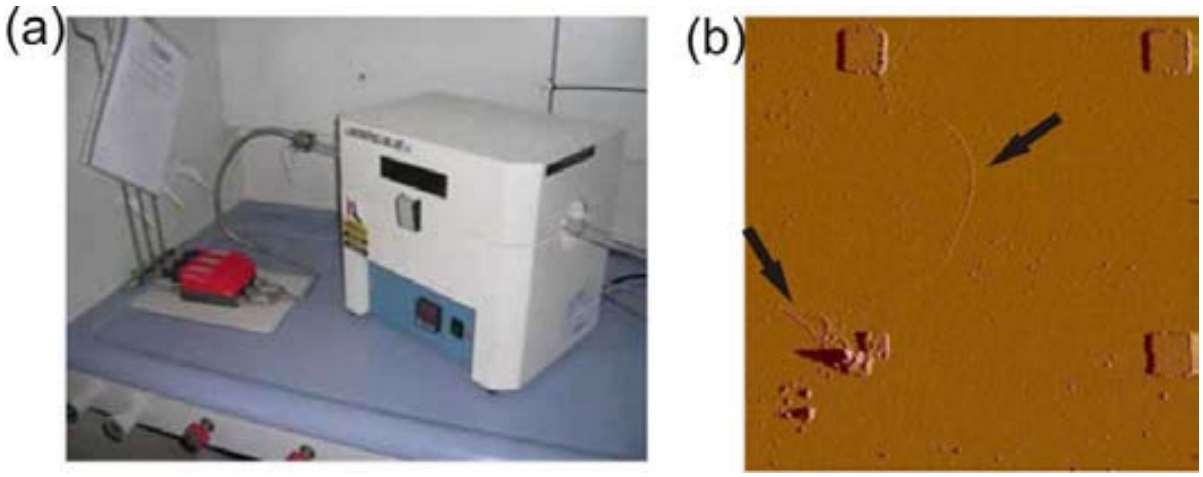

Fig. A.2. (a) CVD oven. (b) SWNTs growing from catalyst pads. AFM image of a sample with alignment marks. To minimize the slack in suspended SWNT devices it is important to choose straight sections of the tube.

A.3 Electron Beam Lithography (EBL)

Lithography is in general a process of transferring patterns from one medium to another. For many years, particle beams of various types have been used in lithography (199) (168). The most popular lithography method in silicon industry is photolithography, which employs UV light of wavelength up to 500 nm. However, with miniaturization of the devices the conventional photolithography has become increasingly inadequate. Other lithography techniques, which use different forms of radiation, including electron beams and ion beams, to offer higher resolution, are growing in importance. Also a big effort has been made with those techniques to scale lithography technology down to the nano-scale (200, 201). Nowadays EBL direct writing is one of the most common tools in nanofabrication process.

Another issue related to lithography processes is the right choice of resist. Polymethyl methacrylate (PMMA) was one of the first resists developed for EBL and remains the most commonly used positive resist. The PMMA has extremely high resolution of less than 10 nm making it perfect for nanolithography (202). It comes in powder form and is dissolved in a solvent, such as anisole or chlorobenzene, of desired concentration. The resist liquid is then spun at high speed to form a thin coating. This is followed by baking at temperatures ranging from 130°C to 170°C with a hot plate or oven to remove the casting solvent. The final resist thickness is determined by the PMMA concentration and the spin speed.

After exposing the destroyed polymer is removed, in a process called development. The typical developers used are 1:3 methyl isobutyl ketone: isopropanol (MIBK:IPA) for the highest contrast and 1:1 MIBK:IPA for the highest sensitivity (203). The developed region is then removed by rinsing in IPA.

Also negative resists are available. Those resists harden after exposure to electron beam and are not removed during the development process. Popular negative e-beam resists consist of an epoxy copolymer of glycidyl methacrylate and ethylacrylate [P(GMA-EA)], also known as COP, and a partially chloromethylated polystyrene (CMS). PMMA can also be used as a negative resist when overexposed (199).

The standard process of nanofabrication consists first of spinning two layers of poly-methyl methacrylate (PMMA) resist. First (bottom) layer is the 495K 3% in chlorobenzene and the second (top) layer is 950K 2% in chlorobenzene. Bottom layer (PMMA 495K) is more sensitive to electron beam and serves as spacer between the sample and the top layer (PMMA 950) and helps to make better lift-off. The top layer is less sensitive to the radiation and serves as an actual mask. After spinning every layer the chip is baked on the hot plate for 1 min at 150°C.

Second step is exposing the design pattern to electron beam. Electron irradiation destroys bonds of the polymer and afterwards the destroyed resist is removed in a developer (1:3 MIBK:IPA), rinsed in IPA and dried with N_2. Spin coating and EBL, shown in Fig. A.3, are done inside the cleanroom facility of Centro Nacional de Microtechnologia, Campus UAB, Bellaterra, Spain.

Fig.A.3. LEO SEM system. Cleanroom of the CNM, Bellaterra, Spain.

A.4 Metal evaporation and lift-off

The most common ways of depositing thin metal layers is by thermal evaporation or sputtering. Sputtering is not compatible with PMMA resist used for EBL, making the lift-off process difficult and not very clean.

On the contrary, thermal evaporation of metals such as Cr, Au or Al is commonly used for nanofabrication. Thermal evaporation process is typically performed in vacuum below 10^{-6} mbar. The substrate metal is placed on a boat and a substantial current (up to 100A) is passed. The substrate is heated by Joule heating up to the point that the vapor pressure becomes sufficiently high to generate a substantial flow of material from the source to the substrate surface. The other option is to heat up the metal with electron beam (so-called electron beam evaporation), which can be useful also for metals with high melting point, such as Pt.

The evaporation takes place in Edwards AUTO 306 Joule evaporator. The nanotube samples are typically covered with layers of 7 nm of Cr and 50 nm of Au. Chromium is used as an adhesion layer, since gold does not stick very well to SiO_2.

The final step is removing of the remaining resist in lift-off process. First the sample is placed in room-temperature acetone for about 30 min (alternatively, in hot acetone of 50°C) to remove the PMMA and then further 30 min in dicloroethane , which is a very strong solvent that removes the PMMA residues.

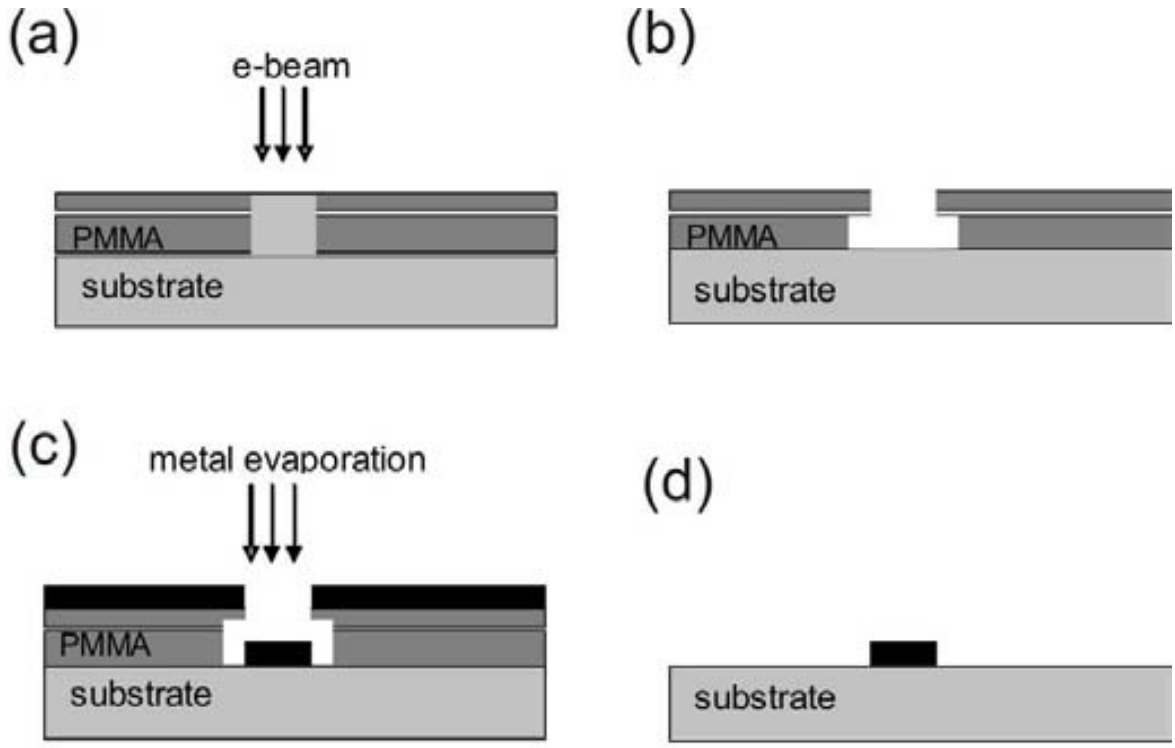

Fig. A.4. Scheme of the electron beam lithography process. (1) The substrate is covered by two layers of resist, in our case PMMA 495 and 950, and the design is exposed to the electron beam. (2) the resist destroyed by electron beam is removed in development process (3) Metal evaporation on the sample. (4) After lif-off the PMMA is removed and metal remains only on the predesigned positions.

For nanotube device fabrication there are usually two essential EBL/metal evaporation steps (Fig. A.4). In the first step the alignment marks are patterned. Those marks serve as a reference for locating the nanotubes. In the second lithography step contacts are deposited on top of the nanotubes. The contacts are designed with ELPHY program using the images of nanotubes taken with AFM microscopy, as discussed in the following section.

A.5 Atomic Force Microscopy (AFM) and device design

AFM proves to be a very useful tool for nanofabrication. It allows to image features with nanometer resolution. Also the tapping mode is non-invasive, in contrast to SEM imaging which can affect CNTs. It is convenient to take images with AFM after every fabrication step.

First of all, the AFM is used to locate the nanotubes with respect to alignment marks. This approach is rather time consuming, but allows choosing for further fabrication the nanotubes with desired length and diameter. Then, after locating the tubes with respect to the markers one can proceed to design contacts, which would serve as source, drain and side-gate for the device.

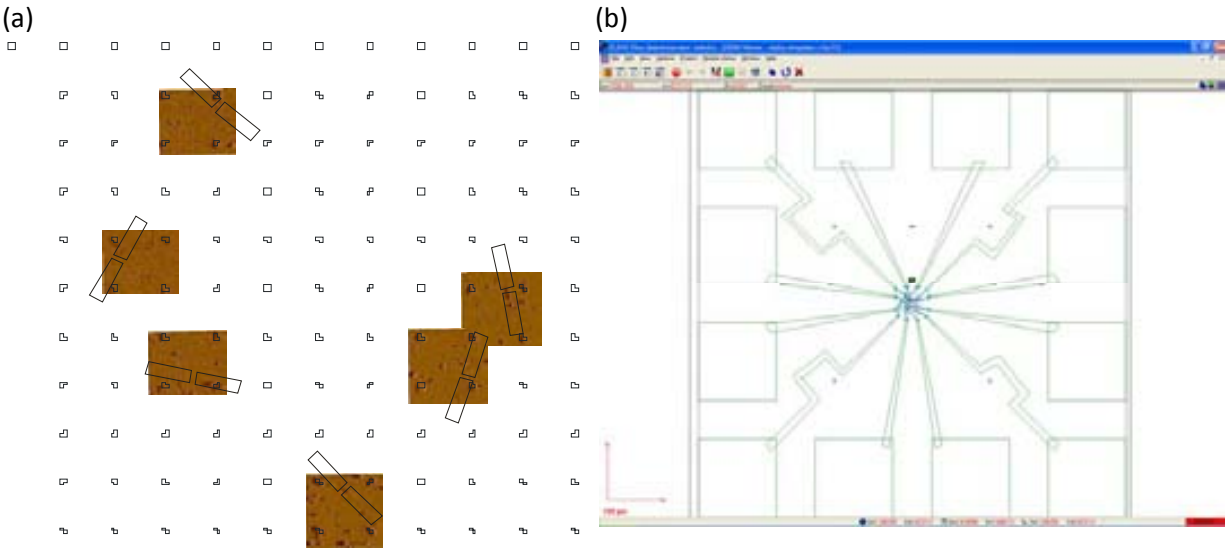

Fig. A.5. (a) CorelDraw mark pattern with some AFM images of MWNTs and designed contacts. (b) Elphy design of the contacts. The design is then exposed on the samples.

The AFM image is imported into CorelDraw file, where it is aligned with respect to the markers and the contacts are designed (Fig. A.5a). Then the design is imported in ELPHY program, used in the EBL system (Fig. A.5b). Contacts are fabricated with EBL/evaporation standard procedure, as described before (Fig. A.6).

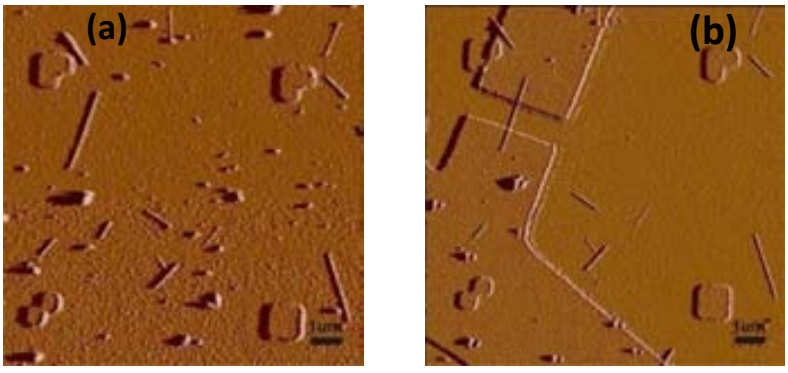

Fig. A.6. (a) AFM image of a MWNT located with respect to alignment marks. (b) The same MWNT with Cr/ Au contacts made by means of EBL and metal evaporation.

A.6 Electrical measurements and etching

Before proceeding with the sample one has to measure the contact resistance of the devices. Since the CNTs can be either metallic or semiconducting the values of resistances can vary from 10 kΩ to various MΩ.

After measuring the electrical properties of the device the last step, etching, is performed. There are various etching techniques commonly used in semiconductor research and industry. In the past years the CMOS investigation has led to discovery and optimization of silicon and silicon dioxide etching processes, which can now be adapted for nanofabrication. In principle we divide them into dry etching and wet etching techniques. Dry etching consists of plasma-based and ion-beam etching techniques. Even though those techniques tend to have better lateral resolution and depth control they are not universally compatible with carbon-based materials used for nanofabrication. They can cause substrate damage when high velocity ions hit the surface. This is very important while working with organic and carbon materials or two-dimensional electron gasses confined to the surface. For instance a common form of plasma etching is used to shape or remove graphene structures.

Therefore, for CNT device fabrication wet etching processes are used. The main advantage of this method is that using different masks and etchants high selectivity can be achieved. Also the buffered hydrofluoric acid (HF) that is used to remove SiO_2 does not influence neither the structure of a CNT, nor the Au contacts (168).

The main disadvantage of wet etching is poor lateral resolution (1-0.1 μm) and difficult control of vertical etching. The etching rate is affected by the exposure to air or simply changes with time. The typical rate for the SiOEtch 5%, BASF, etchant used for the nanofabrication is 100 nm/min (168).

The etching time depends on the device and its application. For 100 nm long resonators it is enough to etch 100 nm, not to induce too much tension in the device. For longer resonators (MWNT) the etching time is typically 3 min, resulting in 300nm of removed SiO2. Also for the CNT motor with cargo it is important to etch enough SiO_2 to let the cargo rotate freely (normally 350-400 nm).

After the etching the sample is transferred into de-ionized water to remove rests of HF acid and then into IPA. Finally, it is gently dried in boiling IPA. The drying step is critical for the sample, as the tube has a tendency to collapse due to surface tension. The alternative to hot IPA drying is the critical point drying (CPD). Both of the methods reduce surface tension while drying, enabling to obtain a suspended device. However hot IPA method is much faster compared to the critical point drying and it also enables to avoid contamination related to CPD. Also it is important that the CNT between the contacts is completely straight, to avoid slack or sticking to the surface during drying.

The etching is performed either in the cleanroom of CNM or the cleanroom of the Universidad Autonoma de Barcelona.

A.7 Annealing

An optional treatment to improve the contact resistance of the devices is to anneal the sample in 300°C in Ar and H_2 atmosphere (500 ml/min and 100 ml/min, respectively) for at least one hour. This is supposed to improve the adhesion between the nanotube and metal layer and leading to improvement of device resistance. Also the presence of H_2 reduces the organic contamination on the surface of nanotube, such as rests of PMMA. The improvement in the resistance can be up to 100 times, depending on the device.

A.8 Electrical breakdown technique

An important step in nanomotor fabrication consists of applying electrical breakdown technique to remove the outer shells of a multiwall nanotube (109, 141). Carbon nanotubes can withstand remarkable current densities, exceeding 10^9 A/cm^2, in part due to their strong carbon-carbon bonding. However, at high enough currents nanotubes ultimately fail (Fig. A.7). In MWNTs, this failure occurs in air at a certain threshold power through the rapid oxidation of the outermost carbon shell. Because the oxidation of defect-free graphite can proceed only at extremely high temperatures, it was concluded that the primary factor in the breakdown initiation was current-induced defect formation and that self-heating plays only a secondary role (141).

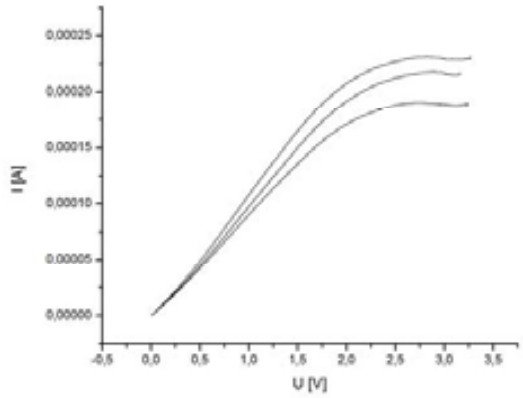

Fig. A.7. I-V characteristic of burning shells of the individual MWNT. Three shells have been removed in total. By characterizing the MWNT after every shell loss one can determine the contribution of each shell to the I-V. Each shell typically carries 19 µA of current.

Electrically, the breakdown of a single carbon shell results in a partial conductance drop that typically occurs within a few milliseconds. When stressed at sufficiently high bias, multiple independent drops occur as one carbon shell after another is broken.

If a device consists of a MWNT with a golden plate deposited on top the ablation will occur only on the part of the nanotube that is not covered with gold, because the metal plate efficiently absorbs the heat generated in this portion of the tube, which prevents or at least delays the tube oxidation in this part (114).

While removing the shells the resistance of the device is increasing and the diameter is decreasing. Typically one shell carries 19uA of current (141). For this reason is important to start with devices with good contact resistance, in order of a few tens of kΩ.

Annex B: Mixing technique

B.1 Actuation and detection

One of the ways of indirectly measuring a high-frequency response can be through signal mixing. Since a high-frequency signal can easily be converted into a low-frequency signal, it is a common technique used in high-frequency instruments, such as CNT transistors and resonators (84, 92). Mixing allows the frequency of any signal to be varied without losing information about its amplitude, which simplifies the detection.

The measurement scheme is presented in Fig. B.1. We apply a frequency modulated signal to the source electrode with the form of:

$$V^{FM}(t) = V^{AC}\cos(2\pi ft + (f_\Delta / f_L)\sin(2\pi f_L t)), \qquad (1)$$

where f is the carrier frequency, f_Δ the frequency deviation, t the time, and f_L a low frequency, typically 671 Hz. The high frequency signal comes from RF source (Agilent Technologies E8257D) and low frequency from the lock-in amplifier (Stanford Research Systems SR830 DSP). Both high and low frequency signals are applied on the source, but only the low-frequency signal from the drain electrode is measured by the current input of the lock-in.

The resulting mixing current, measured on the drain, is given by:

$$I_{mix} = \frac{1}{2}\cdot\frac{dG}{dV_g^{DC}}\cdot V_g^{DC}\cdot\frac{C'}{C}\cdot V^{AC}\cdot f_\Delta\cdot\frac{\partial}{\partial f}\mathrm{Re}[x_0] \qquad (2)$$

with G the conductance of the device, $\mathrm{Re}[x_0]$ the real part of its oscillation amplitude and *C* is the nanotube-gate capacitance (84).

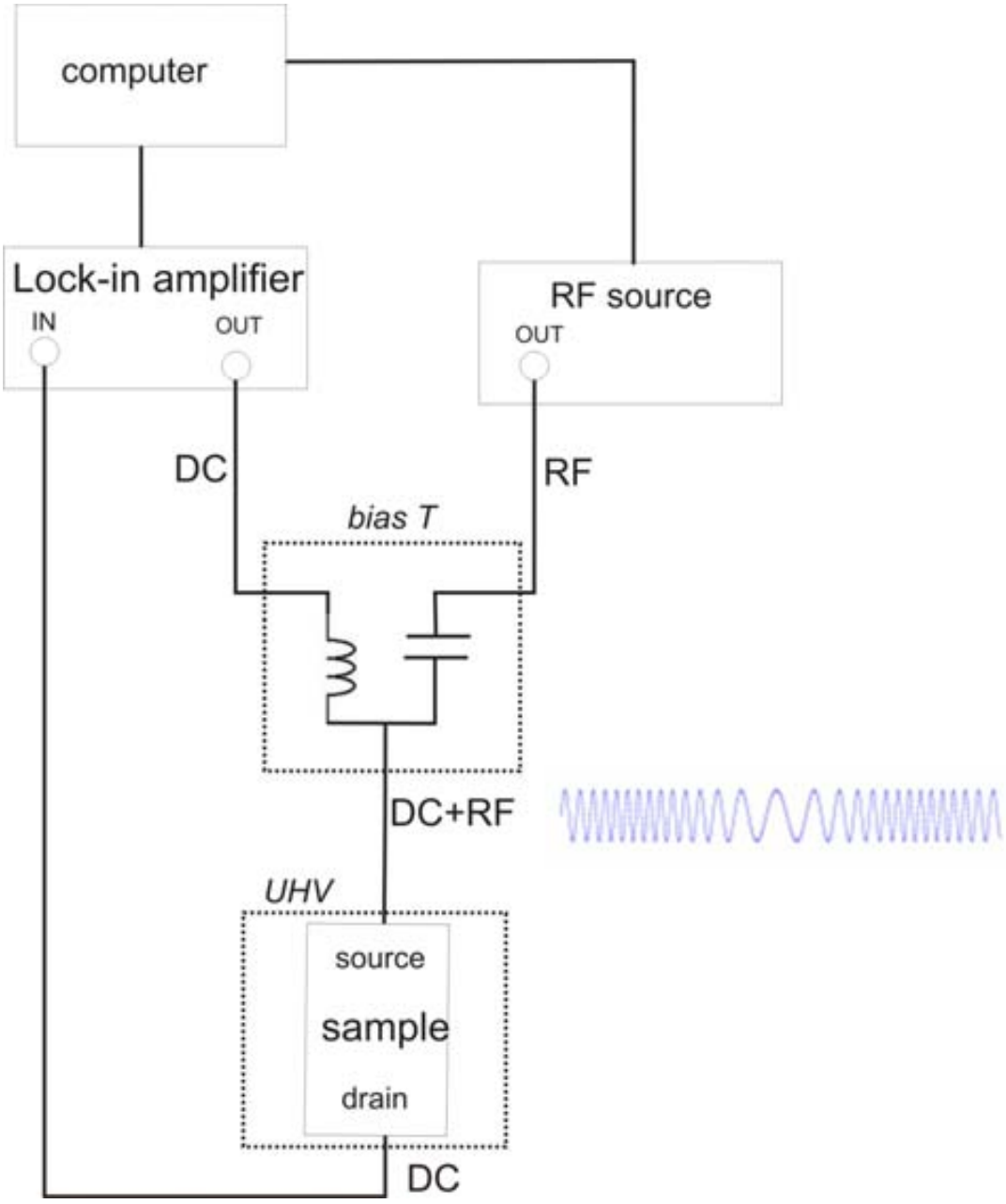

Fig. B.1. Schematic of FM modulated measurement setup.

To detect the motion of the nanotube on resonance we rely on the transistor properties of carbon nanotubes. For semiconducting (4) and small band-gap semiconducting CNTs (17, 204) the conductance depends on the induced charge on the tube. A modulation in charge leads to a modulation in the CNT's conductance. The conductance can be modulated by changing either the applied gate voltage or capacitance to the gate (84).

We measure the module of the mixing current with a lock-in amplifier at frequency f_L, and the measurement yields $I_{mix} \propto \left| \partial / \partial f \, \mathrm{Re}[x_0] \right|$.

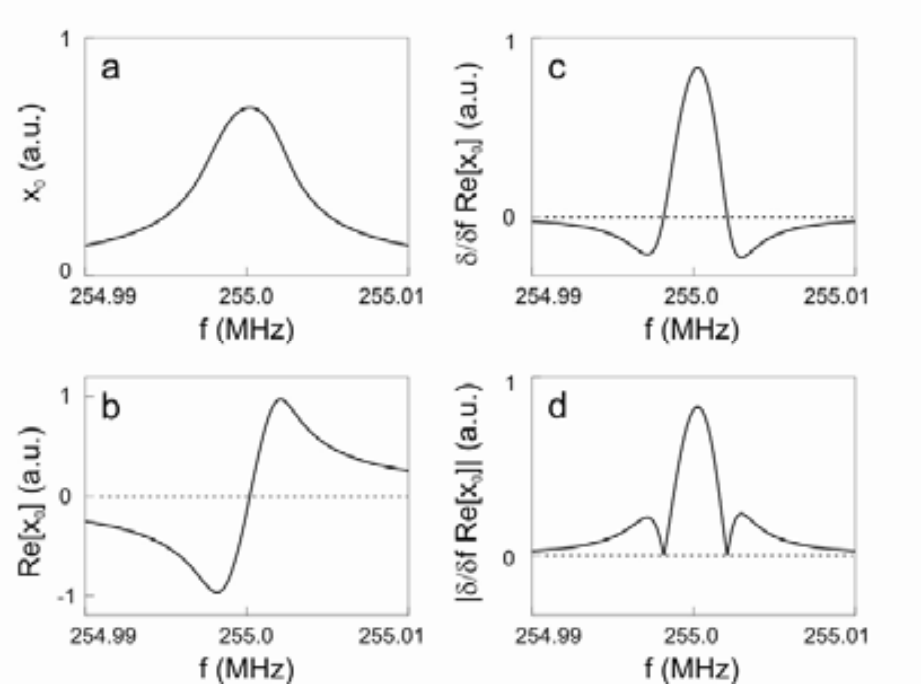

Fig. B.2. Calculated examples of a the motion amplitude x_0, b its real part $\mathrm{Re}[x_0]$, c $\partial / \partial f \, \mathrm{Re}[x_0]$, and d $\left| \partial / \partial f \, \mathrm{Re}[x_0] \right|$. Adapted from (92).

Fig. 2 presents calculated examples of the motion amplitude x_0, its real part $\mathrm{Re}[x_0]$, $\partial / \partial f \, \mathrm{Re}[x_0]$, and $\left| \partial / \partial f \, \mathrm{Re}[x_0] \right|$. The two minima in $\left| \partial / \partial f \, \mathrm{Re}[x_0] \right|$ (Fig. B.2d) provide a precise and simple way to extract the resonance width, and therefore the quality factor.

An important factor in FM measurements is choosing the right value for the frequency deviation (f_Δ). The f_Δ has to be sufficiently small compared to the width of the mechanical resonance Δf . Otherwise, the measured resonance broadens because the frequency range probed by the FM driving force is too large. The typical values of f_Δ used in the experiments were 50-200 kHz.

B.2 Resonance width and quality factor with the FM technique

In physics and engineering the quality factor or Q factor is a dimensionless parameter which characterizes a resonator's bandwidth relative to its center frequency. Higher *Q* indicates a lower rate of energy loss relative to the stored energy of the oscillator.

The mixing current as a function of driving frequency f has a characteristic resonance line-shape with the resonance peak at frequency f_0 flanked by two minima. For a linear resonator the separation between the latter, Δf , coincides with the mechanical bandwidth defined as full width at half maximum (FWHM) for the squared modulus of the motional amplitude (time-averaged mechanical energy stored) and allows to extract the quality factor Q in a simple manner from the relation $\Delta f = f_0 / Q$.

Annex C: Dynamics of a system with one degree of freedom

The calculations are based on the ref. (168).

C.1 Dynamics of a system with infinite degrees of freedom

The simplest dynamic system with one degree of freedom is the harmonic oscillator, which can be modeled as a mass attached to an elastic spring which obeys Hooke's law. The force of the spring $F_s$varies linearly with the displacement x. The constant of proportionality for the spring is the modulus *k.*

$$F_s = -kx \qquad \text{(C.1)}$$

Using Newton's second law of motion, the equation of motion for any displacement x is

$$\sum F = m\ddot{x} \qquad \text{(C.2)}$$

which can be written as a linear second-order differential equation

$$mx + k\ddot{x} = 0 \qquad \text{(C.3)}$$

The general solution to the differential equation is then

$$x(t) = A\exp(-i\omega_m t + -\varphi) \qquad \text{(C.4)}$$

in which $\omega_m = \sqrt{\frac{k}{m}}$is the resonance frequency of the one-dimensional system and A and φ are constants which represent the amplitude and the phase of the movement respectively.

It is rather challenging to find analytical solutions to the dynamics of continuum systems with arbitrary geometries; as a matter of fact, in most cases a numeric approach is required. Nevertheless, it is possible to find solutions to simple geometries like beams.

C.2 Flexural vibrations of a beam

A beam can be considered as a solid which can vibrate only in one direction and has a constant cross-section over its length. Carbon nanotubes and most grapheme resonators can be well treated as beams. In Fig. C.1, the schematic of a vibrating beam in direction z is shown.

In order to solve the equation of the motion of the beam we assume that the strain and the displacements are small. In this approximation the displacement has to be smaller than the thickness of the beam, or the diameter, in the case of a circular cross-section.

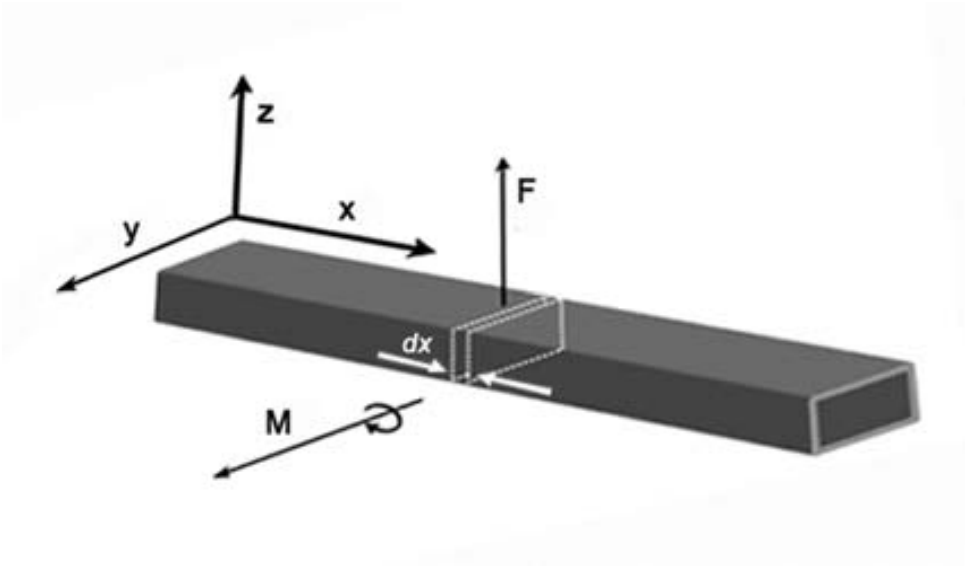

Fig. C.1. Beam of length l and cross-section A. The transverse displacement $z(x)$is the result of forces F along z and torques M along y. The beam is considered to vibrate only in the direction$z$.

As shown in Fig. C.1, a differential element of length $\mathrm{d}x$, cross-section A and bending moment l_y is considered. Note that only displacements in the direction z are considered. This element is subject to forces $F_z(x + \mathrm{d}x)$ and $-F_z(x)$. This element is also subjected to torques $M_y(x + \mathrm{d}x)$ and $-M_y(x)$. Balancing the forces

$$F_z(x + \mathrm{d}x) - F_z(x) - \rho A dx \frac{\partial^2 x}{\partial t^2} = 0 \qquad \text{(C.5)}$$

and balancing the torques

$$F_z(x + \mathrm{d}x)\mathrm{d}x + M_y(x + \mathrm{d}x) - M_y(x) = 0 \qquad \text{(C.6)}$$

thus

$$\frac{\partial F_z(x)}{\partial x} = \rho A \frac{\partial^2 x(z)}{\partial t^2} \qquad \text{(C.7)}$$

$$F_z(x) = -\frac{\partial M_y}{\partial x} \qquad \text{(C.8)}$$

in which

$$M_y = E l_y \frac{\partial^2 x(z)}{\partial x^2} \qquad \text{(C.9)}$$

These equations yield the result

$$\frac{\partial^2}{\partial x^2}\left(E l_y \frac{\partial^2 z(x)}{\partial x^2}\right) = -\rho A \frac{\partial^2 z(x)}{\partial t^2} \qquad \text{(C.10)}$$

and for l_y constant along the beam

$$El_y \frac{\partial^2 z(x)}{\partial x^2} = -\rho A \frac{\partial^2 z(x)}{\partial t^2} \qquad \text{(C.11)}$$

This is the equation which drives the movement of a beam for small displacements and strain. We can assume harmonic time dependence

$$z(x,t) = z(x)e^{-i\omega t} \qquad \text{(C.12)}$$

where the spatial dependence should satisfy

$$\frac{d^4 z}{dx^4} = \omega^2 z(x) \frac{\rho A}{E I_y} \qquad \text{(C.13)}$$

If we define

$$\beta = \sqrt{\omega} \left(\frac{\rho A}{E I_y}\right)^{\frac{1}{4}} \qquad \text{(C.14)}$$

the general solution will be

$$z(x) = c_1 \cos(\beta z) + c_2 \sin(\beta z) + c_3 \cosh(\beta z) + c_4 \sinh(\beta z) \qquad \text{(C.15)}$$

Considering that the beam has a length l and that it is clamped at both ends, which is the most common configuration for carbon nanotube and graphene resonators, the displacement and the slope at both ends will be zero:

$$z(0) = z(l) = \left.\frac{dz(x)}{dx}\right|_{x=0} = \left.\frac{dz(x)}{dx}\right|_{x=l} = 0 \qquad \text{(C.16)}$$

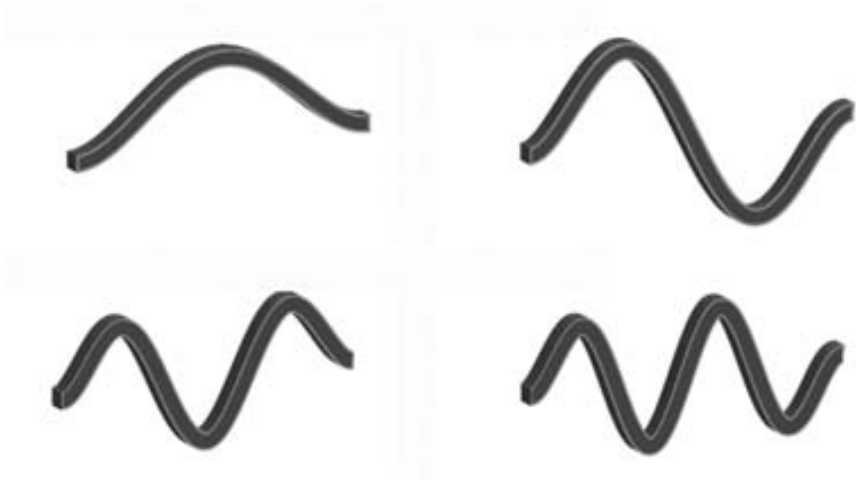

Fig. C.2. First four eigenmodes for the equation of a doubly clamped beam with no residual tension.

With these boundary conditions, only a discrete set of β_n is allowed, and it has to satisfy the equation

$$\cos(\beta_n l)\cosh(\beta_n l) - 1 = 0 \qquad \text{(C.17)}$$

This equation can only be solved numerically. The first solutions for β_n are $\beta_0 l = 0$, $\beta_1 l = 4.73004$, $\beta_2 l = 7.8532$, $\beta_3 l = 10.9956$, $\beta_4 l = 14.1372$, etc. Note that the solution β_0 is the solution for an immobile beam.

The displacement is then given by

$$z_n(x) = a_n(\cos(\beta_n z) - \sin(\beta_n z)) + b_n(\cosh(\beta_n z - \sinh(\beta_n z)) \qquad \text{(C.18)}$$

where the ratio a_n/b_n takes the values $a_1/b_1 = -1.01781$, $a_2/b_2 = -0.9923$, $a_3/b_3 = -1.0000$, etc. and the eigenvalues are given by:

$$\omega_n = \sqrt{\frac{EI_y}{\rho A}}\beta_n^2 \qquad \text{(C.19)}$$

In these equations $z_n(x)$ and $\beta_n(x)$ are the eigenmodes and the eigenfrequencies for the doubly clamped beam. In Fig. C.2 the spatial distribution of the first four eigenmodes is shown.

Publications

1. *High-frequency nanotube mechanical resonators*
J. Chaste, M. Sledzinska, M. Zdrojek, J. Moser, and A. Bachtold
APPLIED PHYSICS LETTERS 99, 213502 (2011)

Conferences

1. Invited talk: *Carbon Nanotube Resonators*; Instituto Politécnico Nacional, Escuela Superior de Física y Matemáticas, Mexico City, 2011

2. NanoSpain 2011, Bilbao, Spain (poster Gold and Silicon Heaters for nanotube motors)
3. NanoSpain 2010, Malaga, Spain (poster Electron Windmill)
4. GDRE 2009, Castelldefels, Spain (poster Electron Windmill)
5. Summer School in Nanoelectronics, Bad Herrenalb, Germany 2009 (poster Electron Windmill)

Carbon Nanotube Electron Windmill

M. Sledzinska, A. Barreiro, A. Bachtold
CIN2-Instituto Catalán de Nanotecnología, Universidad Autónoma de Barcelona (Spain).

Abstract: Recently, a new mechanism to drive a nanotube rotor has been proposed by Bailey, Amanatidis, and Lambert (PRL **100**, 256802 (2008)). It is based upon the torque generated by a flux of electrons passing through a chiral tube. Here we present our progress in the fabrication of those so-called nanotube windmills. Devices consist of a suspended multi-wall nanotube, contacted to two gold electrodes. A few outer shells are removed in between the electrodes, leaving the inner tube free to rotate. When passing a current through the devices electrons are forced to tunnel from the outer onto the inner shells. Due to angular momentum conservation, a tangential force is produced that causes the inner tube to rotate.

Idea: chiral currents in CNTs

v_x - velocity component along the circumference

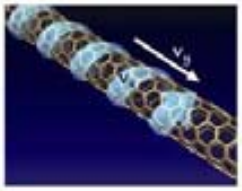

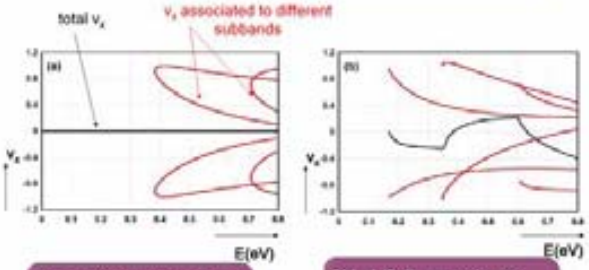

Achiral (8,8) nanotube -> no effective chiral current

Chiral (8,4) nanotube -> effective chiral current changes sign!

C.J. Lambert *& al.*
Phys. Rev. B **78**, 233405 (2008)

Device: CNT windmill

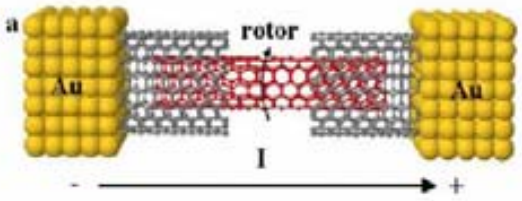

Inner tube free to rotate!

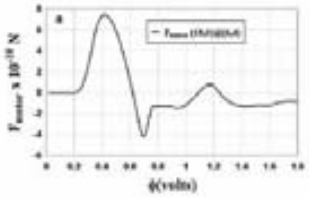

Tangential force and associated torque cause the inner tube to rotate

S.W.D. Bailey *& al.*
Phys. Rev. Lett. **100**, 256802 (2008)

Sample preparation: contacts

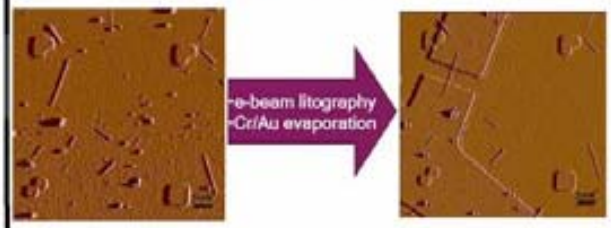

Localizing MWNTs with AFM

Contacted MWNT

Burning shells & patterning plate

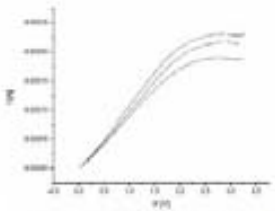

•B. Bourlon *& al.*
Phys. Rev. Lett. **92**, 026804 (2004)
•A. Barreiro *& al.*
Science **320**, 775 (2008)

Contacted MWNT with a gold plate

Experiment

Suspended device

Connecting the nanotube in the SEM

Passing the current through the suspended device while imaging

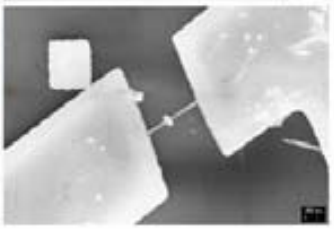

Gold and Silicon Microheaters for Nanotube and Graphene Applications

Marianna Sledzinska, Neus Sabate**, Marc Salleras**, Pablo Jimenez***, Ana Benito***, Wolfgang Maser***, Adrian Bachtold**

ICN, CIN2, Barcelona, UAB (Spain).
**Centro Nacional de Microelectrónica (CNM), Campus Universidad Autónoma de Barcelona. 08193 Bellaterra (Barcelona), Spain
***Instituto de Carboquímica de Zaragoza (CSIC), Departamento de Nanotecnologia, Zaragoza, Spain

Abstract: We present progress in the fabrication of microheaters, designed for possible applications with carbon-based nanomaterials, such as carbon nanotubes (CNTs) and graphene. The first type of heaters we fabricate, which we call gold heaters, consist of a thin gold layer on a suspended, non-conductive silicon beam. Joule heating is induced upon passing large currents. The other type of heaters, which we call silicon heaters, consist of a highly doped silicon beam covered by an insulating layer of oxide and a thin platinum layer. High current is passed through the silicon to induce heating. The temperature is measured by probing the resistance of the platinum. Using the microheaters it is possible to introduce controlled temperature gradients in suspended CNTs or graphene. This will be useful for various applications, for instance in nanoelectromecanical systems (NEMS), where thermal gradients can induce motion of nanoscale cargos. The heaters could also be used to study heat transport and dissipation.

Gold heater

The heater: 70nm Au layer on suspended 350nm Si beam

We use the Au layer for two purposes:
- **heater** - while passing high current we observe the heating of the central part
- **sensor** - By measuring change of resistance vs. temperature R(T) we can estimate the average temperature of the device

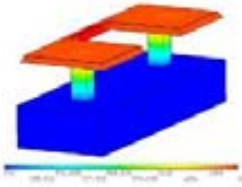

ANSYS model of a suspended gold heater. The maximum temperature can reach up to 1200C.

Advantage: easy fabrication process

Drawback: the maximum temperature is limited due to a limit on the maximum current density flowing through the thin gold layer

1. Fabrication
(100) SOI wafer with 350nm top Si layer

- Electron beam lithography (EBL)
- Cr/Au thermal evaporation on silicon + lift-off
- Annealing at 300C in Ar/H_2 atmosphere

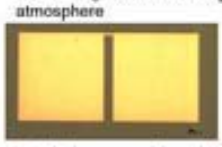

Optical microscope of the gold heater before suspension.

2. Wet etching
- KOH
- HF 49%
- Critical point drying

SEM image of the gold heater after suspension.

Joule heating of a gold heater - experiment

1. Calibration: Measuring R as a function of T in an oven

2. Experiment: Joule heating of Au layer. Measurements in 10^{-4} vacuum, room temperature

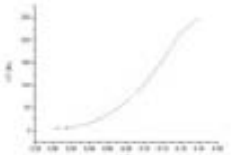

Measured average temperature of the gold heater vs. current

Highest average temperature of the heater obtained in measurements: 435C

Temperature in the middle of the heater: 650C

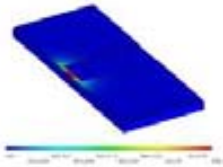

ANSYS calculation of temperature distribution in the gold heater

Silicon heater

Advantage: possibility of reaching high temperatures

Drawback: complicated and time-consuming fabrication process

Device consists of two circuits:
- **Silicon heating circuit**
- **Platinum temperature sensing circuit**

1. Fabrication:
(100) SOI wafer, with highly doped (10^{19}-$10^{20}cm^{-3}$) Si layer

- EBL + SiO_2 etching - heating circuit
- EBL - Pt sensor
- Cr/Pt evaporation + lift off
- EBL - connection between heating and sensing circuit
- Cr/Au evaporation + lift-off

2. Wet etching:
- SiOetch
- KOH
- solution to remove Au layer

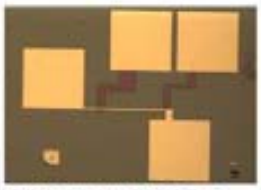

Optical microscope of the silicon heater after suspension.

SEM image of the silicon heater after suspension.

Idea: phonon induced movement

Temperature gradient leads to phonon current, moving from hot to cold, which can drag a cargo along the carbon nanotube.

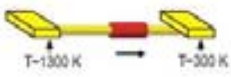

A. Barreiro *& al.* *Science* ***320, 775 (2008);***

1. Fabrication
- MWNT deposition on chips with marks
- MWNT localization with AFM
- EBL - heaters
- Cr/Au evaporation

Optical microscope image of the nanotube motor. Inset: AFM image of nanotube with cargo.

2. Wet etching
- KOH
- HF 49%
- Critical point drying

SEM image of the nanotube motor.

Future: measurements of the motor

Other possible applications: heat transport and dissipation in nanotubes and graphene

Bibliography

1. [Online] http://www.stealth.com/faq_technology.htm.

2. **P. Avouris, Z. Chen and V. Perebeinos.** 2007, Nature Nano., Vol. 2, p. 605.

3. **P. Avouris, J. Appenzeller, R. Martel and S. J. Wind.** 2003, Proceeding of the IEEE, Vol. 91, p. 1772.

4. **S. J. Tans, A. R. M. Verscheueren, C. Dekker.** 1998, Nature, Vol. 393, p. 49.

5. **R. Martel, T. Schmidt, H. R. Shea, T. Hertel, P. Avouris.** 1998, Appl. Phys. Lett., Vol. 73, p. 2447.

6. **S. Heinze, J. Tersoff*, R. Martel, V. Derycke, J. Appenzeller, and Ph. Avouris.** 2002, Phys. Rev. Lett., Vol. 89, p. 106801.

7. **S. J. Wind, J. Appenzeller, R. Martel, V. Derycke, P. Avouris.** 2002, Appl. Phys. Lett., Vol. 80, p. 3817.

8. **P. Avouris.** 2002, Chem. Phys., Vol. 281, p. 429.

9. **A. Javey, H. Kim, M. Brink, Q. Wang, A. Ural, J. Guo, P. McIntyre, P. McEuen, M. Lundstrom and H. Dai.** 2002, Nature Mat., Vol. 1, p. 241.

10. **X.Liu, C. Lee, C. Zhou, C. and J. Han.** 2001, Appl. Phys. Lett., Vol. 79, p. 3329.

11. **A. Bachtold, P. Hadley, T.Nakanishi and C. Dekker.** 2001, Science, Vol. 294, p. 1317.

12. **V. Derycke, R. Martel, J. Appenzeller and P. Avouris.** 2001, Nano. Lett., Vol. 1, p. 453.

13. **Z. Chen, J. Appenzeller, Y.-M. Lin, J. Sippel-Oakley, A. G. Rinzler, J. Tang, Sh. J. Wind, P. M. Solomon and P. Avouris.** 2006, Science, Vol. 311, p. 1735.

14. **J. Kong, N. R. Franklin, C. Zhou, M. G. Chapline, S. Peng, K. Cho, H. Dai.** 2000, Science, Vol. 287, p. 622.

15. **V. Derycke, R. Martel, J. Appenzeller, P. Avouris.** 2002, Appl. Phys. Lett., Vol. 80, p. 2773.

16. **M. Bockrath, J. Hone, A. Zettl, P. L. McEuen, A. G. Rinzler, R. E. Smalley.** 2000, Phys. Rev. B, Vol. 61, p. 1060.

17. **C. Zhou, J. Kong, E. Yenilmez, H. Dai.** 200, Science, Vol. 290, p. 1552.

18. **A.P. Graham, G.S. Duesberg, W. Hoenlein, F. Kreupl, M. Liebau, R. Martin, B.Rajasekharan, W. Pamler, R. Seidel, W. Steinhoegl, E. Unger.** 2005, Appl. Phys. A, Vol. 80, p. 1141.

19. **J. A. Misewich, R. Martel, Ph. Avouris, J. C. Tsang, S. Heinze and J. Tersoff.** 2003, Science, Vol. 300, p. 783.

20. **M. Freitag, J. Chen, J. Tersoff, J. C. Tsang, Q. Fu, J. Liu, and Ph. Avouris.** 2004, Phys. Rev. Lett, Vol. 93, p. 076803.

21. **M. Freitag, J. C. Tsang, J. Kirtley, A. Carlsen, J. Chen, A. Troeman, H. Hilgenkamp, and Ph. Avouris.** 2006, Nano. Lett., Vol. 6, p. 1425.

22. **M. Freitag, Y. Martin, J. A. Misewich, R. Martel, and Ph. Avouris.** 2003, Nano. Lett., Vol. 3, p. 1067.

23. **K. Balasubramanian, Yuwei Fan, Marko Burghard, and Klaus Ker.** 2004, Appl. Phys. Lett., Vol. 84, p. 2400.

24. **M. Freitag, James C. Tsang, Ageeth Bol, Dongning Yuan, Jie Liu, and Phaedon Avouris.** 2007, Nano. Lett., Vol. 7, p. 2037.

25. **M. Freitag, James C. Tsang, Ageeth Bol, Phaedon Avouris, Dongning Yuan, and Jie Liu.** 2007, Appl. Phys. Lett, Vol. 91, p. 031101.

26. **Iijima, S.** 1991, Nature, Vol. 354, p. 56.

27. **Pan, Z., S.S. Xie, B. Chang, C. Wang.** 1998, Nature, Vol. 394, p. 631.

28. **Dresselhaus, M. S, P. C. Eklund.** 2000, Adv. in Phys, Vol. 49, p. 706814.

29. [Online] http://students.chem.tue.nl.

30. [Online] http://nlpgw.jst.go.jp/images/.

31. **Dresselhaus, M.S., G. Dresselhaus, R. Saito, A. Jorio.** 2005, Phys. Rep., Vol. 409, p. 47.

32. **Charlier, J.-C., X. Blasé, S. Roche.** 2007, Rev. Mod. Phys., Vol. 79, p. 677.

33. **Saito, R., G. Dresselhaus, M. S. Dresselhaus.** *Physical Properties of Carbon Nanotubes.* London : Imperial College Press, 1998.

34. **McEuen, P. L., M. Fuhrer, H. Park.** 1, 2002, IEEE Trans. on Nanotech., p. 78.

35. **Mintimre, J., C. T. White.** 1998, App. Phys. A, Vol. 67, p. 15037.

36. **Charlier, J.-C. , P. Lambin.** 1998, Phys. Rev. B, Vol. 57, p. 15037.

37. **Kramberger, C., R. Pfeiffer, H. Kuzmany, V. Zolyomi, J. Kürti.** 2003, Phys. Rev. B, Vol. 68, p. 235404.

38. **Thomsen, C., S. Reich.** 2000, Phys. Rev. Lett, Vol. 85, p. 5214.

39. **Zolyomi, V., J. Kürti.** 2002, Phys. Rev. B, Vol. 66, p. 073418.

40. **Tuinstra, F., J. L. Koenig.** 1970, J. Chem. Phys., Vol. 53, p. 1126.

41. **Nemanich, R. J., S. A. Solin.** 1979, Phys. Rev. B, Vol. 20, p. 392.

42. **Poot, M., H. S. J. van der Zaant.** 2011, arXiv: 1106.2060v1.

43. **Yu, M. F. et al.** 2000, Science, Vol. 287, p. 637.

44. **Yu, M. F., Files, B. S., Arepalli, S. & Ruoff, R. S.** 2000, Phys. Rev. Lett., Vol. 84, p. 5552.

45. **Zettl, J. and A. Cumings.** 2000, Science, Vol. 289, p. 602.

46. **Pantano, A., David M.Parks, Mary C.Boyce.** 2004, Journal of the Mechanics and Physics of Solids, Vol. 52, p. 789.

47. **Journet, C., W. K. Maser, P. Bernier, A. Loiseau, M. Lamy de la Chapelle, S. Lefrant, P.Deniard, R. Lee, J.E. Fischer.** 1997, ature, Vol. 388, p. 756.

48. **Maser, W.K., E. Muñoz, A.M. Benito, M.T. Martinez, G.F De La Fuente, Y. Maniette, E. Anglaret, J.L. Suavajol.** 1998, Appl. Phys. Lett., Vol. 292, p. 587.

49. **Scott, C.D., S. Arepalli, P. Nikolaev, R.E. Smalley.** 2001, Appl. Phys. A, Vol. 72, p. 573.

50. **Jones, K. M., and M. J. Heben.** 2005, Chem. Phys. Lett., Vol. 401, p. 522.

51. **Guo, T., P. Nikolaev, A. Thess, D. T. Colbert, R. E. Smalley.** 1995, Chem. Phys. Lett., Vol. 243, p. 49.

52. **Jost, O., A.A. Gorbunov, W. Pompe, T. Pichler, R. Friedlein, M. Knupfer, M. Reibold, H.-D. Bauer, L. Dunsch, M.S. Golden, J. Fink.** 1999, Appl. Phys. Lett., Vol. 75, p. 2217.

53. **Kumar, M., Ando, Y.** 2010, Journal of Nanoscience and Nanotechnology, Vol. 10, p. 3739.

54. **Barreiro, A.** *Carbon Nanoelectronics. PhD thesis.* Bellaterra : Universidad Autonoma de Barcelona, 2008.

55. **Kong, J. , H.T. Soh, A.M. Cassell, C.F. Quate, H.J Dai.** 1998, Nature, Vol. 395, p. 878.

56. **Zhou, W., Z. Han, J. Wang, Y. Zhang, Z. Jin, X. Sun, C. Yan, Y. Li.** 2006, Nano.Lett., Vol. 6, p. 2987.

57. **Gohier, A., C.P. Ewels, T.M Minea, M.A. Djouadi,.** 2008, Carbon, Vol. 46, p. 1331.

58. **Cui, H., G. Eres, J.Y. Howe, A. Puretzky, M. Varela, D.B. Geohegan, D.H Lowndes.** 2003, Chem. Phys. Lett., Vol. 374, p. 222.

59. **Fan, S.S., M.G. Chapline, N.R. Franklin, T.W. Tombles, A.M. Cassell, H.J Dai,.** 1999, Science, Vol. 283, p. 512.

60. **Hata, K., D.N. Futaba, K.Mizuno, T.Namai, M. Yumura, S. Ijima.** 2004, Science, Vol. 306, p. 1362.

61. **Takagi, D., Y. Homma, H. Hibino, S. Suzuki, Y. Kobeyashi.** 2006, Nano. Lett., Vol. 6, p. 2642.

62. **Zhou, W., Z. Han, J. Wang, Y. Zhang, Z. Jin, X. Sun, C. Yan, Y. Li,.** 2006, Nano. Lett., Vol. 6, p. 2987.

63. **Takagi, D., H. Hibino, S. Suzuki, Y. Kobayashi, Y, Homma.** 2007, Nano. Lett., Vol. 7, p. 2272.

64. **Javey, A., H.J. Dai.** 2005, J. Am. Chem. Soc., Vol. 127, p. 11942.

65. **Peierls, R.** 1935, Annales de l'institut Henri Poincare, Vol. 5, p. 177.

66. **Novoselov, K. S. et al.** 2004, Science, Vol. 306, p. 666.

67. **Wallace, P. R.** 1947, Phys. Rev., Vol. 71, p. 622.

68. **J. R. Williams, L. DiCarlo, C. M. Marcus.** 2007, Science, Vol. 317, p. 638.

69. **D. A. Abanin, L. S. Levitov.** 2007, Science, Vol. 317, p. 641.

70. **Tombros, N., Jozsa, C., Popinciuc, M., Jonkman, H. T. & van Wees, B. J.** 2007, Nature, Vol. 448, p. 571.

71. **Lee, C., Wei, X., Kysar, J. W. & Hone, J.** 2008, Science, Vol. 321, p. 385.

72. **Al-Jishi, R. & Dresselhaus, G.** 1982, Phys. Rev. B, Vol. 26, p. 4514.

73. **Garcia-Sanchez, D., A. M. van der Zande, A. San Paulo, B. Lassagne, P. L. McEuen, and A. Bachtold.** 2008, Nano Lett., Vol. 8, p. 1399.

74. **Roukes, Ekinc K. L.i and M. L.** Rev. Sci. Instrum. : s.n., 2005, Vol. 76, p. 061101.

75. **Craighead, H. G.** 2000, Science, Vol. 290, p. 1532.

76. **Roukes, M. L.** 2001, Phys. World, Vol. 14, p. 25.

77. **Nguyen, C. T.-C.** s.l. : 1486, 1999. IEEE TRANSACTIONS ON MICROWAVE THEORY AND TECHNIQUES. Vol. 47.

78. **LaHaye, M. D., Buu, O., Camarota, B. and Schwab, K. C.** 2004, Science, Vol. 304, p. 74.

79. **Caves, C. M., K. S. Thorne, R. W. P. Drever, V. D. Sandberg, and M. Zimmermann.** 1983, Rev. Mod. Phys., Vol. 52, p. 341.

80. **Magazine, Science.** [Online] 2010. http://sciencecareers.sciencemag.org/career_magazine/previous_issues/articles/2010_12_17/caredit.a1000120.

81. **O'Connell, A. D., M. Hofheinz, M. Ansmann, Radoslaw C. Bialczak, M. Lenander, Erik Lucero, M. Neeley, D. Sank, H. Wang, M. Weides, J. Wenner, John M. Martinis and A. N. Cleland.** 2010, Nature, Vol. 464, p. 697.

82. **Teufel, J. D., T. Donner, D. Li, J.W. Harlow, M. S. Allman, K. Cicak, A. J. Sirois, J. D.Whittaker, K.W. Lehnert, and R.W. Simmonds.** 2011, Nature, Vol. 475, p. 359.

83. **Kis, A., A. Zettl.** 2008, Philos. Trans. A Math. Phys. Eng. Sci., Vol. 366, p. 1611.

84. **Gouttenoire, V., T. Barois, S. Perisanu, J.L. Leclercq, S.T. Purcell, P. Vincent and A. Ayari.** 2010, Small, Vol. 6, p. 1060.

85. **Sazonova, V., Y. Yaish, H. Üstünel, D. Roundy, T. A. Arias and P.l L. McEuen.** 2004, Nature, Vol. 431, p. 284.

86. **Huttel, A. K., G. A. Steele, B. Witkamp, M. Poot, L. P. Kouwenhoven, and H. S. J. van der Zant,.** 2009, Nano Lett., Vol. 9, p. 2547.

87. **Peng, H. B., C.W. Chang, S. Aloni, T. D. Yuzvinsky, and A. Zettl.** 2006, Phys. Rev. Lett., Vol. 97, p. 087203.

88. **Chaste, J., M. Sledzinska, M. Zdrojek, J. Moser, and A. Bachtold.** 2011, Appl. Phys. Lett., Vol. 99, p. 213502.

89. **Laird, E. A., F. Pei, W. Tang, G. A. Steele, and L. P. Kouwenhoven.** 2012, Nano Lett., Vol. 12, p. 193.

90. **Lassagne, B., Y. Tarakanov, J. Kinaret, D. Garcia-Sanchez, and A. Bachtold,.** 2009, Science, Vol. 325, p. 1107.

91. **Steele, G. A., A. K. Huttel, B. Witkamp, M. Poot, H. B. Meerwaldt, L. P. Kouwenhoven, and H. S. J. van der Zant.** 2009, Science, Vol. 325, p. 1103.

92. **Eichler, A., J. Moser, J. Chaste, M. Zdrojek, I. Wilson-Rae, and A. Bachtold.** 2011, Nat. Nanotechnol., Vol. 6, p. 339.

93. **Yang, Y. T., C. Callegari, X. L. Feng, K. L. Ekinci, and M. L. Roukes.** 2006, Nano Lett., Vol. 6, p. 583.

94. **Lassagne, B., D. Garcia-Sanchez, A. Aguasca, and A. Bachtold.** 2008, Nano Lett., Vol. 8, p. 3735.

95. **Chiu, H.-Y., P. Hung, H. W. Ch. Postma, and M. Bockrath.** 2008, Nano Lett., Vol. 8, p. 4342.

96. **Jensen, K., K. Kim, and A. Zettl.** 2008, Nat. Nanotechnol., Vol. 3, p. 533.

97. **Wang, Z., J. Wei, P. Morse, J. G. Dash, O. E. Vilches, and D. H. Cobden.** 2010, Science, Vol. 327, p. 552.

98. **J. Chaste, A. Eichler, J.Moser, G. Ceballos, R. Rurali and A. Bachtold.** Nature Nanotechnol. [Online] 2012. http://www.nature.com/nnano/journal/vaop/ncurrent/full/nnano.2012.42.html.

99. **Li, Ch., and T.-W.Chou.** 2004, Appl. Phys. Lett., Vol. 84, p. 121.

100. **Yoon, J., C. Q. Ru, and A. Mioduchowski,.** 2002, Phys. Rev. B, Vol. 66, p. 233402.

101. **W. Wu, M. Palaniapan and W.-K. Wong,.** 2008, Electr. Lett., Vol. 44.

102. **J. S. Bunch, A. M. van der Zande, S. S. Verbridge, I. W. Frank, D. M. Tanenbaum, J. M. Parpia, H. G. Craighead and P.l L. McEuen.** 2007, Science, Vol. 315, p. 490.

103. **C. Chen, S. Rosenblatt, K. I. Bolotin, W. Kalb, P. Kim, I. Kymissis, H. L. Stormer, T. F. Heinz, and J. Hone.** 2009, Nature Nanotechnol., Vol. 4, p. 861.

104. **R. A. Barton, B. Ilic, A. M. van der Zande, W. S. Whitney, P. L. McEuen, J. M. Parpia and H. G. Craighead.** 2011, Nano. Lett., Vol. 11, p. 1232.

105. **A. M. van der Zande, R. A. Barton, J. S. Alden, C. S. Ruiz-Vargas,W. S. Whitney, P. H. Q. Pham, J. Park, J. M. Parpia, H. G. Craighead and P. L. McEuen.** 2010, Nano Lett., Vol. 10, p. 4869.

106. [Online] https://www.jyu.fi/fysiikka/en/research/material/nanophys/moltech/research.

107. **Deshpande, V. V., H.-Y. Chiu, H. W. Ch. Postma, C. Mikó, L. Forró, and M. Bockrath.** 2003, Nano Lett., Vol. 6, p. 1092.

108. **A. M. Fennimore, T. D. Yuzvinsky, Wei-Qiang Han, M. S. Fuhrer, J. Cumings, A. Zettl.** 2003, Nature, Vol. 424, p. 408.

109. **B. Bourlon, D.C. Glattli, C. Miko, L. Forro, A. Bachtold.** 2004, Nano Lett., Vol. 4, p. 709.

110. **B. C. Regan, S. Aloni, R. O. Ritchie, U. Dahmen and A. Zettl.** 2004, Nature, Vol. 428, p. 924.

111. **Svensson, K., H. Olin, E. Olsson.** 2000, Phys. Rev. Lett., Vol. 93, p. 145901.

112. **Golberg D., Costa P.M.F.J., Mitome M., Mueller Ch., Hampel S., Leonhardt A., Bando Y.** 2007, Adv. Mater., Vol. 19, p. 1937.

113. **Löffler, M., U. Weissker, T. Mühl, T. Gemming, J. Eckert, B. Büchner.** 2011, Adv. Mat., Vol. 23, p. 541.

114. **Barreiro, A., R. Rurali, E. R. Hernández, J. Moser, T. Pichler, L. Forró and A. Bachtold.** 2008, Science, Vol. 320, p. 775.

115. **Drexler, K. E.** *Nanosystems: Molecular Machinery, Manufacturing and Computation.* New York : Wiley, 1992. p. 297.

116. **Rugar, H. J. Mamin and D.** 2001, Appl. Phys. Lett., Vol. 79, p. 3358.

117. **J. D. Teufel, T. Donner, M. A. Castellanos-Beltran, J. W. Harlow, and K. W. Lehnert.** 2009, Nat. Nanotechnol., Vol. 4, p. 820.

118. **T. Rocheleau, T. Ndukum, C. Macklin, J. B. Hertzberg, A. A. Clerk, and K. C. Schwab.** 2009, Nature, Vol. 463, p. 72.

119. **X. M. H. Huang, C. A. Zorman, M. Mehregany, and M. L. Roukes.** 2003, Nature, Vol. 421, p. 496.

120. **13. N. Liu, F. Giesen, M. Belov, J. Losby, J. Moroz, A. E. Fraser, G. McKinnon, T. J. Clement, V. Sauer, W. K. Hiebert, and M. R. Freeman.** 2008, Nat. Nanotechnol., Vol. 3, p. 715.

121. **Wu, C. C., and Z. Zhong.** 2011, Nano Lett., Vol. 11, p. 1448.

122. **Eichler, A., J. Chaste, J. Moser, and A. Bachtold.** 2011, Nano Lett., Vol. 11, p. 2699.

123. **Sapmaz, S., P. Jarillo-Herrero, Y. M. Blanter, C. Dekker, and H. S. J. van der Zant,.** 2006, Phys. Rev. Lett., Vol. 96, p. 026801.

124. **MacNair, J. F. C. Nix and D.** 1940, Phys. Rev., Vol. 60, p. 597.

125. **W. Bao, F. Miao, Z. Chen, H. Zhang, W. Jang, C. Dames, and C. N. Lau.** 2009, Nat. Nanotechnol., Vol. 4, p. 562.

126. **V. Singh, S. Sengupta, H. S. Solanki, R. Dhall, A. Allain, S. Dhara, P.Pant, and M. Deshmukh.** 2010, Nanotechnology, Vol. 21, p. 165204.

127. **Y. K. Kwon, S. Berber, and D. Tomanek,.** 2004, Phys. Rev. Lett., Vol. 92, p. 015901.

128. **Ballantine, D. S. and al, et.** *Acoustic Wave Sensors.* San Diego, CA : Academic Press, 1997.

129. **Lu, C.** *Application of Piezoelectric Quartz Crystal Microbalance.* London : Elsevier, 1984.

130. **Thompson, M. and Stone, D. C.** *Surface-Launched Acoustic WaVeSensors: Chemical Sensing and Thin Film Characterization.* New York : John Wiley and Sons, 1997.

131. **Ekinci, K. L. and Yang, Y. T. and Roukes, M. L.** 2004, J. Appl. Phys, Vol. 95, p. 2682.

132. **Cleland, A. N. and Roukes, M. L. J.** 2002, J. Appl. Phys., Vol. 92, p. 2758.

133. **Yang Y.T., Callegari C., Feng X.L. and Roukes M.L.** 2011, Nano. Lett., Vol. 11, p. 1753.

134. **Blencowe, M.** 2004, Phys. Rep., Vol. 395, p. 159.

135. **Knobel, R. G. and Cleland, A. N.** 2003, Nature, Vol. 424, p. 291.

136. **Poncharal, P., Wang, Z. L., Ugarte, D. and de Heer, W. A.** 2004, Science, Vol. 304, p. 74.

137. **Babic, B., Furer, J., Sahoo, S., Farhangfar, S. & Schonenberger, C.** 2003, Nano Lett., Vol. 3, p. 1577.

138. **Meyer, J. C., Paillet, M. and Roth, S.** 2005, Science, Vol. 309, p. 1539.

139. **Jensen, K., C¸ . Girit, Mickelson, W. and Zettl, A.** 2006, Phys. Rev. Lett., Vol. 96, p. 215503.

140. **Purcell, S. T., Vincent, P., Journet, C. and Binh, V. T.** 2002, Phys. Rev. Lett., Vol. 89, p. 276103.

141. **P. G. Collins, M. S. Arnold and Ph. Avouris.** 2001, Science, Vol. 292, p. 706.

142. **M. Bockrath, D. H. Cobden, P. L. McEuen, N. G. C, A. Zettl, A. Thess and R. E. Smalley.** 1997, Science, Vol. 275, p. 1922.

143. **S. J. Tans, M. H. Devoret, H. Dai, A. Thess, R. E. Smalley, L.J. Geerligs and C. Dekker.** 1997, Nature, Vol. 386, p. 474.

144. **Mailly, F., et al.** 2001, Sens. Act., Vol. 94, p. 32.

145. **Dai, C.L. A.** 2007, Sens. Act. B, Vol. 122, p. 375.

146. **D. Briand, S. Heimgartner, M.-A. Gretillat, B. van der Schoot and N. F. de Rooij J.** 2002, J. Micromech. Microeng., Vol. 12, p. 971.

147. **Puigcorbe, J., D. Vogel, B. Michel, A. Vila, I. Gracia, C. Cane and J. R. Morante.** 2003, J. Micromech. Microeng., Vol. 13, p. 548.

148. **Chen, L. and Mehregany, M.** Atlanta, GA : s.n., 2007. Proceedings of the 6th IEEE Sensors Conference. p. 620.

149. **Mailly, F., et al.** 2001, Sens. Actuat. A, Vol. 94, p. 32.

150. **Aslam, M. and Gregory, C. and Hatfield, J.V.** 2004, Sens. Actuat. B, Vol. 103, p. 153.

151. **Mo, Y.W., et al.** 2001, Sens. Act. B, Vol. 79, p. 175.

152. **Tao, C., Yin, C. and He, M. and Tu, S.** Sanya, China : s.n., 2008. Proceedings of the 3rd IEEE International Conference on Nano/Micro Engineered and Molecular Systems. p. 284.

153. **Furjes, P., et al.** 2002, Sens. Act. A, Vol. 99, p. 98.

154. **Creemer, J.F., et al.** 2008, Sens. Act. A, Vol. 148, p. 416.

155. **Esch, H., G. Huyberechts, R. Mertens, G. Maes, J. Manca, W. De Ceuninck and L. De Schepperm.** 2000, Sens. and Act. B, Vol. 65, p. 190.

156. **Briand, H D., S. Heimgartner, M.-A. Gretillat, B. van der Schoot, N. F. de Rooij.** 2002, J. Micromech. Microeng., Vol. 12, p. 971.

157. **Graf, M., D. Barrettino, K.U. Kirstein and A. Hierlemann.** 2008, Sens. and Act. A, Vol. 142, p. 284.

158. **Courbat, J. and D. Briand, N.F. de Rooij.** 2008, Sens. Act. A, Vol. 142, p. 285.

159. **D. Teyssieux, D. Briand, J. Charnay, N.F. de Rooij and B. Cretin.** 2008, J. Micromech. Microeng., Vol. 18, p. 065005.

160. **Cozzani, E., et al.** Atlanta, GA, USA : s.n., 2007. Proceeding of the 6th IEEE Sensors Conference. p. 181.

161. [Online] http://news.thomasnet.com/fullstory/MEMS-Micro-Hot-Plates-suit-chemical-sensor-applications-818227 .

162. **Mo, Y., Y. Okawa, M. Tajima, T. Nakai, N. Yoshiike and K.i Natukawa.** 2001, Sens. and. Act. B, Vol. 79, p. 175.

163. **Briand, D. and F. Beaudoin, J. Courbat, N.F. de Rooij, R. Desplats and P. Perdu.** 2005, Microelectronics Reliability, Vol. 45, p. 1786.

164. **Charnay, J. and N.F. de Rooij, B. Cretin.** 2008, J. Micromech. Microeng., Vol. 18, p. 065005.

165. **P. DENG, Y-K. LEE and P. CHENG.** Characterization of An Integrated Self-sensing Submicron Bubble Actuator . [Online] http://www.icee-con.org/papers/2004/69.pdf).

166. **al., K. Sato et.** 1988, Sens. Act. A, Vol. 64, p. 87.

167. **Hull, R.** *Properties of Crystalline Silicon .* London : INSPEC, 1999.

168. **Cleland, A. N.** *Foundations of Nanomechanics.* s.l. : Springer, 2003.

169. [Online] http://www.virginiasemi.com/pdf/siliconetchingandcleaning.pdf.

170. **C.-J. Lu, W. H. Steinecker, W.-Ch. Tian, M. C. Oborny, J. M. Nichols, M. Agah, J. A. Potkay, H. K. L. Chan, J. Driscoll, R. D. Sacks, K.l D. Wise, S. W. Pang and E. T. Zellers.** 2005, Lab Chip, Vol. 5, p. 1123.

171. **W.-C. Tian, S. W. Pang.** 2002, J. Vac. Sci. Technol. B, Vol. 20.

172. **W.-C. Tian, S. W. Pang.** 2003, J. Vac. Sci. Technol. B, Vol. 21.

173. [Online] http://cleanroom.byu.edu/ResistivityCal.phtml.

174. **(F. Mailly, A. Giani, R. Bonnot, P. Temple-Boyer, F. Pascal-Delannoy, A. Foucaran and A. Boyer.** 2001, Sens. Act. A, Vol. 92, p. 32.

175. **Junmo Kang, Hyeongkeun Kim, Keun Soo Kim, Seoung-Ki Lee, S. Bae, J.-H. Ahn, Y.-J. Kim, J.-B. Choi and . Hee Hong.** 2011, Nano Lett., Vol. 11, p. 5154.

176. **Pop, E., Mann, D. and Goodson, K.and Dai, H.** 2007, J. Appl. Phys., Vol. 101, p. 093710.

177. **Shi, L., et al.** 2009, J. Appl. Phys., Vol. 105, p. 104306.

178. **Pop, E., et al.** 2005, Phys. Rev. Lett., Vol. 95, p. 155505.

179. **Rotkin, S. V., Perebeinos, V. and Petrov, A. G. and Avouris, P.** 2009, Nano Lett., Vol. 9, p. 1850.

180. **Bae, M.-H., Ong, Z.-Y., Estrada, D. and Pop, E.** 2010, Nano Lett., Vol. 10, p. 4787.

181. **Grosse, K.L., M.-H. Bae, F. Lian, E. Pop and W. P. King.** 2011, Nature Nanotechnol., Vol. 6, p. 287.

182. **Z. Yao, C. L. Kane, and C. Dekker.** 2000, Phys. Rev. Lett., Vol. 84, p. 2941.

183. **Hummel, R. E.** 1994, Int. Mater. Rev., Vol. 39, p. 97.

184. **H. Park, A. K. L. Lim, J. Park, A. P. Alivisatos and P. L. McEuen.** 1999, Appl. Phys. Lett., Vol. 75, p. 301.

185. **J. Moser, A. Barreiro and A. Bachtold.** 2007, Appl. Phys. Lett., Vol. 91, p. 163513.

186. **A. M. Goossen, V. E. Calado, A. Barreiro, K. Watanabe, T. Taniguchi and L. M. K. Vandersypen,.** 2012, Appl. Phys. Lett., Vol. 100, p. 073110.

187. **Y. Miyamoto, A. Rubio, S.G. Louie, M. L. Cohen.** 1996, Phys. Rev. Lett., Vol. 76, p. 2121.

188. **C. J. Lambert, S. W. D. Bailey and J. Cserti.** 2008, Phys. Rev. B, Vol. 78, p. 233405.

189. **V. Krstic, G.Wagniere, G. L. J. A. Rikken.** 2004, Chem. Phys. Lett., Vol. 390, p. 25.

190. **Y. Miyamoto, A. Rubio, S.G. Louie, M. L. Cohen.** 1999, Phys. Rev. B, Vol. 60, p. 13885.

191. **P. Kral, E. J. Mele, D. Tomanek.** 2000, Phys. Rev. Lett., Vol. 85, p. 1512.

192. **R. T. Senger, S. Dag, S. Ciraci.** 2004, Phys. Rev. Lett., Vol. 93, p. 196807.

193. **Hsu, P. C. Watts and W. K.** 2004, Appl. Phys. A: Mater. Sci. Process., Vol. 78, p. 79.

194. **S.W.D. Bailey, I. Amanatidis and C.J Lambert,.** 2008, Phys. Rev. Lett., Vol. 100, p. 256802.

195. **A.N. Kolmogorov, V.H Crespi.** 2000, Phys. Rev. Lett., Vol. 85, p. 4727.

196. **Veeco.** *Veeco Dimension 3100 User's manual.*

197. **Nezbeda, D. E. Soule and C. W.** 1968, J. Appl. Phys., Vol. 39, p. 5122.

198. **Wang, S.** 2010, EPL, Vol. 89, p. 17005.

199. *IEEE TRANSACTIONS ON ELECTRONICS PACKAGING MANUFACTURING.* 2003, Vol. 26.

200. **Muray, I. Brodie and J. J.** *The Physics of Micro/Nano-Fabrication.* New York : Plenum, 1992.

201. **Timp, G.** *Nanotechnology.* New York : Springer-Verlag, 1999.

202. **Ferry, M. Khoury and D. K.** 1996, J. Vac. Sci. Technol. B, Vol. 14, p. 75.

203. **G. H. Bernstein, D. A. Hill, and W. Liu.** 1992, J. Appl. Phys., Vol. 71, p. 4066.

204. **E. D. Minot, Y. Yaish, V. Sazonova and P. L. McEuen.** 2004, Nature, Vol. 428, p. 536.

205. **Solomon, P. M.** *Future Trends in Micreoelectronics: Up the Nano Creek.* New York : Wiley, 2007.

206.

207. **E. V. Castro, K. S. Novoselov, S. V. Morozov, N. M. R. Peres, J. M. B. Lopes dos Santos, Johan Nilsson, F. Guinea, A. K. Geim, and A. H. Castro Neto.** 2007, Phys. Rev. Lett, Vol. 99, p. 216802.

208. **T. Ohta, Aaron Bostwick, Thomas Seyller, Karsten Horn and Eli Rotenberg.** 2006, Science, Vol. 313, p. 951.

209. **Thess, A., R. Lee, P. Nikolaev, H. Dai, P. Petit, J. Robert, C. Xu, Y.H. Lee, S.G. Kim, A. G. Rinzler, D. T. Colbert, G.E. Scuseria, D. Tomanek, J. E. Fischer, R. E. Smalley.** 1996, Science, Vol. 273, p. 483.

210. **K.L. Ekinci, M.L.Roukes.** 2005, Rev. Sci. Instr., Vol. 76, p. 061101.